DEVELOPMENT OF REDUCED ORDER MODEL FOR DYNAMIC ANALYSIS OF AIRCRAFT VIA GLOBAL OPTIMIZATION

A THESIS SUBMITTED TO
THE GRADUATE SCHOOL OF NATURAL AND APPLIED SCIENCES
OF
MIDDLE EAST TECHNICAL UNIVERSITY

BY

OĞUZHAN KÖSE

IN PARTIAL FULFILLMENT OF THE REQUIREMENTS
FOR
THE DEGREE OF MASTER OF SCIENCE
IN
AEROSPACE ENGINEERING

AUGUST 2023

Approval of the thesis:

DEVELOPMENT OF REDUCED ORDER MODEL FOR DYNAMIC ANALYSIS OF AIRCRAFT VIA GLOBAL OPTIMIZATION

submitted by **OĞUZHAN KÖSE** in partial fulfillment of the requirements for the degree of **Master of Science** in **Aerospace Engineering, Middle East Technical University** by,

Prof. Dr. Halil Kalıpçılar
Dean, Graduate School of **Natural and Applied Sciences** _____

Prof. Dr. Serkan Özgen
Head of the Department, **Aerospace Engineering** _____

Prof. Dr. Altan Kayran
Supervisor, **Aerospace Engineering, METU** _____

Examining Committee Members:

Prof. Dr. Demirkan Çöker
Aerospace Engineering Dept., METU _____

Prof. Dr. Altan Kayran
Aerospace Engineering Dept., METU _____

Assoc. Prof. Dr. Ercan Gürses
Aerospace Engineering Dept., METU _____

Asst. Prof. Dr. Görkem Eğemen Güloğlu
Aerospace Engineering Dept., METU _____

Assoc. Prof. Dr. Turaç Farsadi
Mechanical Engineering Dept., ATÜ _____

Date: 21.08.2023

I hereby declare that all information in this document has been obtained and presented in accordance with academic rules and ethical conduct. I also declare that, as required by these rules and conduct, I have fully cited and referenced all material and results that are not original to this work.

Name Last name : Oğuzhan Köse

Signature :

ABSTRACT

DEVELOPMENT OF REDUCED ORDER MODEL FOR DYNAMIC ANALYSIS OF AIRCRAFT VIA GLOBAL OPTIMIZATION

Köse, Oğuzhan
Master of Science, Aerospace Engineering
Supervisor : Prof. Dr. Altan Kayran

August 2023, 148 pages

Reduced models are often used in the early phases of aircraft design to shorten analysis times and contribute to the optimization process. In the final stages of aircraft design, reduced models are used to create the mathematical model of the aircraft after ground vibration tests. This thesis study explains the creation process of a reduced model, the beam stick model (BSM). The BSM reduces the 3-dimensional finite element model to 1-dimensional. BSMs can be used to estimate the loads on the aircraft or to reflect the dynamic characteristics of the aircraft. This study uses the global optimization method to create BSM of the METU Very Light Aircraft (VLA). The Crow Search Algorithm (CSA) is used as a global optimization method with specific updates. In addition, a new methodology has been developed when connecting control surfaces to lifting surfaces in the reduced order BSM. In the thesis, the detailed structural finite element model and the BSM's natural frequencies and mode shapes are compared. The modal analysis solver of the MSC NASTRAN finite element program is used to make this comparison. Then, flutter and gust response analysis are performed using the BSM, and the results are compared with the analysis results obtained with the detailed finite element model.

It is seen that the results of the detailed finite element model and the BSM match very well. Dynamic aeroelasticity analyses should be repeated with many mass combinations due to the certification criteria of aircraft. For this reason, the response of the aircraft structure and the BSM to mass changes is expected to be the same. The modal analysis results of the mass change of the BSM and the detailed finite element model are also examined. It is observed that both models give similar responses. The analyses show that the proposed methodology to generate BSM can be used effectively and reliably in dynamic aeroelasticity studies.

Keywords: Reduced order models; Beam stick model; Global optimization; Aeroelasticity; Dynamic response

ÖZ

GENEL ENİYİLEME YOLUYLA UÇAKLARIN DİNAMİK ANALİZİ İÇİN İNDİRGENMİŞ MODELLERİN GELİŞTİRİLMESİ

Köse, Oğuzhan
Yüksek Lisans, Havacılık ve Uzay Mühendisliği
Tez Yöneticisi: Prof. Dr. Altan Kayran

Ağustos 2023, 148 sayfa

Uçak tasarımının ilk fazlarında analiz sürelerini kısaltmak, optimizasyon sürecine katkıda bulunmak indirgenmiş modeller sıklıkla kullanılır. Uçak tasarımının son safhalarında ise yer titreşim testlerinden sonra uçağın matematiksel modelini oluşturmak için indirgenmiş modellerden yararlanılmaktadır. Bu tezde, bir indirgenmiş model olan kiriş-çubuk modelinin oluşturulma süreci anlatılacaktır. Kiriş-çubuk modeli 3 boyutlu sonlu elemanlar modelinin 1 boyuta indirgenmesi amacıyla kullanılır. Kiriş-çubuk modeller uçak üzerindeki yükleri tahmin etmede ya da uçağın dinamik karakteristiğini yansıtmada kullanılabilir. Bu çalışmada, genel eniyileme yöntemi kullanılarak ODTÜ Çok Hafif Uçağının (VLA) kiriş-çubuk modeli oluşturulmuştur. Genel eniyileme yöntemi olarak karga arama algoritması bazı güncellemeler yapılarak kullanılmıştır. Ayrıca, kontrol yüzeylerini, kaldırma yüzeylerine bağlanırken yeni metodoloji geliştirilmiştir. Önerilen yöntemle oluşturulan kiriş-çubuk modeli ile uçak yapısının dinamik karakteristiklerinin örtüşmesi amaçlanmaktadır. Kiriş-çubuk model ile detaylı sonlu elemanlar modelinin doğal frekans ve titreşim şekilleri karşılaştırılmıştır. Bu karşılaştırmayı yapmak için MSC NASTRAN sonlu elemanlar programının modal analiz çözücüsü kullanılmıştır. Daha sonra, kiriş-çubuk model kullanılarak çırpınma ve rüzgar tepkisi

analizleri yapılmıştır ve sonuçlar detaylı sonlu elemanlar modeli ile yapılan analizlerle karşılaştırılmıştır. Detaylı sonlu elemanlar modeli ile kiriş-çubuk modelin sonuçlarının birbirleri ile uyuştuğu gözlemlenmiştir. Dinamik aeroelastisite analizleri sertifikasyon kriterleri gereği birçok farklı kütle kombinasyonları ile tekrarlanması gerekmektedir. Bu sebeple, uçak yapısı ile kiriş-çubuk modelin kütle değişimlerine tepkisinin aynı olması beklenir. Kiriş-çubuk model ile detaylı sonlu elemanlar modelinin kütle değişimi sonucu modal analiz sonuçları incelenmiştir. Her iki yapının da benzer tepkiler verdiği gözlemlenmiştir. Yapılan analizler önerilen kiriş-çubuk model oluşturma yönteminin dinamik aeroelastisite problemlerinde kullanılabileceğini göstermiştir.

Anahtar Kelimeler: İndirgenmiş modeller; Kiriş-çubuk model; Genel eniyileme; Aeroelastisite, Dinamik cevap

To my family, who always do their best for me…

ACKNOWLEDGMENTS

First of all, I would like to express my gratitude to my advisor, Prof. Dr. Altan Kayran, for guidance and invaluable support. Working with him has been a great experience. His valuable insights have helped me enhance the quality of my work, and I have learned a lot from him throughout this journey.

The METU-VLA aircraft's finite element model is used in this thesis. I want to express my gratitude to Turkish Aerospace Industries, Inc. for supporting the METU-VLA project. I also want to thank the students who contributed their efforts to this project.

I extend my heartfelt gratitude to my parents, Funda Köse and Hamza Köse, for their unwavering love, support, and guidance throughout my life.

I would also like to thank my uncle, Mazhar Tuğlu, sincerely. His outlook on life and bravery will serve as a constant example for me.

Lastly, I would like to thank my friend, Murat Aydın. His dedicated efforts and contributions to my work have been invaluable. His willingness to support me throughout this journey has made a significant difference, and I am genuinely thankful for his friendship and assistance.

TABLE OF CONTENTS

LIST OF TABLES

TABLES

LIST OF FIGURES

FIGURES

LIST OF ABBREVIATIONS

ABBREVIATIONS	
A	Antisymmetric
AIC	Aerodynamic Influence Coefficient Matrix
AP	Awareness Probability
BSM	Beam Stick Model
CG	Center of Gravity
CSA	Crow Search Algorithm
DLM	Doublet-lattice Method
DOF	Degrees of Freedom
FEM	Finite Element Model
GFEM	Global Finite Element Model
IPS	Infinite Plate Spline
IRS	Improved Reduced System
MAC	Modal Assurance Criteria
MDOF	Multi-Degrees of Freedom
ROM	Reduced order model
S	Symmetric
SEREP	System Equivalent Reduction Expansion Process
VAM	Variational Asymptotic Method
VLA	Very Light Aircraft

LIST OF SYMBOLS

SYMBOLS	
$Area$	Cross-sectional area of the beam element
AP	Awareness probability
B_{hh}	Generalized viscous damping matrix
C	Damping matrix
$\bar{c}$	Reference chord
F_a	Aerodynamic forces on the structural elements
F_e	External forces
F_h	Aerodynamic forces on the aerodynamic boxes
F_r	Frequency ratio
fl	Flight length
G	Spline matrix
g	Non-dimensional damping
h	Interpolated displacement vector for aerodynamic boxes
H_{hh}	Generalized structural damping matrix
Hz	Hertz
i	Complex number
I	Identity matrix
I_{yy}	Area moment of inertia about the y-axis
I_{zz}	Area moment of inertia about the z-axis
J	Polar moment of inertia
K	Stiffness matrix
k	Reduced frequency
K_{hh}	Generalized stiffness matrix
$\bar{K}_{global}$	Stiffness matrix written according to the global coordinate system for a beam element

$\bar{K}_{local}$	Stiffness matrix written according to the local coordinate system for a beam element
M	Mass matrix
m	Memory matrix
M_{hh}	Generalized mass matrix
N_z	The normal component for vertical gusts
Q	Force vector
Q_{hh}	Generalized aerodynamic force matrix
q	Displacement vector
q_∞	Dynamic pressure
r	Random number with a uniform distribution between 0 and 1
S	The position of the aircraft relative to the gust
S_{kj}	Transformation matrix (from pressure coefficient to force and moments)
T	Transformation matrix (from local coordinate system to global coordinate system)
u	Mode shape vector
U_{de}	Gust velocity
V	Free-stream velocity
Vf	Velocity versus frequency
Vg	Velocity versus damping
w_g	Discrete gust profile
x	Position matrix
γ	Decay parameter
η	Generalized displacement
ρ	Air density
ϕ	Modal matrix
ω	Natural frequency
$\bar{\omega}$	Angular frequency

CHAPTER 1

INTRODUCTION

1.1 Background to the Study

The field of aeroelasticity deals with analyzing how the structural response of an aircraft is influenced by the aerodynamic forces it experiences. These interactions can lead to complex and sometimes unpredictable behavior. Therefore, aeroelasticity is critical in ensuring an aircraft's structural integrity, stability, and performance. Aeroelastic analyses can be broadly classified into static aeroelasticity and dynamic aeroelasticity.

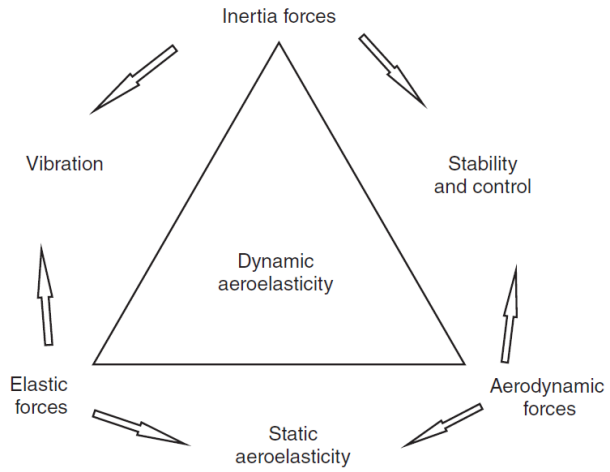

Figure 1.1 Collar's aeroelastic triangle [1]

Static aeroelastic analysis studies the flexibility of the structure under aerodynamic loads. These analyses examine the load distribution changing with the effects of flexibility, the effectiveness of the control surfaces, and the divergence instability.

These time-independent analyses are essential to understanding the aircraft's structural response to static loads.

The field of dynamic aeroelasticity examines how an aircraft's structure responds to aerodynamic forces under dynamic conditions. Dynamic aeroelastic analyses are essential for aircraft certification. Many dynamic analyses, such as flutter, gust, and nonlinear flutter, must be performed during the aircraft design process. When an aircraft experiences self-induced and unstable oscillations due to the aerodynamic forces acting upon it, this phenomenon is known as flutter. Flutter can result in large deformations and can ultimately lead to structural failure. Gust analysis examines the dynamic response of the aircraft, taking into account the aircraft's flexibility due to changes in the lift distribution caused by a gust.

The solutions to such dynamic aeroelasticity problems include adding mass balance, increasing the control loop stiffness, or increasing the stiffness in certain aircraft regions. However, most of these solutions increase the mass of the aircraft. For weight-saving purposes and increasing the efficiency of the aircraft, dynamic aeroelasticity analysis should be included in the optimization process at the beginning of the aircraft design process. The dynamic characteristics of airplanes are usually estimated with finite element models (FEM). These models often contain many elements. Complex FEM dramatically increases the computational time in dynamic analysis. Times are manageable for a single analysis. However, in a dynamic analysis framework, the total analysis time increases considerably for different mass/CG configurations of the aircraft, store configurations, iterative solutions in nonlinear flutter analysis, and multidisciplinary optimization problems. Moreover, creating a detailed FEM for each configuration is very costly.

This makes using a reduced-order model (ROM) in such analysis necessary. ROMs are also used in the final stages of aircraft design projects to create a mathematical model suitable for evaluating the results of ground vibration tests (GVT). In this thesis, the beam stick model (BSM), one of the ROM types, is the focus of the study. In creating the BSM, the global optimization method is used, and the BSM is then

used in flutter and gust analyses. Comparisons are made with high-fidelity analyses to evaluate the accuracy and efficiency of the BSM.

1.1.1 Beam Stick Model

The use of BSMs in dynamic aeroelasticity analysis has become increasingly common due to their efficiency and accuracy. BSMs can accurately predict the dynamic behavior of the aircraft and are often used in multidisciplinary optimization studies, where a quick evaluation of the aircraft's dynamic response is required. The optimization process involves modifying the aircraft's design parameters to achieve performance goals while ensuring that the aircraft's dynamic response remains within acceptable limits.

The BSM is created by dividing the aircraft structure into several beam finite elements and connecting them on the elastic axis of the aircraft. The elastic axis is a theoretical line along which the structure would bend if it were only under bending loads [2]. By determining the appropriate cross-sectional properties of the beam elements, the dynamic characteristics of the aircraft can be represented. BSMs are created utilizing data obtained from the "Global Finite Element Model" (GFEM) or the data obtained in GVTs.

Using BSMs has several advantages over using GFEM models:

- The number of elements is much lower, significantly reducing the computational time required for dynamic analyses.
- BSMs can be easily modified and updated, allowing for quicker design iterations.
- BSMs are more suitable for sensitivity analysis and optimization, as they require fewer design variables than the GFEM.

The accuracy of stick models is vital to aircraft design, as these models are often included in the optimization process. The accuracy of BSMs depends on the number of beam elements, the accuracy of the cross-sectional properties, and the boundary

conditions. Therefore, the validation of the BSMs using high-fidelity models is critical to ensure their accuracy and reliability.

Figure 1.2 shows a typical stick model of a half aircraft. The black elements in Figure 1.2 represent the beams. Orange triangular elements represent lumped masses. The purple elements extending from the beams to the leading and trailing edges are the RBE2 elements. RBE2 elements are rigid and have been added to the model to improve the fluid-solid interaction used in many dynamic analyses.

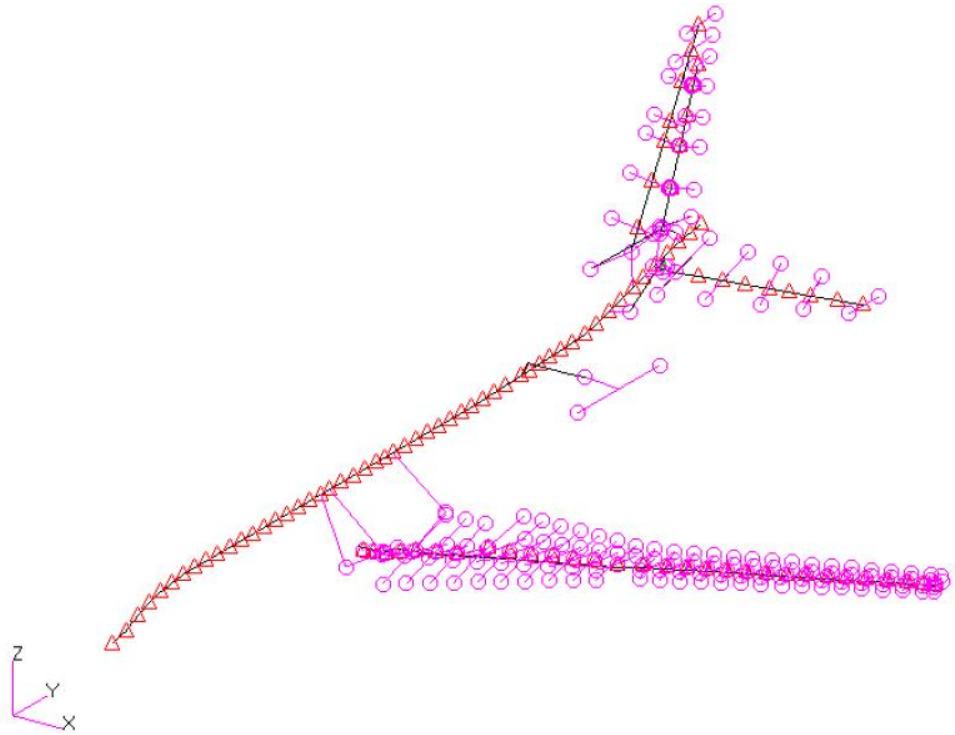

Figure 1.2 Beam Stick Model [3]

1.1.2 Global Optimization

The global optimization method is a proper optimization for complex problems that cannot be differentiated. It is used in almost every field, from engineering design to financing. In global optimization, the probability of getting stuck at local minima or

local maxima is very low compared to other optimization methods. Discrete and integer design variables can be managed more easily. In addition, global optimization methods do not need gradient information in the optimization process. Therefore, the popularity of global optimization increases day by day.

It should be noted that many design variables are needed in generating BSM, and the connections between the design variables can completely change the result. Considering these, using global optimization methods in the stick model creation process seems logical. In this thesis, the Crow Search Algorithm (CSA) [4], one of the swarm intelligence algorithms, is used while creating the BSM. CSA is preferred because of its ability to reach optimum results quickly and being a proven method.

1.2 Motivation of the Thesis

The motivation of this thesis can be listed as follows.

- Most of the studies in the literature focused on developing reduced order models for one component of the aircraft. However, in dynamic analysis, the effect of the components on each other is undeniable. In order to catch the unstable behavior in the aircraft, the whole aircraft must be modeled and in this thesis stick model of the whole aircraft is generated.
- In some of the studies in the literature, reduced order models including control surfaces exist. However, there are scarce resources in the literature that model lifting surfaces together with control surfaces in developing BSMs. Control surfaces can have a significant impact on dynamic analysis and their inclusion in BSMs are very critical in reflecting the true dynamic behavior of the aircraft.
- Most of the research in the literature has focused on four main modes (First bending, first torsion, second bending, and second torsion) in the development process of BSMs. Effects of other modes on dynamic analysis are not included.

1.3 Objective of the Thesis

The main objective of this thesis is to generate a beam stick model for the dynamic analysis of complete aircraft with high fidelity. Aims can be listed as:

- To develop beam stick model of a full aircraft including control surfaces and including all the primary modes of the aircraft.
- To develop a new method for connecting control surfaces to the lifting surface in the stick model of the aircraft.
- To perform comparative studies on the flutter, and gust analysis of the full aircraft with the developed stick model and the detailed FEM of the aircraft.

1.4 Outline of the Thesis

The structure of this thesis is summarized as follows:

In Chapter 2, a literature survey on ROM is presented. However, to cover the scope of this thesis in more detail, a comprehensive literature review on BSM rather than other ROM variants is conducted.

Chapter 3 explains the stages of creating the aeroelastic model of the METU Very Light Aircraft (VLA) aircraft in detail. The aeroelastic model combines three basic models: the structural model, the mass model, and the aerodynamic model. The process of creating these models is presented in detail in this section. In addition, the modal analysis results of GFEM are also presented in this section. Fluid-structure coupling, which provides the interaction between the aerodynamic model and the structural model, is also successfully performed to prepare the model for aeroelastic analysis.

Chapter 4 describes the CSA, a swarm intelligence algorithm used to create the BSM. CSA modifications, objective functions, and design variables are presented in this section.

The steps involved in developing the BSM are described in detail in Chapter 5. It describes the conversion of the wing, fuselage, horizontal, and vertical tail from the GFEM to the BSM. The proposed methods for attaching lifting surfaces to the fuselage and control surfaces to the lifting surfaces are also explained thoroughly.

In Chapter 6, the splines and aerodynamic models developed for the BSM are introduced. Flutter and discrete gust analysis performed with BSM and GFEM are compared. In addition, the responses of BSM to mass changes are investigated. This chapter evaluates how reliable is the BSM developed in predicting the dynamic aeroelastic response of the VLA.

The overall conclusions of the thesis study are provided in Chapter 7.

CHAPTER 2

LITERATURE REVIEW

There are two ways to create a ROM in the aerospace industry. The first way is the BSM, while the second is to create a matrix-based ROM [5].

In the literature, stick models are created utilizing different methods. Singh and Nichols' study is one of the first methods used in the field of reduced order modeling based on BSM [6]. The complex wing FE model is fixed at the root at the beginning of the process. Then, a unit force is given from the free end of the wing. The displacements at specific points are measured under the specified boundary conditions. Beam stiffness properties are determined in accordance with the measured displacements. Afterward, BSM is created on the elastic axis with the stiffness properties determined. At the end of the analysis, a comparison is made between the natural frequencies and mode shapes obtained from the BSM and the FEM generated using shell elements. Corriveau and Dervault [7] also created BSM using a similar method. They studied how the accuracy of the created BSM changes according to the aspect ratio, sweep angle, and wing thickness. They pointed out that as the aspect ratio decreases, the fidelity of the BSM decreases. Jones and Cesnik [8] created a nonlinear stick model using this method. The created stick model is used in dynamic aeroelasticity analysis. Hashemi-Kia and Toosi [9] generated BSM using a different methodology. Instead of calculating beam properties by giving unit force, they determined beam properties by giving unit deflection. Hayirli and Kayran [10] performed dynamic response analyses using this method. Hajela and Chen [11] calculated the moment of inertia, the product of inertia and torsional constants of a wing. An equivalent beam model is created by using these values. The beam stiffness properties are scaled, taking into account the shear lag effects so that the created

BSM is not stiffer than the actual aircraft wing. BSM is used in optimization problems to reduce the weight of the wing. Corn et al. [12] developed a method for creating stick models for hollow-type structures. They have considered the situation of non-overlapping shear and mass centers. Timoshenko beam theory [13] is used in the article. Hence, the BSM that is generated in this study can also represent coupled bending and torsion modes. Piperni et al. [14] modeled the wing torque box with spar, flange, and stringer. In this study, thin-walled sections are transformed into stick models along the elastic axis. The created stick model is used in multidisciplinary optimization for a business jet. Elsayed et al. [15] created a BSM that can be used in static analysis. The wing is divided into many spanwise parts. The divided parts are fixed from the root part, unit forces and moments are applied, and sectional beam properties are calculated with respect to the elastic axis. The methodology described in the article is then compared with the classical methods in the literature, and they showed that the new methodology predicted deflections better than other methods. However, the study also concluded that the generated BSM is unsuitable for dynamic analysis. Bindolino [16] assumed the wing torque box as a rectangle and created a stick model. The created stick model is used to reduce the mass of the wing torque box. Later, Cirillo [3] created BSM for a private jet using beam section constitutive laws. In this method, both static and dynamic characteristics are represented by the BSM. The created stick model is then used in discrete gust analysis. Palacios [17] described a method to create a stick model with nonlinear geometric effects using the 3D linear FEM model. The stick model is created using modal coordinates. Carrera et al. [18] modeled the beams with their component-wise formula. All the elements in a semi-monocoque structure are converted into beams. The model created by component-wise modeling is compared with the models created by Euler-Bernoulli [19] and Timoshenko [13] beam theories. Comparisons are made by performing static analysis. Pagani [20] made this formulation usable in dynamic aeroelasticity analysis. Cecrdle [21] published a conference paper on how the control surfaces without stiffness information, the engine attached to the wing, and the control surface tabs can be modeled as stick

models. Kratochví [22] developed a method for connecting control surfaces to lifting surfaces in the BSM. A particular beam element is created for this purpose. In this study, 9 degrees of freedom (DOF) is used instead of a FEM utilizing beam elements with the classic 6 DOF. It is shown that with the extra DOFs, beam elements represent the stiffness effect of the lifting surface and the control surface with a single beam. The stick model is then used in the flutter analysis in the article. Gupta et al. [23] developed a new method to convert nonhomogeneous and aperiodic 3D structures to BSM. In this method, the Variational Asymptotic Method (VAM) is used to determine the sectional properties in beams. Since VAM is inefficient in calculating complex sections, complex sections are replaced by more superficial structures that are equivalent in stiffness. Then, these sections are converted into beam elements using VAM. In this study, a surrogate model is used during stiffness matching. However, since a new surrogate model is needed for the new sections, a new method is deemed necessary. To solve this problem, Sarojini et al. [24] used a gradient-based optimizer instead of using the surrogate model in the stiffness-matching part. Then, VAM is used to convert this section into beam elements.

Given the advantages of employing optimization techniques in constructing BSM, Dunn's [25]–[29] works have gained significant prominence in this field. Dunn used genetic algorithms in his studies. Dunn noted that many features are optimized when creating stick models, and each beam feature drastically changed the results. These kinds of problems are nonlinear optimization problems. Dunn then stated that using a genetic algorithm to solve such problems would be appropriate. In his publications, he utilized the frequency response functions obtained from GVT to increase the fidelity of the BSM. Bending stiffness and mass distributions are utilized as design variables. Trivailo [30] defined the mass and stiffness properties of the beams as design variables and tried to reflect both the static and dynamic characteristics of the aircraft. A genetic algorithm was used in the optimization process. It is seen that natural frequencies close to GVT results are obtained with a 10% margin of error in the article. Thomas [31] created an optimized stick model using the differential evolution algorithm for a stick model created with the unitary loading method. It is

aimed to simulate the dynamic characteristics of the GFEM with the created stick model. In addition, since matrix-based ROMs better reflect the dynamic character of the aircraft compared to BSMs, he augmented the stiffness and mass matrices of the BSM by using the matrices from matrix-based ROM. Navratil [32] created a stick model for static aeroelastic analysis. The stick model creation process is as follows. First, deformation information from the GFEM is transferred to the aerodynamic model. Then, the deformation information obtained from the stick model is transferred to the aerodynamic model. Gradient-based optimization methods are used to simulate the deformation information of the two aerodynamic models. Beam properties are used as design variables.

A second method of creating ROMs is matrix-based ROM. These methods can be defined as reducing the dimensions of stiffness and mass matrices. Generally, they reflect the dynamic character of the aircraft better than BSM. However, these methods are not preferred in the aviation industry as they cannot be controlled as easily as BSM. In addition, they are not suitable for complex structures. The best-known among these methods is Guyan Reduction [33], [34]. This method selects some DOFs as primary and some DOFs as slaves. After this selection, a transformation matrix is created. By using the created transformation matrix, reduced stiffness and reduced mass matrix can be obtained. The Improved Reduction Method (IRS) [35] is an extension of the Guyan Reduction method, which involves selecting primary and slave DOFs for elimination from the system. Its objective is to address the errors arising from inconsistent handling of slave DOF masses in the Guyan Reduction method. In the IRS method, the mass matrix of the slave DOFs is re-diagonalized through a correction matrix to ensure that the reduced system precisely reflects the slave DOF masses. System Equivalent Reduction/Expansion Process (SEREP) [36] uses eigenvectors to create the reduced stiffness and mass matrix. Other popular matrix-based ROM methods are Craig-Bampton [37] and dynamic condensation [38].

CHAPTER 3

AEROELASTIC MODEL OF THE VERY LIGHT AIRCRAFT

3.1 Introduction

In this section, the process of creating the aeroelastic model of the METU VLA aircraft is explained in detail. The METU VLA aircraft is a joint project between METU and Turkish Aerospace Industries. The aircraft's design is handled by undergraduate students of METU, while Turkish Aerospace Industries provides consultation for the project.

Building an aeroelastic model is essential in evaluating and optimizing the aircraft structural performance. The aeroelastic model to be created consists of three main components: the structural model, the mass model, and the aerodynamic model.

First, the generation process of the structural model is discussed. Building the structural model is a mathematical representation of the aircraft's structure. In this process, the structural model is created using the MSC Patran program. Next, the mass model is explained. The mass model represents the mass distribution and interactions of the aircraft. Converting a density-based model to a lumped-based mass model is explained in detail. MSC Patran program is used in the mass model creation process. After completing the structural and mass models, the modal analysis is performed using MSC Nastran. The outputs of the modal analysis are the inputs of the optimization code that generates the BSM.

After the structural dynamics model is completed, the process of creating the aerodynamic model is started. In this respect, MSC Flight Loads module is used to create the aerodynamic model.

In order to enable the use of the model in aeroelastic analysis, spline creation is required to provide interaction between the structural and aerodynamic models. The splines created ensure that the deformations in the structure are transferred to the aerodynamic mesh, and the forces generated in the aerodynamic panels are transferred to the structure appropriately. This way, METU VLA aircraft is made suitable for aeroelastic analysis.

3.2 Structural Model

METU VLA GFEM is introduced in Figure 3.1 to 3.3.

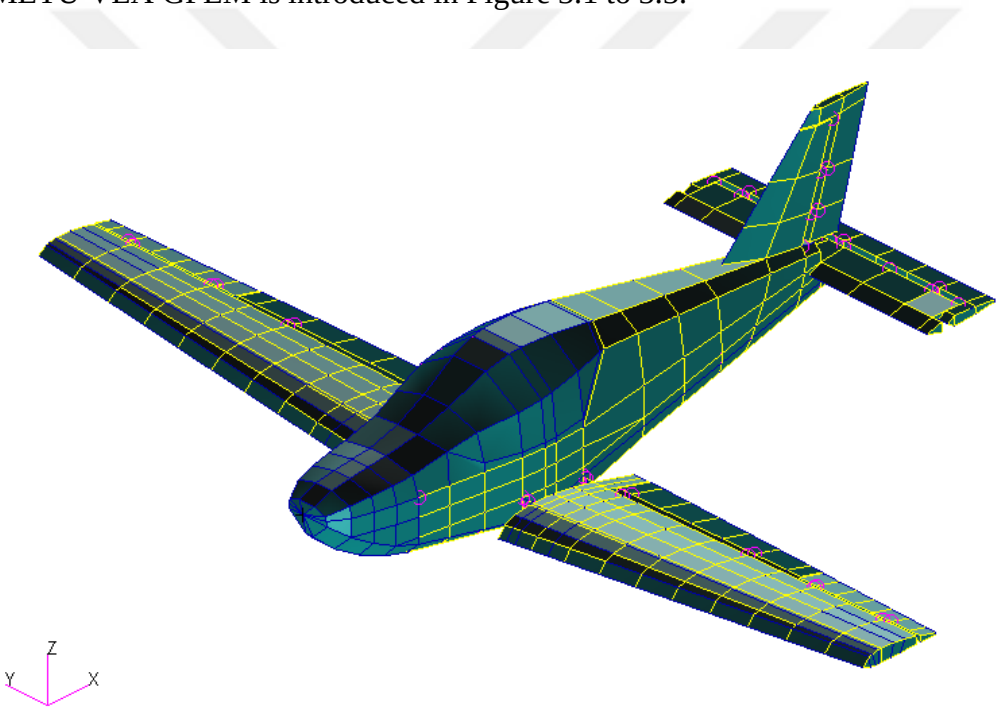

Figure 3.1 Isometric view of GFEM

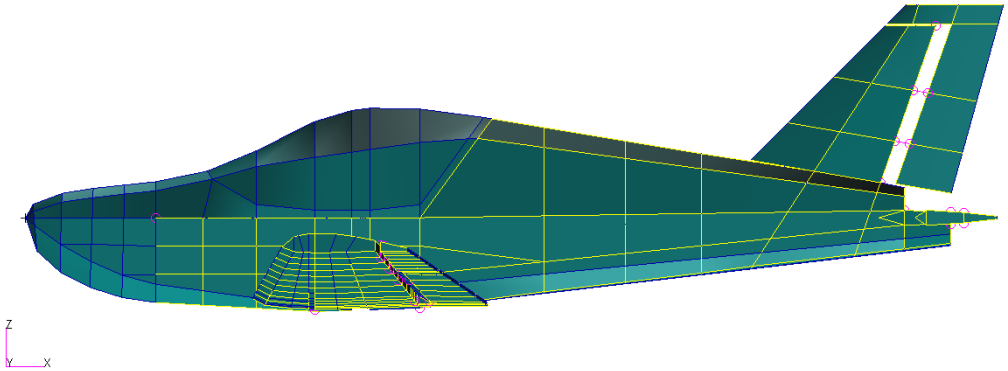

Figure 3.2 Side view of GFEM

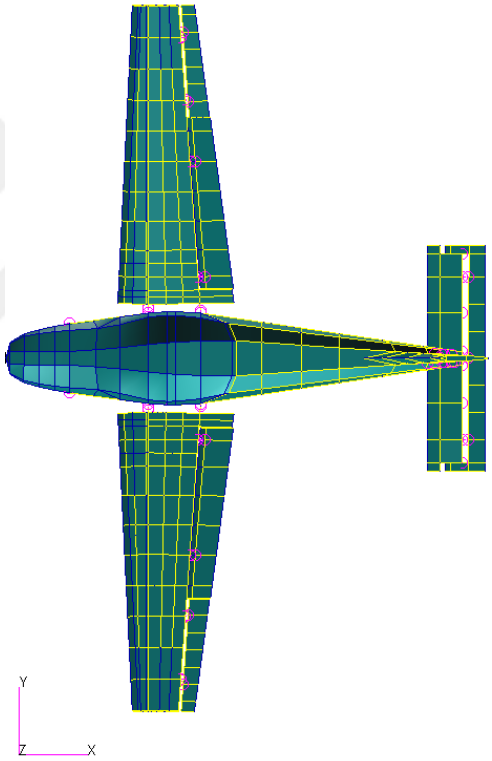

Figure 3.3 Top view of GFEM

The yellow-colored elements in Figure 3.1 to 3.3 represent beams. These elements have been used to model spar caps, rib caps, frame caps, longerons, and stringers. 2D shell elements are preferred for modeling ribs, webs, and skins. Area moment of

inertia in the GFEM is equivalent to the CATIA model for each cross-section. This criterion determines the height and width values of 1D beam elements. Aluminum is used as the material in the aircraft.

There are four types of control surfaces in the VLA. These are aileron, flap, elevator, and rudder. A lug and clevis mechanism connects the control surface and lifting surfaces. In GFEM, the fittings are modeled using RBE2 rigid elements. RBE2 rigid elements are used to model regions with high rigidity. It is assumed that the stiffness values of the lugs and clevis are considerably higher than the rest of the aircraft. The RBE2 elements merge on the hinge axis of the control surface. One RBE2 element is between the hinge axis and the lifting surface, while the other one is between the hinge axis and the control surface. The RBE2 element has two dependent nodes located on the upper and lower nodes of the rear spar of the lifting surface. The independent node is on the hinge line. Meanwhile, two dependent nodes of RBE2 elements on the control surface are on the upper and lower nodes of the front spar, with the independent node still positioned on the hinge line. There are coincident nodes between the two RBE2 elements. A CBUSH element is placed between these nodes. The CBUSH element allows adding springs hence stiffness to the model in our desired DOFs. By the virtue of this element, the force transmission directions required for the fittings are accurately depicted. This modeling approach is visually presented in Figure 3.4 and Figure 3.5.

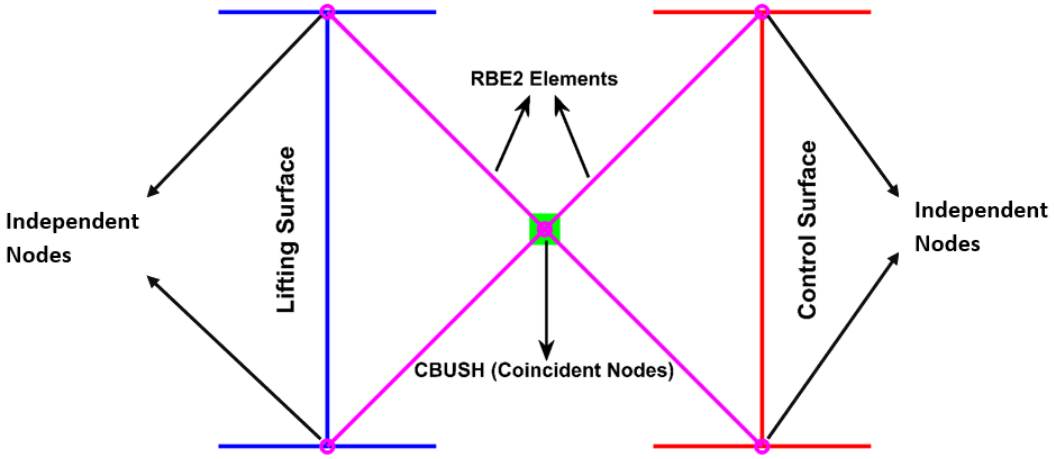

Figure 3.4 Connection between lifting surface to control surface (side view)

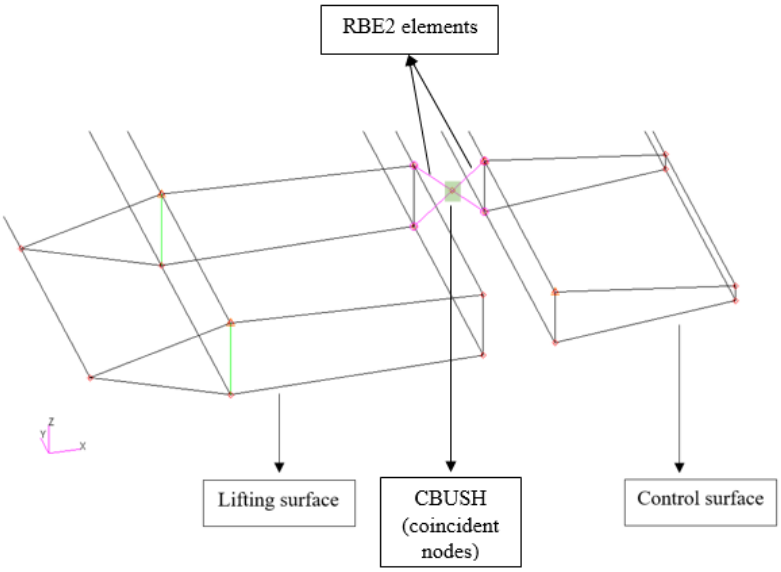

Figure 3.5 Fittings Modelling in GFEM

The CBUSH element shown in Figure 3.5 not only provides the force interaction between the lug and clevis but also acts as an element that balances the hinge moment of the control surface. The stiffness value that resists the hinge moment on the control surface is called the control loop stiffness. The dynamic stiffness values of the actuator are needed in order to obtain the control loop stiffness value correctly.

However, in this thesis study, the control surfaces' estimated control loop stiffness values have been determined. The determined values are converted to rotational spring and added to the CBUSH element.

Another element in the model is the RBE3 elements. These elements do not add any rigidity to the model. There are two reasons for adding RBE3 elements to the model. First, they ensure the distribution of lumped masses into the structural model. This is explained in detail in Section 3.3. The second reason is to find the average displacement of a particular region. RBE3 elements have one dependent node. The number of independent nodes can be from one to infinity. The displacement of the independent nodes represents the average displacement relative to the dependent node. The average displacements of the aircraft in certain sections in the GFEM are used as the displacement of the reference point in the BSM. In the modelling phase, RBE3 elements are used to represent the average displacement of the lifting surfaces of the aircraft along the elastic axis at the rib points. Dependent nodes of RBE3 elements are generated at the front spar points on the control surfaces and the center of gravity locations of the frames in the body. Every node where the dependent node of the RBE3 element in the GFEM is located, there is also the node where the beam elements of the BSM exist. The connection of RBE3 elements to ribs and frames is shown in Figure 3.6 and Figure 3.7. The purple elements in Figure 3.6 and Figure 3.7 are the RBE3 elements.

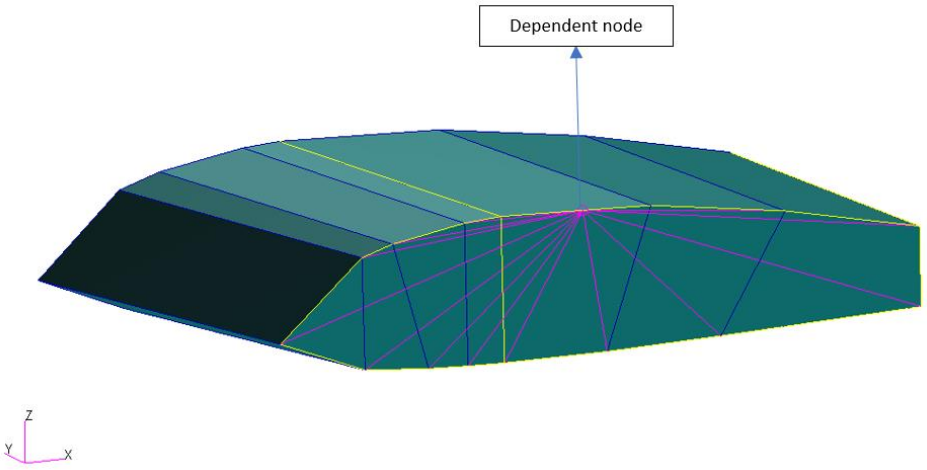

Figure 3.6 RBE3 element on the rib

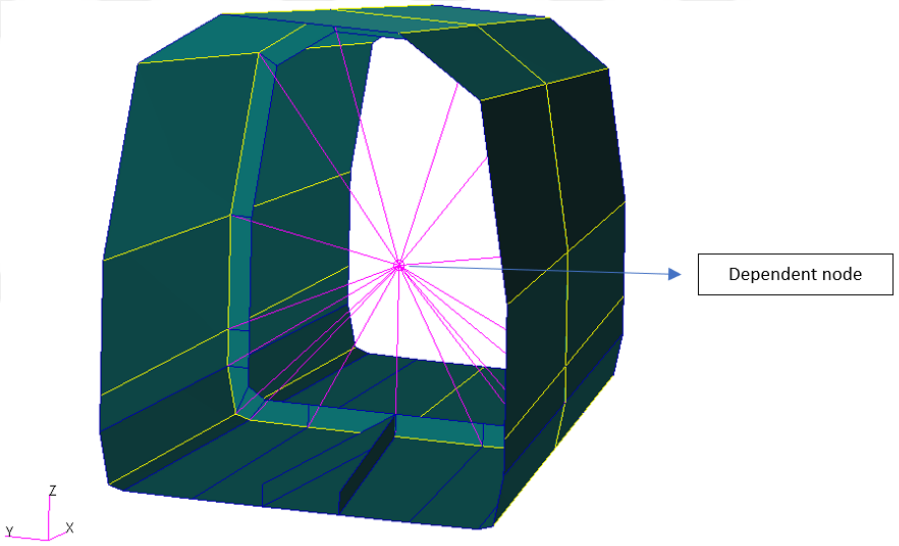

Figure 3.7 RBE3 element on the frame

The total number of nodes and elements used while creating the GFEM is given in Table 3.1.

Table 3.1 Element and node numbers in GFEM

Element Type	Topology	*Total in Model*
-	Node	1492
Shell	QUAD4	1502
Shell	TRIA3	90
Beam	BAR2	72
Rod	BAR2	1400
Bush	BAR2	24
0-D Mass	POINT1	86
Total elements		3174

QUAD4 and TRIA3 elements are used to model skins, ribs, and webs, BAR2 elements are used to model spar and rib caps, stringers, and POINT1 elements are utilized to model lumped masses.

3.3 Mass Model

Stiffness and mass models determine the dynamic characteristics of the aircraft. The density of the mass model and the way it is attached to the stiffness model directly affects the elastic modes of the aircraft.

A lumped-based model is preferred instead of a density-based mass model in the dynamic analysis of GFEM. There are three main reasons for this. These reasons are listed below.

- The first reason is that mass matrix of the lumped-based model is much sparser than density-based models. This is because, in lumped-based mass models, the mass is distributed to specific nodes only. However, in a density-based model, the mass must be distributed to all nodes, as the mass at each node is calculated based on the density information. In this case, more

calculations are required to calculate the mass, thus increasing the calculation time. In addition, each element in such matrices must be allocated a space in memory. However, sparse matrices use memory more efficiently, and solution time can be shortened using eigenvalue solution methods specific to sparse matrices. In particular, algorithms that work well with sparse matrices, such as the Lanczos algorithm, can be used effectively in eigenvalue solving. Using the Lanczos algorithm, software such as MSC Nastran also significantly shortens the eigenvalue solution time of sparse matrices. Consequently, lumped-based mass model significantly reduces the duration of the eigenvalue problems to be solved while performing the modal analysis.

- The second reason is that density-based mass models have local modes. Especially in models with large elements, it is inevitable to avoid having local modes in modal analysis. These local modes are unrealistic. They contaminate the analysis result.
- The third reason is that the lumped mass model to be created is used directly in the BSM creation process. Therefore, it contributes to the BSM creation process.

In this study, a density-based mass model is used during the development of the GFEM. The MSC Patran software's mass properties tool is utilized to convert a density-based mass model to a lumped-based mass model. This tool facilitates the determination of the center of gravity (CG) and mass moment of inertia values for the specified region. Lumped masses are created using CONM2 cards utilizing the calculated mass and CG values by the MSC Patran mass properties tool. Subsequently, the created lumped masses are distributed to the hard points of the corresponding region, such as the rib-spar connection and frames, utilizing RBE3 elements. This approach aims to prevent the formation of local modes by effectively distributing the mass to the hard points. The RBE3 elements, depicted in orange, are employed to disperse the lumped masses within the wing and fuselage, as illustrated in Figure 3.8 and Figure 3.9. In Figure 3.8 and Figure 3.9, each number represents a lumped mass.

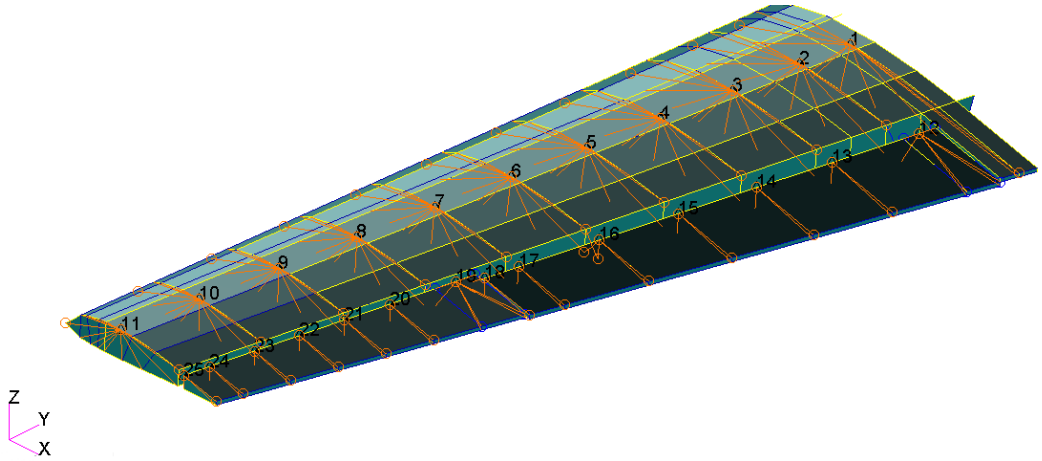

Figure 3.8 RBE3 elements used to distribute to lumped masses in the wing

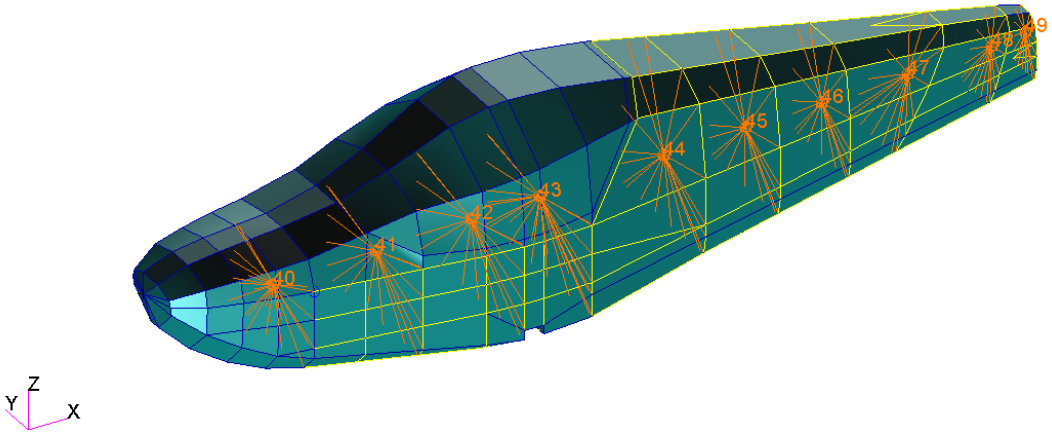

Figure 3.9 RBE3 elements used to distribute to lumped masses in the fuselage

The comparison of the dynamic analysis of the isolated torque box of the wing created with the density-based mass model and the isolated torque box made with the lumped-mass model is given in Table 3.2. Too many local modes exist in the density-based model of the entire aircraft. Therefore, the torque-box model is preferred instead of using the whole aircraft in the comparison.

Table 3.2 Comparison of density-based and lumped mass models of the torque-box of the wing

Mode Identification	Density-Based Mass Model [Hz]	Lumped-Mass Model [Hz]	Difference [%]
First bending (out of plane)	15.32	15.37	0.33
First bending (in plane)	47.64	47.87	0.47
Second bending	59.89	59.38	0.85
First torsion	100.17	99.50	0.67
Second bending (in plane)	111.33	111.12	0.15

A total of 86 lumped masses are used in GFEM. The distribution of the lumped masses used is given in Figure 3.10.

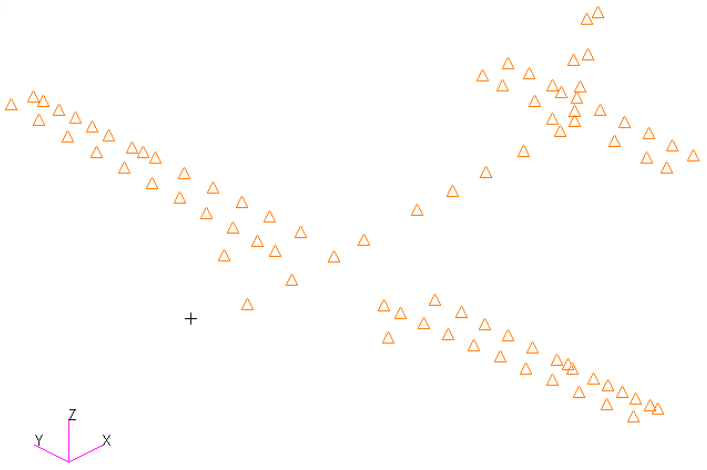

Figure 3.10 Lumped mass distribution in the GFEM

The mass, CG, and mass moment of inertia values of the aircraft are given in Table 3.3. The nose of the aircraft is the origin of the coordinate system.

Table 3.3 Mass Properties of the GFEM

Mass Properties	*Direction*	*Value*
Mass [kg]	-	716.72
CG [mm]	x	2176.32
CG [mm]	y	-0.8866
CG [mm]	z	-168.31
Mass moment inertia at CG [kg.mm^2]	xx	1.00e+9
Mass moment inertia at CG [kg.mm^2]	yy	8.51e+8
Mass moment inertia at CG [kg.mm^2]	zz	1.71e+9
Mass moment inertia at CG [kg.mm^2]	xy	2.26e+6
Mass moment inertia at CG [kg.mm^2]	xz	-7.76e+7
Mass moment inertia at CG [kg.mm^2]	yz	6.79e+5

3.4 Modal Analysis

This section explains the theory of modal analysis of free vibration of undamped multi-degree of freedom (MDOF) systems. The MSC Nastran normal mode analysis (SOL103) module is then used to conduct the modal analysis of the GFEM. This study aims to identify the elastic modes that provide the basis for assessing dynamic aeroelasticity and the subsequent development of the BSM. A critical step in effectively representing the dynamic behavior of the aeroelastic system under investigation is the choice of suitable elastic modes.

The most general form of the equation of motion of a linear system is given in Equation 3.1.

$$[M]\{\ddot{q}\} + [C]\{\dot{q}\} + [K]\{q\} = \{Q\} \tag{3.1}$$

where [M], [C], and [K] are the mass, damping, and stiffness matrix, respectively. These matrices are symmetrical. The sizes of the specified matrices are the DOF x DOF. q and Q are displacement and force column vectors. Since the system to be

solved is undamped and free vibration, $[\mathrm{C}] = [0]$ and $\{\mathrm{Q}\} = \{0\}$. After simplification, the equation of motion of free vibration of undamped systems is given in Equation 3.2.

$$[M]\{\ddot{q}\} + [K]\{q\} = \{0\} \tag{3.2}$$

At this point, the solution of the system is assumed to be in the form of simple harmonic motion given by $\{q\} = \{u\}e^{i\omega t}$. Equation 3.3 is obtained when the assumed harmonic solution is substituted into Equation 3.2. Equations 3.4 and 3.5 are obtained when necessary simplifications are made.

$$-\omega^2[M]\{u\}e^{i\omega t} + [K]\{u\}e^{i\omega t} = \{0\} \tag{3.3}$$

$$\big[[K] - \omega^2[M]\big]\{u\}e^{i\omega t} = \{0\} \tag{3.4}$$

$$\big[[K] - \omega^2[M]\big]\{u\} = \{0\} \tag{3.5}$$

Equation 3.5 has trivial solution. $\{u\} = \{0\}$ corresponds to the case where there is no vibration in the system. In Equation 3.5 the number of homogeneous algebraic equations is equal to the total number of DOF in the GFEM. Unknown displacement vector (u) represents the degree of freedom vector, and the frequency is denoted by ω^2. The determinant of the $\big[[K] - \omega^2[M]\big]$ part in Equation 3.5 must be set to zero in order to find the nontrivial solution of u.

$$\det\big[[K] - \omega^2[M]\big] = 0 \tag{3.6}$$

The solution of Equation 3.6 gives us ω as the number of DOF. These values are the natural frequencies of the system.

After obtaining the natural frequencies, Equation 3.5 can be solved for the eigenvectors which are the mode shapes in the free vibration problem. Since the equations are linearly connected, any one of the equations can be ignored. Then, by choosing an arbitrary value for one unknown and substituting the particular natural frequency into Equation 3.5, DOF-1 unknowns and DOF-1 equations can be

obtained. Then, u values can be found for each ω value. Each vector u represents the mode shape corresponding to the natural frequency.

3.4.1 Modal Analysis Results of the Global Finite Element Model

Elastic modes of the GFEM up to 90 Hz are given in Table 3.4. S denotes the symmetric mode shape, and A means the antisymmetric mode shape in Table 3.4. As the natural frequency values increase, their effect on dynamic aeroelasticity analysis generally decreases. For this reason, the effect of elastic modes after 90 Hz on dynamic response or flutter analysis is insignificant. In addition, local modes are effective in elastic modes after 90 Hz. These modes are unrealistic.

Table 3.4 Modal Analysis Results of the GFEM

Mode #	Mode Identification	Natural Frequency [Hz]
1	Wing first bending – aileron rotation (S)	12.35
2	Aileron rotation (A)	16.97
3	Aileron & flap rotation (out of phase) (S)	18.02
4	Flap rotation (A)	18.85
5	Aileron & flap rotation (in phase) (S)	19.09
6	Elevator rotation (S)	21.66
7	Wing first bending – aileron rotation (A)	23.12
8	Horizontal tail first bending-vertical tail first bending-elevator first bending(A)	27.35
9	Vertical tail first bending (A)	30.65
10	Rudder rotation (A)	32.70
11	Horizontal tail first torsion – elevator first bending (S)	33.60
12	Vertical tail in-plane motion (S)	36.65

Table 3.4 continued

13	Wing in-plane bending – vertical tail in-plane motion(S)	39.12
14	Rudder in-plane motion (S)	41.06
15	Wing in-plane bending (A)	46.69
16	Wing second bending (S)	52.36
17	Elevator first torsion – horizontal tail first bending (S)	53.26
18	Horizontal tail in-plane bending (A)	54.76
19	Wing second bending (A)	62.56
20	Flap in-plane bending (S)	67.18
21	Flap in-plane bending (A)	68.44
22	Flap first bending (S)	69.65
23	Flap first bending (A)	70.40
24	Horizontal tail first torsion – elevator second bending (A)	76.81
25	Vertical tail first torsion - rudder first bending (A)	82.55
26	Horizontal tail first torsion (S)	83.67
27	Wing first torsion (S)	85.42

Modes 12, 13, 14, 15, 18, 20, and 21 are omitted from the dynamic analysis. This is because these modes include in-plane bending. In order to capture these modes correctly, the fasteners in the GFEM must be realistically modeled. In addition, the effect of in-plane motions on dynamic aeroelasticity analysis is much less than out-of-plane motions. While creating the BSM, the specified in-plane motion modes are not reflected. Two of the elastic modes extracted from dynamic analyses are given in Figure 3.11 and Figure 3.12 in order to provide a clearer understanding of in-plane motions.

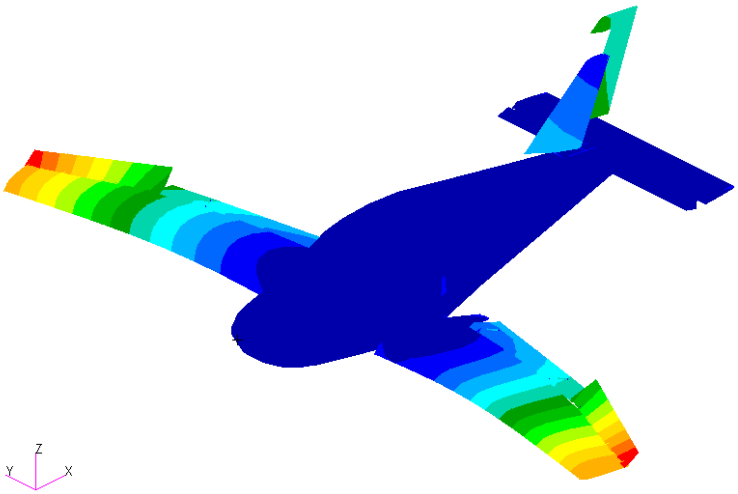

Figure 3.11 Wing in-plane first bending – vertical tail in-plane motion (mode 13)

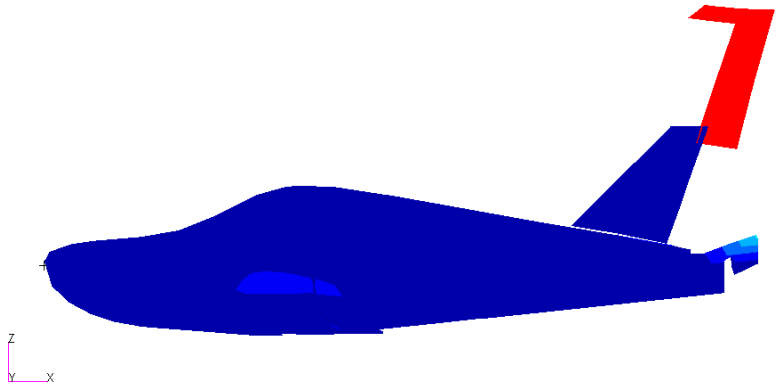

Figure 3.12 Rudder in-plane motion (mode 14)

3.5 Aerodynamic Model

Aeroelasticity is the discipline that studies the interaction of structure and aerodynamics. Therefore, the aerodynamic model is vital in aeroelasticity analysis. The aerodynamic model must compute the proper aerodynamic forces and appropriately depict the flow around the structure. An incorrect or inadequate aerodynamic model may yield inaccurate results in analyses of dynamic aeroelasticity and may erroneously predict the vibrations and deformations that the

structure would experience under actual conditions. This can have catastrophic consequences for the aircraft.

In this study, the aerodynamic model is created using MSC FlightLoads. MSC Nastran uses the Doublet-Lattice method (DLM) in the subsonic region on interfering lifting surfaces [39]. The linearized aerodynamic potential theory lies behind this method. DLM is an extended method of the steady Vortex-Lattice method for unsteady flows. The unidentified lifting pressures are assumed to be evenly distributed over each box's one-quarter chord line. Each box has a single control point centered spanwise on its three-quarter chord line and at which the surface normal wash boundary condition is satisfied. DLM is widely used for aeroelastic analysis in the aviation industry. This is because it gives fast and reliable results in subsonic regions.

Some points to be considered while creating aerodynamic modeling are as follows.

- Aerodynamic elements are flat plates and must be modeled parallel to the flow [40].
- Wing, horizontal tail, vertical tail, and control surfaces are considered lifting surfaces. Unique aerodynamic panels have been created for each lifting surface.
- The aerodynamic effects of the fuselage are minor in aircraft like METU VLA. In such aircraft, flutter mechanisms are usually caused by the coupling mechanisms of the wing, horizontal and vertical tail, or control surfaces. For this reason, the fuselage is not included in the aerodynamic model. However, in aircraft configurations where the effects of the fuselage may be more significant, aerodynamics should be included in the model.
- It is advised to focus aerodynamic boxes close to the hinge lines, trailing edge, and leading edge [40].
- As shown in Figure 3.13, all elements in the wing and tail spanwise must be aligned. If this condition is not met, the vortex lines generated by the wing crosses the tail's aerodynamic boxes. Due to the singularity of

the aerodynamic matrix at the vortex line, the downwash effect on the tail is unreasonably strong [41].

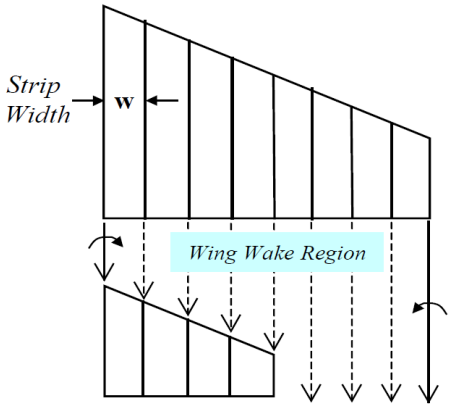

Figure 3.13 Alignment of the elements for wing and horizontal tail [41]

- At least 12 elements along the chordwise are needed to represent a sine wave properly [41]. For this reason, at least 12 aerodynamic elements are used in each section.

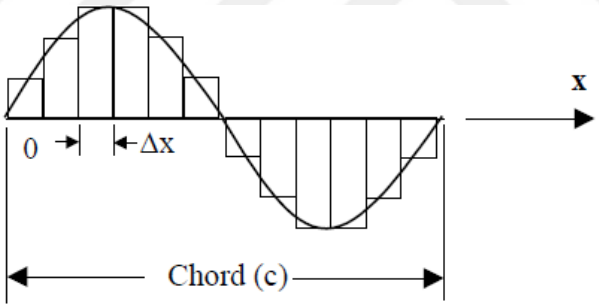

Figure 3.14 Sine-wave representation with aerodynamic boxes [41]

- DLM demands that boxes have an aspect ratio of no more than three. However, the closer the aspect ratio is to one, the better.
- As shown in Figure 3.15 and Figure 3.16, when making the aerodynamic model of the two wings, an aerodynamic panel should be modeled to combine the right and left wings. This bridge panel prevents an unrealistic strong vortex on the inboard parts of the wing [41].

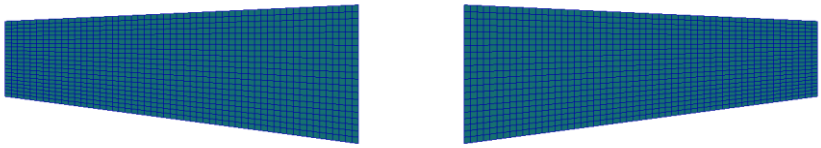

Figure 3.15 Incorrect modelling

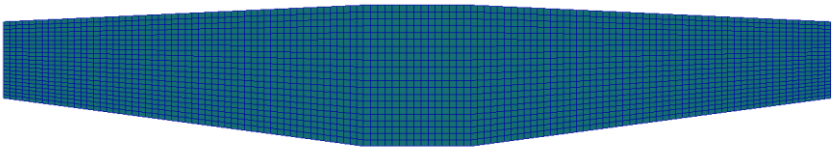

Figure 3.16 Correct modelling with the bridge panel

The aerodynamic model created by following the specified rules is given in Figure 3.17. A total of 3255 aerodynamic elements are used in the model.

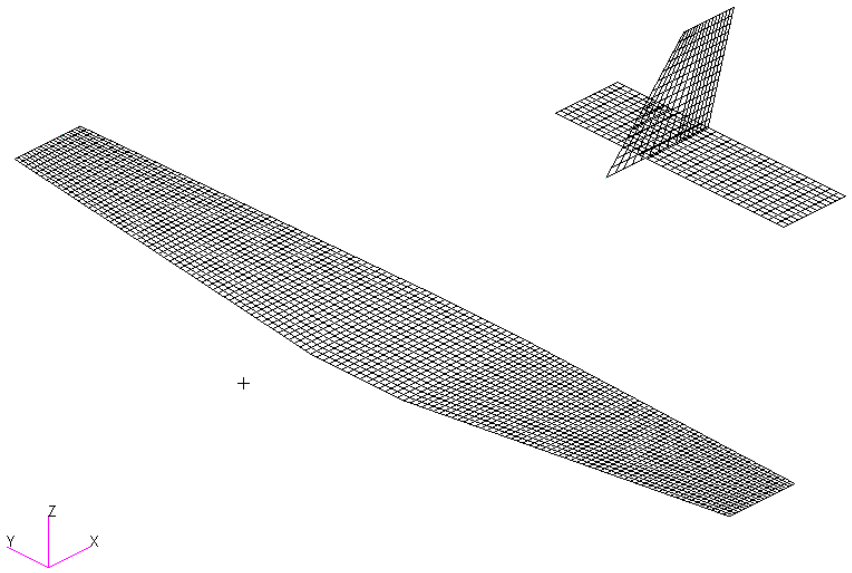

Figure 3.17 Aerodynamic model of the VLA

3.6 Aero-structure coupling

The spline matrix provides communication between the aerodynamic model and the structural model and allows the displacements calculated in the structural model to be transferred to the aerodynamic model.

$$\{h\} = [G]\{q\} \tag{3.7}$$

In Equation 3.7, h represents the interpolated displacement vector for aerodynamic boxes, G represents the spline matrix, and q represents the displacement vector in the structural model. The spline matrix also transfers aerodynamic loads to the structural model. Equation 3.8 can be expressed using the virtual work principle.

$$\{\delta h\}^T\{F_h\} = \{\delta q\}^T\{F_a\} \tag{3.8}$$

In Equation 3.8, F_a stands for aerodynamic forces on the structural element, while F_h represents aerodynamic forces on aerodynamic boxes. δh and δq represent virtual displacement vector on aerodynamic and structural grids, respectively.

By inserting Equation 3.7 into Equation 3.8, Equation 3.9 is obtained.

$$\{\delta q\}^T([G]^T\{F_h\} - \{F_a\}) = 0 \tag{3.9}$$

Since the virtual displacement vector cannot be equal to zero, the term inside the parenthesis in Equation 3.9 must be set to zero. Hence, after the spline matrix G is created, utilizing the transpose of the spline matrix G, one can transfer forces from the aerodynamic boxes to the structural finite element grid points, as given by Equation 3.10.

$$\{F_a\} = [G]^T\{F_h\} \tag{3.10}$$

MSC Nastran has many spline methodologies. Among these, infinite plate spline (IPS) [42] the industry's most widely used spline methodology, is used while preparing the aeroelastic model. The IPS approach should be applied if the FEM includes wing-like components and plate-type elements [41].

The reason for many errors in aeroelastic analysis is to create incorrect spline inputs. For this reason, it is necessary to carefully select the structural nodes that are used in the spline matrix. Some considerations when choosing spline nodes are as follows.

- The principle of virtual work guarantees the conservation of the total force, but not the conservation of moment. It is advised that the structural grid points chosen for the spline be coarser than the aerodynamic grid points in order to ensure accurate force splines. The moment distribution to the structural grid is affected if more than one structural grid point is present within a single aerodynamic box [43].
- All aerodynamic grids should be included within the domain of the structural grids to prevent extrapolation. Extrapolation can result in distortion. Structural models are often narrower than aerodynamic models, as the fairings are not modeled. In order to solve this problem, it is advised that additional grid points be added at the leading/trailing edges of the wing and that these new grids be connected to their neighboring grid points via rigid elements like RBE2 in MSC Nastran. In addition, structural nodes close to the intersection of the two aerodynamic panels are selected for the splined nodes of both panels. This allows the structural nodes to cover the aerodynamic model in the spanwise direction. This approach also aims to prevent discontinuities between panels and improve the accuracy of the analysis.
- Only lower skin or upper skin nodes should be selected for splining the nodes. If the upper and lower nodes are selected simultaneously, ill-conditioned or singularity can occur in the spline matrix.
- The nodes to be splined must be hard points of the aircraft. These nodes can be on the spars, ribs, or frames. Otherwise, local modes that may occur may contaminate the results of the aeroelastic analysis.

The splined nodes in the structural model are highlighted in Figure 3.18 and Figure 3.19.

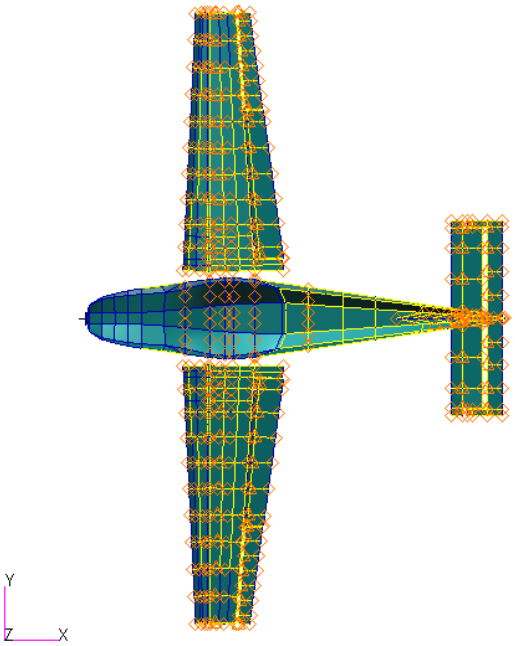

Figure 3.18 Top view of splined nodes

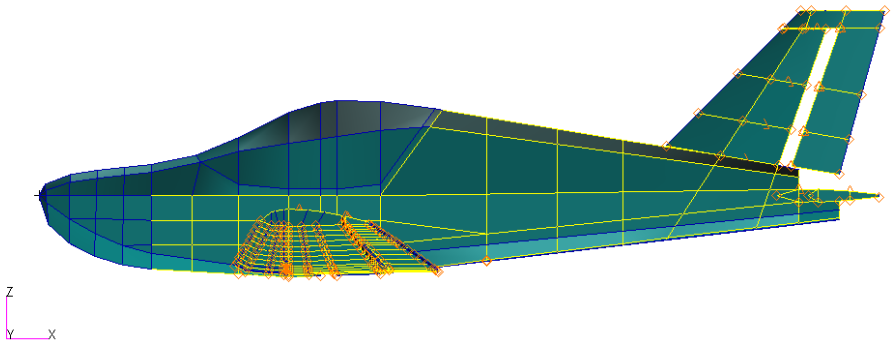

Figure 3.19 Side view of splined nodes

Spline validation may be carried out by precisely reflecting the deformations that occur in the structural model to the aerodynamic model. As a result, the aerodynamic model and GFEM elastic mode responses are provided in Figure 3.20.

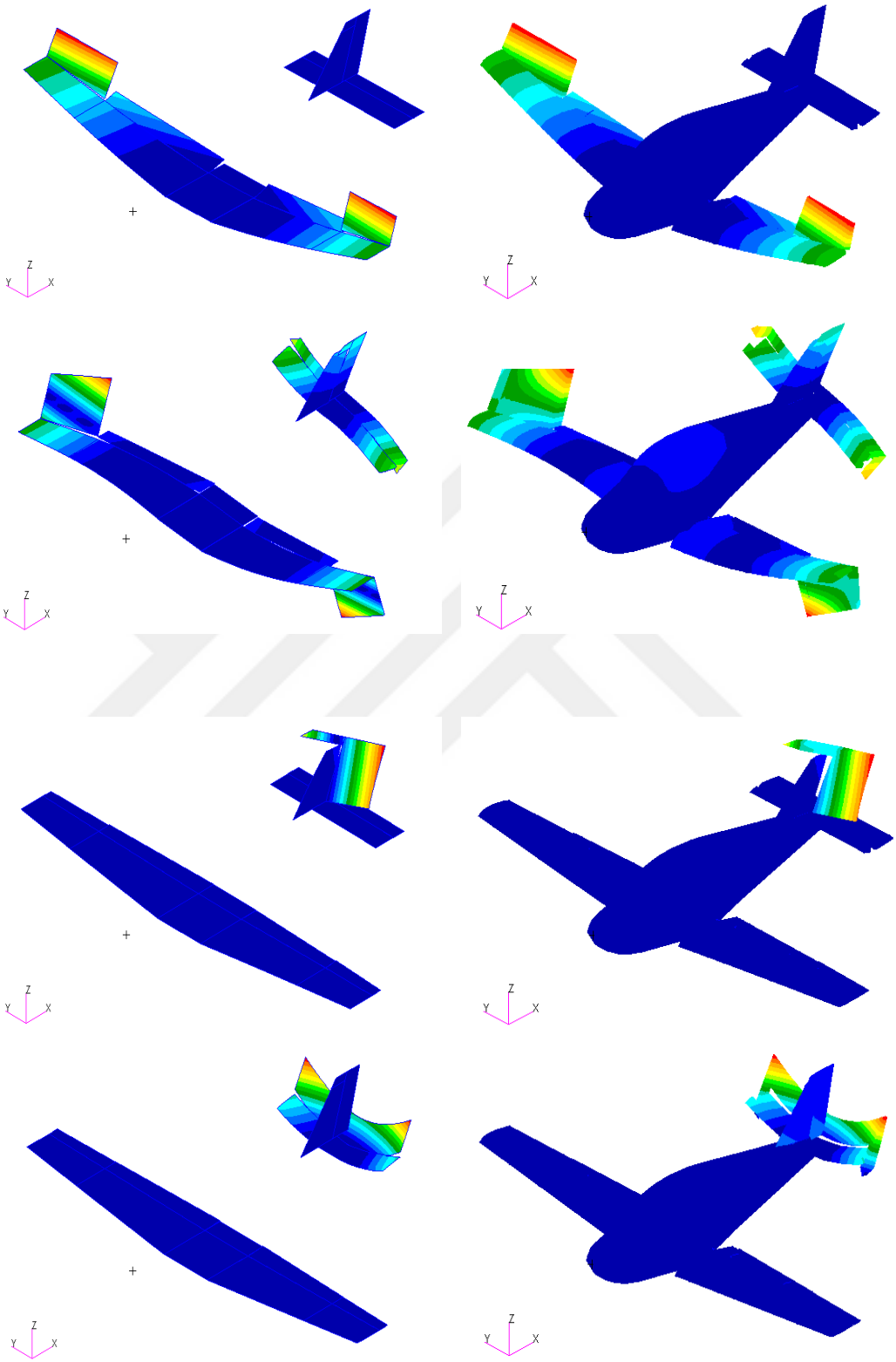

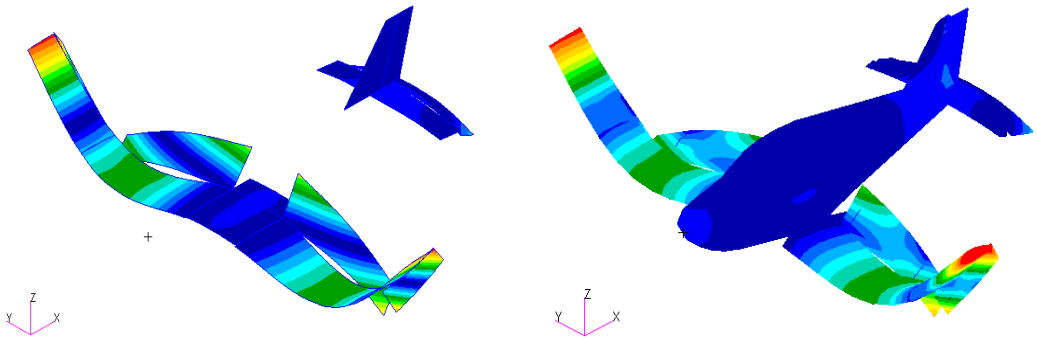

Figure 3.20 Spline Verification of the VLA (left aerodynamic model, right GFEM)

The elastic modes shown in Figure 3.20 have been carefully chosen to show the movement of all components, ensuring that all parts are properly splined. Both the aerodynamic model and the structural model displayed similar behavior. This demonstrates that the selected spline nodes are appropriately selected.

CHAPTER 4

OPTIMIZATION METHOD USED IN GENERATING BEAM STICK MODEL

4.1 Introduction

This section explains the global optimization code developed to create the BSM. The global optimization code used in this study is inspired by CSA [4]. For this reason, CSA is described in the first part. Then, information about some modifications made in the CSA algorithm is given in Section 4.3. These modifications aim to make specific steps of the CSA algorithm better suited to the problem studied. Section 4.4 presents details of design variables and objective functions. Finally, Section 4.5 is completed by explaining the steps of the modified CSA algorithm.

4.2 Crow Search Algorithm

Optimization algorithms can be classified under three main headings. These are enumerative, calculus-based, and global optimization methods. Global optimization methods are divided into heuristic, meta-heuristic, and random search. Classification of the meta-heuristic algorithms is given in Figure 4.1. CSA is classified as a swarm intelligence meta-heuristic algorithm. In recent years, a wide range of optimization problems have been effectively solved using meta-heuristic methods. These algorithms yielded successful results in health, economics, and engineering problems. The majority of severely nonlinear real-world optimization problems have demonstrated encouraging results when solved with meta-heuristic algorithms.

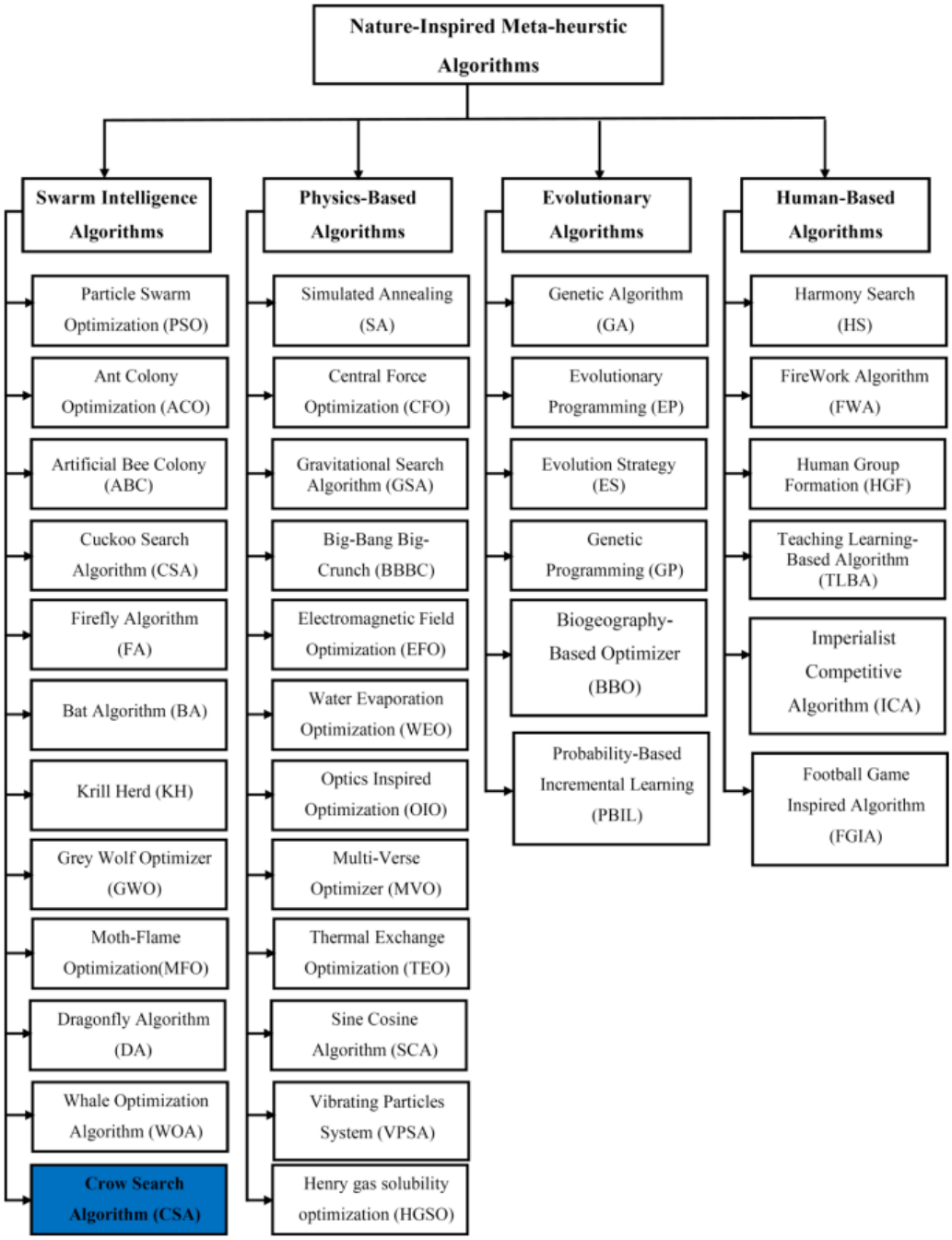

Figure 4.1 Taxonomy of the meta-heuristic algorithms [44]

CSA is developed with inspiration taken from crows. The optimization algorithm is based on the basic idea of memory abilities, communication skills, and social

behavior of crows toward food storage. The crow-inspired behaviors of the algorithm are listed below.

- Crows live in a social order.
- Crows have an extraordinary memory. Crows remember their food storage location and do not forget this information for a long time.
- Crows always seek a more efficient food source. Therefore, they follow each other to steal another crow's food.
- Crows are animals known for their clever behavior. If they realize that they are being followed, they fly to a random area to protect their food from other crows. However, they are likely to find a more fertile food zone in a random area.

The goal of the CSA is that crow i should be able to follow another crow j to find its hidden food source. During this process, crow i must continuously update its position. Additionally, if crow i perceives a danger of being caught while attempting to steal the food, it must alter its position. The CSA utilizes two matrices as the fundamental components for implementing these functionalities into the algorithm.

The first matrix is an x matrix that determines the position of the crows. The size of this matrix should be flock size times the number of design variables. In a sense, it is a d-dimensional environment. Each design variable is the coordinates of the crows' positions. Second, a memory matrix (m) is needed. The size of the m matrix is the same as the x matrix. This matrix stores the position of the best food zone up to the current number of iterations of the crows. This matrix represents the extraordinary memories of the crows. Two different possibilities can arise in each iteration of the algorithm.

In the first state, crow j is unaware of being followed by crow i. In this case, the new position of the crow i, which follows the crow j, is determined using Equation 4.1.

$$x^{i,iter+1} = x^{i,iter} + r_i * fl^{i,iter} * \left(m^{j,iter} - x^{i,iter}\right) \quad (4.1)$$

In Equation 4.1, i and j define the identity of the crow in the flock. i and j can take a value between one and the flock size. '$iter$' refers to the number of iterations. '$iter$' can take a value from one to the maximum number of iterations. The meanings of the symbols used in Equation 4.1 are as follows.

- x: Position matrix
- fl : Flight length
- r : Random number with a uniform distribution between 0 and 1
- m : Memory matrix

The new position of the crow is affected by flight length (fl), as shown in Figure 4.2.

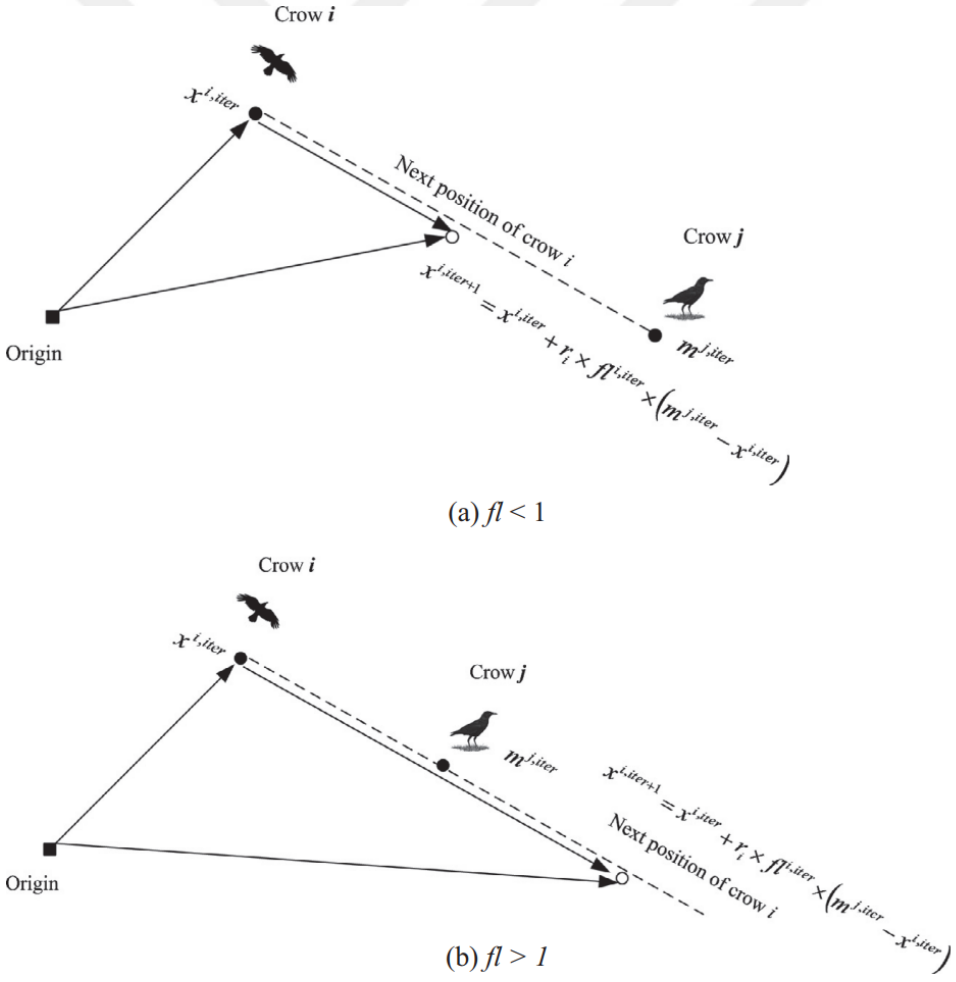

Figure 4.2 Effect of fl on the position of the crow (a) for fl < 1 (b) for fl > 1 [4]

Large values of the fl lead to global search, and small values to local search [4]. Any location on the dashed line in Figure 4.2 can be the new position of the crow.

In the second case, crow j becomes aware of being followed. In this case, crow j wants to protect its food by deceiving crow i by going to another random location in the search space. In this case, the position of crow i is randomly determined.

The occurrence of first state (Equation 4.2) or second state (Equation 4.3) depends on the awareness probability (AP). If the random number selected during iteration falls below the AP threshold, Equation 4.3 holds, otherwise, Equation 4.2 holds.

$$x^{i,iter+1} = x^{i,iter} + r_i * fl^{i,iter} * \left(m^{j,iter} - x^{i,iter}\right) \quad if, \quad r^j > \mathrm{AP}^{\mathrm{j,iter}} \quad (4.2)$$

$$x^{i,iter+1} = Random\ position \quad if, \quad r^j < \mathrm{AP}^{\mathrm{j,iter}} \quad (4.3)$$

$\mathrm{AP}^{\mathrm{j,iter}}$ represents the AP of crow j. AP is a number between 0 and 1 and is a parameter entered as an input to the optimization code. AP is related to the intelligence of crows. For example, if an AP close to one is chosen, most crows know that they are being followed. For this reason, crows fly to random areas, and this increases the probability of the second state, Equation 4.3. Choosing a number close to one for AP increases diversification. In this case, crows search a broader area. This reduces the search frequency in a good place. If the AP is chosen a number close to zero, the probability of the first situation (Equation 4.2) increases. In this case, crows generally perform a local search, and the likelihood of finding the global optimum decreases. Therefore, this parameter should be selected according to the problem type. Suggested value of AP is 0.1 according to Askarzadeh [4].

The CSA is itemized step-by-step.

1. Objective function, flock size, maximum iteration number, flight length, and awareness probability should be determined.
2. A random matrix should be given to the position matrix. Since the crows do not have any experience at the beginning, the position matrix and the memory matrix must be synchronized.

3. The objective function should be calculated for each crow.
4. At this stage, the new position of the crow is determined. In this case, there are two different possibilities. Equation 4.2 or 4.3 determines the new position of the crow i. This is repeated for each crow in the flock.
5. The suitability of the crow's new position is tested at this stage. If the crow's new position does not satisfy the constraints, the position of the crow is not changed.
6. The objective function is recalculated for the new position of the crows.
7. At this stage, the memory matrix of the crows is updated. If the objective function calculated according to the updated position of the crow is better than the memory matrix, the memory matrix is updated. If the memory matrix is better, the memory matrix does not be changed.
8. In this case, whether the termination criterion has been reached is checked. If the code reaches the maximum iteration number, it will stop. If it doesn't reach, it will repeat from Step 4 until it reaches the maximum number of iterations.

4.3 Modified Crow Search Algorithm

When building a BSM that accurately represents the aircraft's dynamic characteristics, it is necessary to have two objective functions. The first objective function should calculate the difference in natural frequencies between the GVT results or 3D FEM and the BSM. The second objective function should compare the similarity of the mode shapes. The original CSA includes a single objective function. In this study, a second objective function is added to the CSA, turning the problem into a multi-objective optimization.

In multi-objective optimization problems, conflicting objective functions make it difficult to find the optimum solution. For example, while generating the BSM, there may be cases where the natural frequencies are well matched, but the mode shapes have very low similarity to the GFEM. The Pareto optimal method is one method to

find which solution is more efficient in multi-objective optimization problems. The Pareto optimal solution is used when not all objective functions can be optimized simultaneously. In this case, a Pareto optimal set is created. The terms dominance and non-dominance are used to find the Pareto optimal set. A domination relation occurs when one solution performs better than another solution in at least one objective function and is at least equal in any other objective function. All non-dominance solutions form the Pareto optimal set.

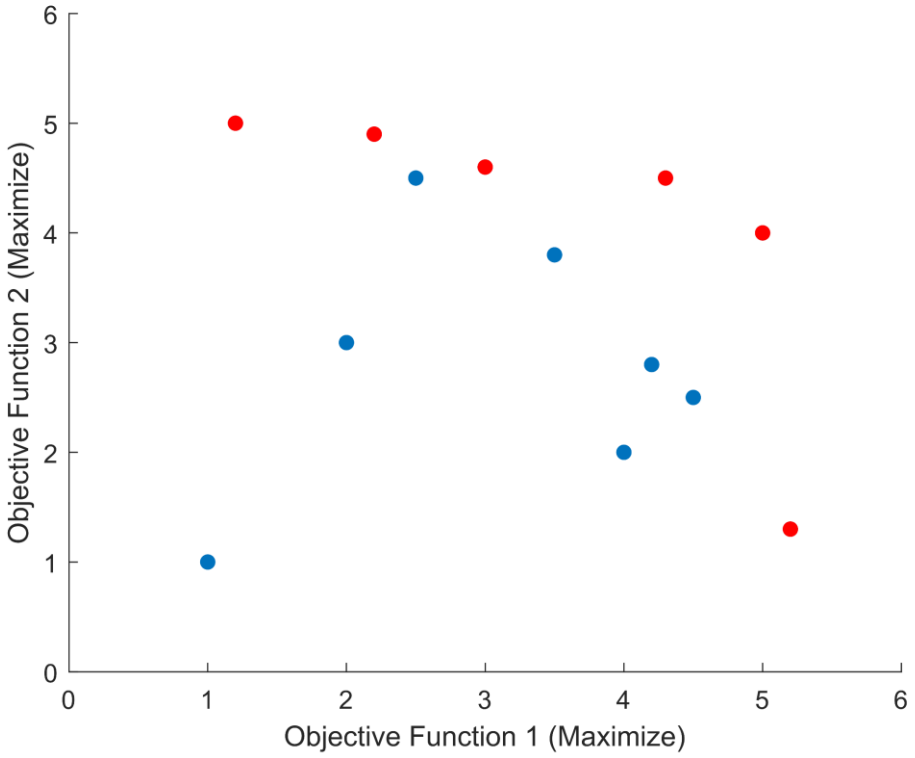

Figure 4.3 Pareto optimal solutions

In Figure 4.3, the Pareto optimal solution set is highlighted in red. The algorithm's primary objective is to group situations that do not have a clear advantage over each other and improve their chances of selection. Despite the red circles outperforming the blue circles in Figure 4.3, they cannot provide an advantage over each other.

Therefore, each option could be the best for the user. The ultimate decision is left up to the user.

Another feature added to the algorithm is the variable AP. As the number of iterations increases, the AP gradually decreases. The main reason is that the crows approach the fertile region as the number of iterations increases. When this happens, the decrease in AP reduces the random search rate and focuses on the efficient area. With this change, the crows reach a better location at much lower number of iterations.

4.4 Design Variables and Objective Functions

Since the global optimization method is used in this study, design variables and objective functions must be defined.

Section 3.4 explains how to find the eigenvalues and eigenvectors of the system. Two critical factors affecting the dynamic characteristics of a system are mass and stiffness. For this reason, all parameters affecting the mass matrix and stiffness matrix can be selected as design variables. However, in this optimization code, the mass matrix parameters are not considered as design variables. The mass matrix is given as direct input to the code. The mass matrix preparation process, which is given as input to the code, is as follows.

- Conversion from a density-based mass model to a lumped-based mass model is performed as described in Section 3.3.
- The lumped mass elements created in the GFEM are directly connected to the nearest nodes of the BSM.
- BSM's mass matrix is exported directly using MSC Nastran.

The parameters affecting the stiffness matrix are used as design variables. Typical beam element is illustrated in Figure 4.4. The parameters used as design variables for each beam element are listed below.

- Elastic modulus
- Shear modulus
- I_{zz} (Area moment of inertia about the z direction)
- I_{yy} (Area moment of inertia about the y direction)
- J (Polar moment of inertia)
- $Area$ (Cross-sectional area)

The Nastran PBAR card is utilized when defining beams in the FEM [45]. This card allows the direct integration of the design variables into the beam element. Thus, instead of altering the height and width of the beam to optimize its inertia values, the inertia values themselves can be used as design variables.

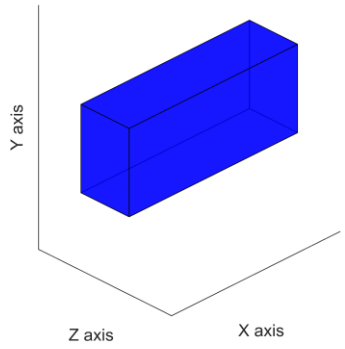

Figure 4.4 Representation of beam element

This optimization code uses two objective functions, as stated in Section 4.3. In this optimization code, objective functions are tried to be minimized. The BSM primarily aims to simulate the natural frequency and mode shapes of the test data coming from GVT or GFEM. Therefore, the first objective function compares the natural frequencies of the 3D GFEM with the natural frequencies of the BSM. The second objective function leverages the Modal Assurance Criteria (MAC) to compare the mode shapes. MAC is used to compare the mode shapes of two different systems. It

outputs a number between zero and one. As the MAC output gets closer to one, it is concluded that the mode shapes of the two systems are similar.

First, the construction of the objective function, which is related to the natural frequency, is explained. In this example, two natural frequencies are considered to explain the methodology. If more than two frequency ratios are to be taken into consideration, it should be added to the formula similarly.

$$a_1 = (|1 - F_{r1}| + |1 - F_{r2}|) \tag{4.4}$$

$$\begin{aligned} p_1 = {} & minimum(0, F_{r1} - 0.9)^2 + minimum(0, 1.1 - F_{r1})^2 \\ & + minimum(0, F_{r2} - 0.9)^2 + minimum(0, 1.1 - F_{r2})^2 \end{aligned} \tag{4.5}$$

$$f_1 = a_1 * (1 + c_1 * p_1) \tag{4.6}$$

In Equation 4.4, F_{ri} stands for the frequency ratio of mode i calculated as the ratio of the natural frequency taken from the GFEM or test data to the natural frequency output of the optimization iteration, which is the natural frequency calculated by the BSM. The purpose of the a_1 function is to obtain F_{ri} that is closer to the best value, which is one. In Equation 4.5, p_1 function is calculated. The function p_1 serves to impose a penalty to ensure that the natural frequencies remain within the specified limit values for the first objective function. Equation 4.5 activates the penalty function when the frequency ratios fall outside the range of 0.9 to 1.1. f_1 is the first objective function. The objective function of this optimization problem is tried to minimize. When the value is small, it means the natural frequencies calculated by the GFEM and the natural frequencies calculated by the BSM in the optimization process are close to each other. Objective function depends on functions a_1 and p_1. Also, c_1 constant affects the objective function. It is impossible to determine the c_1 constant in the objective function directly. It must be determined empirically based on the difficulty of satisfying the penalty function and the importance of the penalty function [46]. For this optimization code, c_1 is taken 100.

The second objective function compares the similarity of the mode shapes determined by the GFEM with the eigenvectors coming out of the BSM in the

optimization process. It uses MAC to compare the mode shapes. MAC formulation is given in Equation 4.7.

$$MAC(\{\phi_{BSM}\}\{\phi_{GFEM}\}) = \frac{|\{\phi_{BSM}\}^T\{\phi_{GFEM}\}|^2}{(\{\phi_{BSM}\}^T\{\phi_{BSM}\})(\{\phi_{GFEM}\}^T\{\phi_{GFEM}\})} \quad (4.7)$$

In Equation 4.7, ϕ_{BSM} represents the modal matrix of the BSM and ϕ_{GFEM} defines the modal matrix of the GFEM.

Equations 4.8 - 4.10 show the application of the penalty function considering only two MAC value. If more than two MAC values are to be considered, it should be added to the formula similarly. The penalty function is activated if the MAC function is less than 0.9. Note that, the second objective function is also tried to minimize.

$$a_2 = (|1 - MAC_1| + |1 - MAC_2|) \quad (4.8)$$

$$p_2 = minimum(0, MAC_1 - 0.9)^2 + minimum(0, MAC_2 - 0.9)^2 \quad (4.9)$$

$$f_2 = a_2 * (1 + c_2 * p_2) \quad (4.10)$$

The comments about the c_1 coefficient are also valid for the c_2 coefficient. The c_2 coefficient should be determined according to the importance of the penalty function. This optimization code uses a value of 500 for c_2.

4.5 Algorithm of the Code

This section explains the modified CSA code used to generate the BSM in detail. The code for optimization is generated using the MATLAB tool.

1. The inputs are prepared by determining the flock size, maximum number of iterations, flight length, and AP. Additionally, the number of iterations to decrease the AP is also given. All these parameters are given in Table 4.1. Input is required for the mass matrix, reference natural frequency,

eigenvectors used in calculating the objective function, coordinates of the BSM nodes, and nodes of the beam elements in the BSM.

Table 4.1 Parameters using in the optimization code

Parameters	*Value*
Flock size	50
Maximum number of iterations	1e+10
Flight length	2
Initial AP	0.6
Number of iterations to decrease the AP	200, 400, 600, 800, 1000 (For each iteration number, the AP is decreased by 0.1)

2. The initial values of the positions of the crows are given. The position matrix and the memory matrix are synchronized.
3. The objective function is calculated for the position of each crow. The operations performed while calculating the objective function are as follows.

   After receiving the updated design variables, the stiffness matrix for a single beam element is computed in the local coordinate system. The resulting stiffness matrix's size is 12x12, with 6 DOF corresponding to each node. The stiffness matrix must be converted into the global coordinate system. Equation 4.11 is employed to obtain the stiffness matrix for a single beam in the global coordinate system.

$$[\overline{K}_{global}] = [T^T][\overline{K}_{local}][T] \tag{4.11}$$

In Equation 4.11, T represents the transformation matrix. $\overline{K}_{global}$ shows the stiffness matrix written according to the global coordinate system for a beam element. $\overline{K}_{local}$ denotes the stiffness matrix written with respect to the local

coordinate system for a beam element. Appendix A gives the element stiffness matrix written with respect to the local element coordinate system.

Element stiffness matrices must be placed in their appropriate locations in the global stiffness matrix. Hence, the global stiffness matrix is obtained. Following the generation of the global stiffness matrix, the necessary boundary conditions are applied. With this step, the code has all the information to solve the eigenvalue problem defined in Equation 3.6.

The optimization code developed calculates eigenvalues and eigenvectors with the current design variables. Using the eigenvalues first objective function f_1 is calculated. MAC is calculated using the newly found eigenvectors and reference eigenvectors and using the MAC matrix second objective function f_2 is calculated. All these steps are performed by the Matlab code which essentially does the optimization iterations.

4. The number of iterations determines AP. As the number of iterations increases, the AP gradually decreases.
5. The crow's new position is determined using Equation 4.2 or 4.3.
6. The suitability of new positions is checked. If it is not suitable, it is returned to the old position.
7. Objective functions are calculated just as in Step 3 based on the new positions.
8. The Pareto optimal solution set from the objective functions are determined for the new position. In the optimization process, the goal is to minimize all the objective functions.
9. Following the determination of the Pareto optimal solution set, choosing from candidates which are not superior to each other is necessary. This selection aims to eliminate extreme cases from the Pareto optimal solution set. For instance, if the natural frequencies have met the target value, but the MAC values are too low, it is unlikely to reach the optimum solution. Cases where the two objective functions have common points must be included in

the memory matrix. In the selection process from the Pareto optimal solution set, candidates who meet any of the conditions listed below are accepted, and the memory matrix is updated accordingly.

- The memory matrix is updated if both objective functions are better or equal to the crow's current best value.
- If the penalty function p_2 is equal to zero at both the current position in the memory matrix and the new position, and if p_1 is greater than zero at the current position in the memory matrix, and the newly calculated f_1 is better than the existing f_1 in the memory matrix, then the memory matrix is updated. In this case, the mode shapes are acceptable. Since the MAC ratios of all mode shapes are higher than 0.9, p_2 is not activated. However, the situation is different for natural frequencies. The penalty function p_1 is still greater than zero. The expectation from the code is to focus on improving the frequency ratios rather than further improving MAC ratios.
- If the penalty function p_1 is equal to zero at both the current position in the memory matrix and the new position, and if p_2 is greater than zero at the current position in the memory matrix, and the newly calculated f_2 is better than the existing f_2 in the memory matrix, then the memory matrix is updated. This situation is the opposite of the previous situation. The code should improve the MAC ratios instead of the frequency ratios.
- If a penalty function (p(1) or p(2)) in the memory matrix is larger than twice the other penalty function, the priority in the objective functions is given to reducing the penalty function with the higher value. In this case, the memory matrix is updated if the penalty function with a higher value decreases and the penalty function with a lower value changes by less than 10 percent in the newly calculated objective functions. The memory matrix is updated even if the penalty function with a low value grows slightly. This prevents the first objective function from decreasing to low values and the second objective function from dwelling at high values.

10. In this step, it is checked whether the termination criterion has been met. If the change in objective functions in the last 200 iterations is less than two percent, termination criteria are provided. If reached, the code is stopped. If not reached, it is repeated from Step 4 until reaching the maximum number of iterations.

The design variables used in the optimization code are implemented to the beams in the BSM, and the generation of the BSM is completed.

To better understand the output of the optimization code, Table 4.2 gives the cross-sectional properties of the beam elements created for the horizontal tail. Cross-sectional properties of the remaining beam elements are given in Appendix B. There are six beam elements representing the horizontal tail in BSM. These six beam elements are given in Figure 4.5. In addition, the cross-sectional properties of the beam elements are given according to the element coordinate frames. The coordinate frame of element 1 is given in Figure 4.6 as an example. Coordinate frames of other horizontal tail beam elements are the same as element 1.

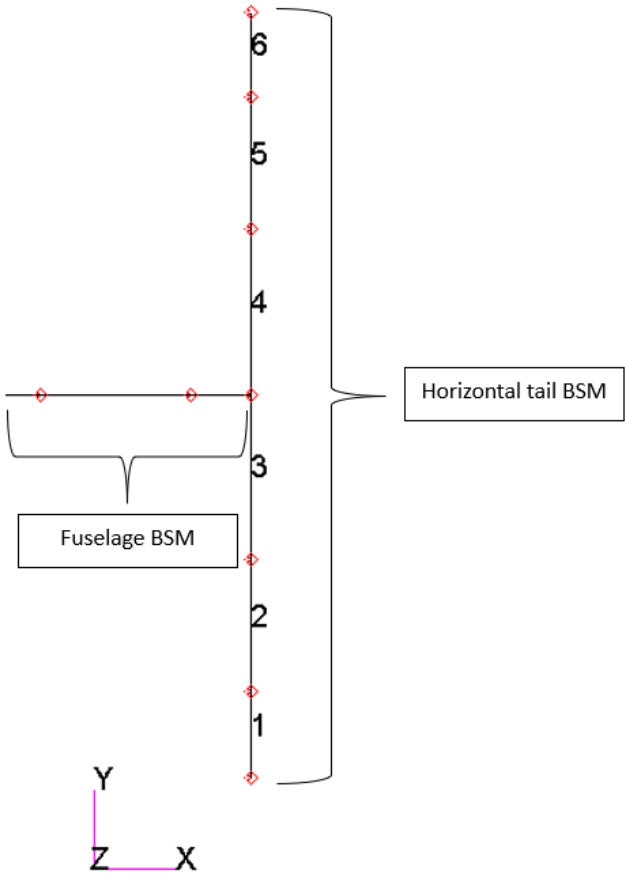

Figure 4.5 BSM of the horizontal tail

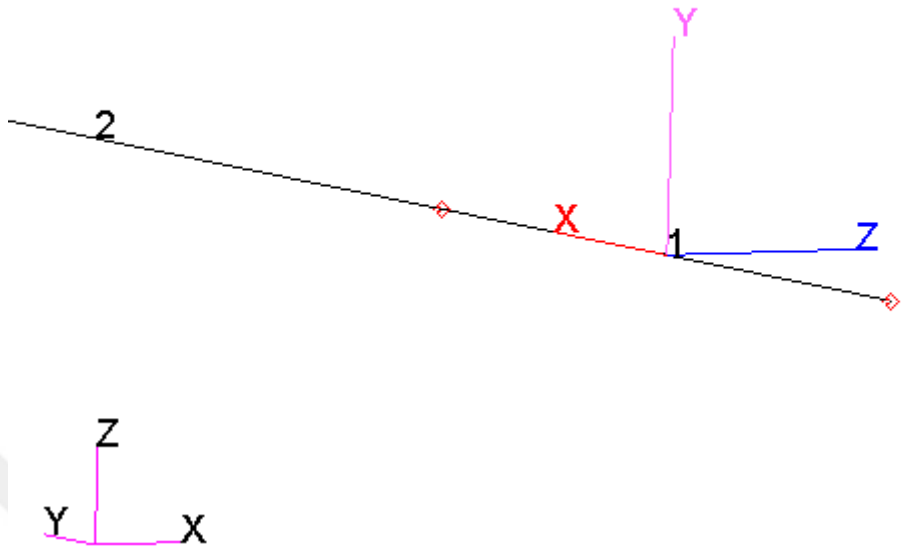

Figure 4.6 Element coordinate frame of element 1

Table 4.2 Output of the modified CSA for the horizontal tail

Number of the Beam Element	*Cross sectional area [mm²]*	I_{zz} [mm⁴]	I_{yy} [mm⁴]	J [mm⁴]
1	15.80	2.31	8110	46.90
2	12.70	5.26	3320	97.10
3	6.40	49.00	5320	31.40
4	6.40	49.00	5320	31.40
5	12.70	5.26	3320	97.10
6	15.80	2.31	8110	46.90
Elastic Modulus		3.98e+9 N/mm²		
Shear Modulus		1.28e+9 N/mm²		

Table 4.2 shows the properties of the beam elements representing the horizontal tail. Since the horizontal tail is symmetrical with respect to the X axis, beam elements

also show balanced properties. I_{yy} is higher than other inertia values because I_{yy} is the beam property that determines the stiffness in the in-plane direction. As explained in Section 3.4.1, in-plane motions are ignored in the dynamic analysis. In this case, the modified CSA code increased the I_{yy} value to increase the natural frequencies of the in-plane motions to high values. It should also be noted that cross-sectional areas seem to be inconsistent compared with the inertia properties. Since the PBAR element in Nastran is used when creating the BSM, the cross-sectional properties do not have to represent a real shape, they are just numbers. For this reason, it is possible to see inconsistency in the output of the optimization code. Secondly, looking at Table 3.4, it is seen that all the elastic modes correspond to bending, torsion, and rotation modes. I_{zz} is vital to match the natural frequencies and mode shapes of out-of-plane bending with the GFEM. Polar moment of inertia is more critical for torsional modes. Rotation modes generally depend on the value of the rotational spring used between the control surface and the lifting surface. Conversely, the cross-sectional area is ineffective in determining the frequency and mode shapes of bending, torsion, and rotational modes. It is common to see the inconsistency between area and inertia properties since the cross-sectional area has little effect, or almost none, on objective functions.

The time history of the objective functions during the optimization process of the horizontal tail beam properties is given in Figure 4.7. The data used to create Figure 4.7 is obtained from the memory matrix of crow 50.

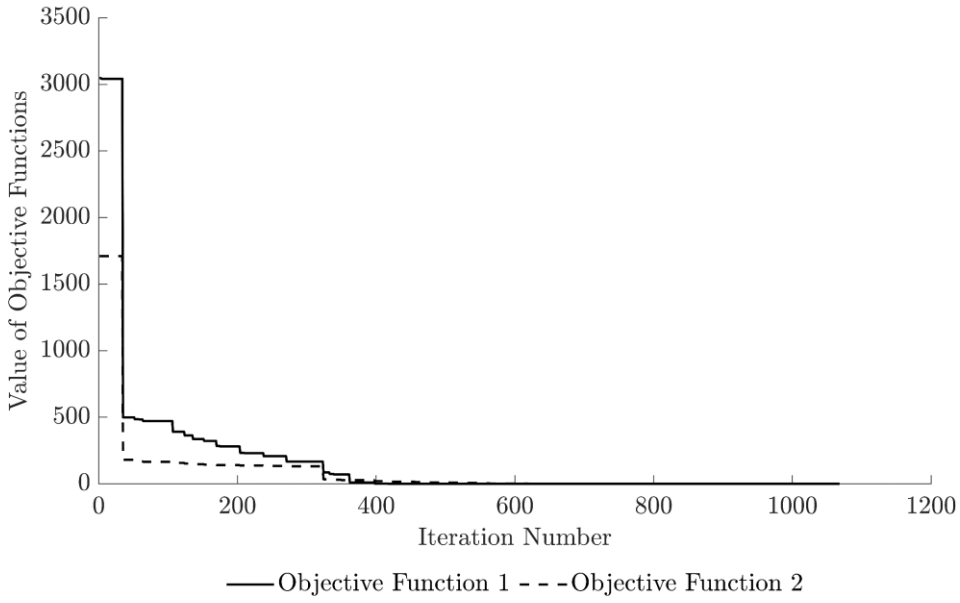

Figure 4.7 Iteration vs. objective functions

CHAPTER 5

GENERATION OF THE BEAM STICK MODEL OF THE VLA FOR DYNAMIC ANALYSIS

5.1 Introduction

This section explains the process of creating the stick model in detail. All the information about converting the wing, fuselage, horizontal, and vertical tail from the GFEM to the BSM is presented. In addition, the proposed methods for connecting the control surfaces to the lifting surfaces and lifting surfaces to the body are described in detail. By describing these complex aspects, this section provides a comprehensive understanding of BSM generation.

5.2 Generation of the Beam Stick Model of the Wing Structure

While creating the stick model of the aircraft, first of all, studies are carried out on the wing structure. The wing model consists of three parts: the flap, the aileron, and the wing torque box. In this study, it is aimed to obtain separate beam models for each of these parts. In this context, the wing torque box is modeled in isolation under the fixed boundary condition in the first step. Figure 5.1 shows the GFEM and BSM of the isolated wing torque box. In Figure 5.1, the elements in the spanwise direction of the BSM represent the beams, while the triangular elements symbolize the lumped masses. The lumped masses used in BSM are the same as those used in GFEM. The elements extending from the beams to the leading and trailing edges are the RBE2 elements. RBE2 elements are called rigid elements and are used in many dynamic analyses to improve fluid-structure interaction. The nodes on the leading edge and trailing edge in BSM are created by referencing the nodes on the upper skin of the

GFEM. The nodes on the x-axis of the BSM cross over the elastic axis, while the nodes on the y-axis cross over the ribs.

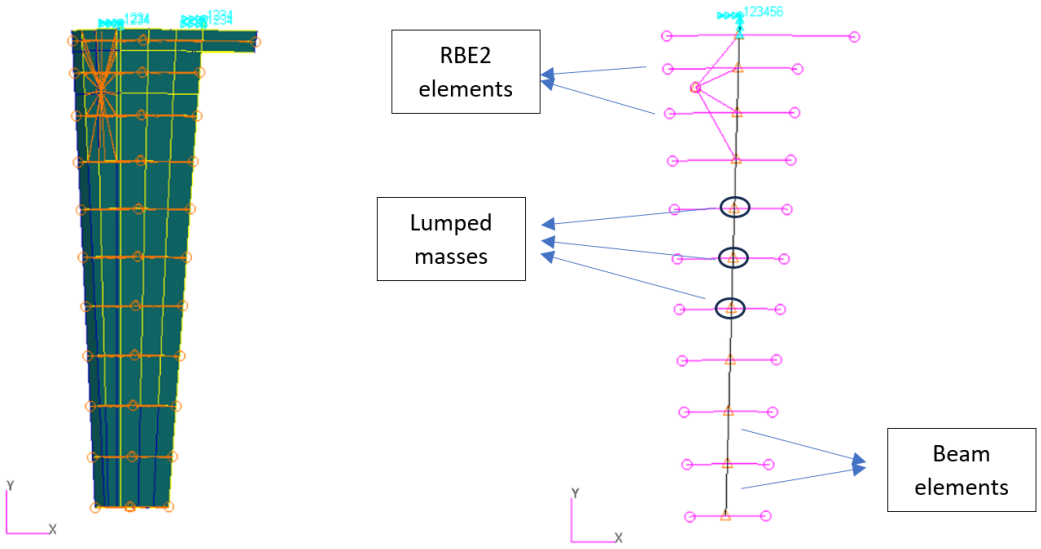

Figure 5.1 Isolated wing torque box model for the GFEM and the BSM

Torsional load is applied at the free end of the isolated torque box GFEM to determine the position of the elastic axis. The nodal line of the structure under load is accepted as the elastic axis. Figure 5.2 shows the static analysis result. The intersection line of the deformed and undeformed shapes indicates the position of the elastic axis. The intersection points of the elastic axis and ribs determine the location of BSM nodes.

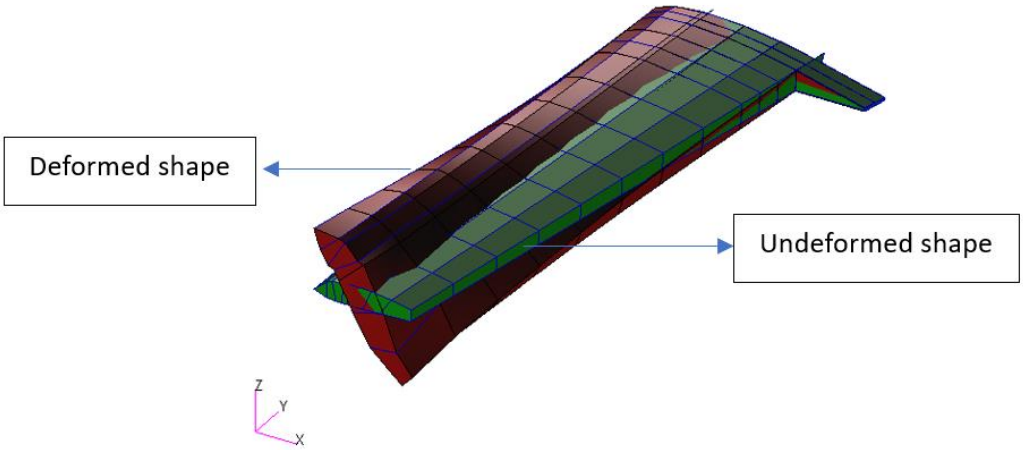

Figure 5.2 Deformed shape under torsion load (red) and undeformed shape under torsion load (green)

In the next step, the cross-sectional properties of the beam elements obtained from the optimization code are included in the stick model. A comparative analysis of dynamic properties performed for the isolated wing torque box model is presented in Table 5.1.

Table 5.1 Comparison of dynamic characteristic for the isolated wing torque box

Mode Identification	GFEM Frequency [Hz]	BSM Frequency [Hz]	Difference [%]	MAC
First bending	15.37	15.37	0.01	1.00
Second bending	59.38	58.21	1.97	0.99
First torsion	99.50	101.40	1.96	0.98

As evident from the data presented in Table 5.1, the dynamic characteristics of the wing torque box have been accurately represented in the BSM with high fidelity.

Modeling the control surfaces is the next step. Control surface modeling is carried out in two stages. The first step explains the conversion of the isolated control surface from GFEM to the BSM. The second step explains how the control surface is connected to the lifting surface in detail. The procedures performed to complete the first stage are listed below.

- In GFEM, the control surface is isolated. As an example, the isolated GFEM flap model and stick model are given in Figure 5.3. The points where the front spar, rib, and upper skin intersect are also the nodes where the beam nodes are located.
- Modal analysis is performed without applying any boundary conditions to the isolated control surface, hence for the free control surface.
- Natural frequencies and mode shapes from the modal analysis result are given as input to the optimization code. Beam properties from the code are used in the stick model. With this step, the representation of the dynamic characteristic of the isolated control surface with the BSM is completed.

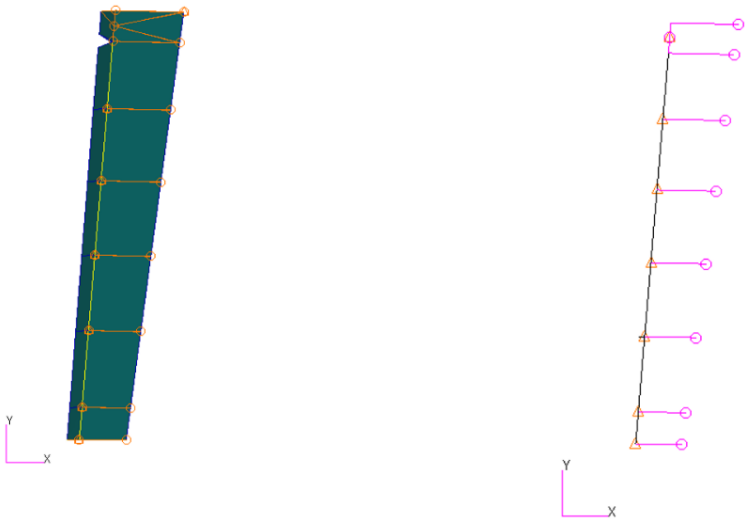

Figure 5.3 Isolated flap model for the GFEM and the BSM

Comparison of the dynamic characteristics for the isolated flap model is given in Table 5.2. Two elastic modes after the first six rigid body modes are given in Table 5.2.

Table 5.2 Comparison of dynamic characteristic of the isolated flap

Mode Identification	GFEM Frequency [Hz]	BSM Frequency [Hz]	Difference [%]	MAC
First bending	80.17	81.22	0.32	1.00
Second bending	185.05	183.66	0.75	1.00

Table 5.2 shows that the isolated flap is successfully converted to the stick model with very low difference compared to the GFEM. However, the way that the control surface is connected to the lifting surface is very important in order to reflect the dynamic characteristics of the aircraft accurately. There are thirteen control surface-lifting surface connections on the aircraft. Two connections are used for each aileron and flap, two for the rudder, and three for the elevator to the lifting surface. Connections are provided with lugs and clevises. Connection points are given in Figure 5.4 with circles.

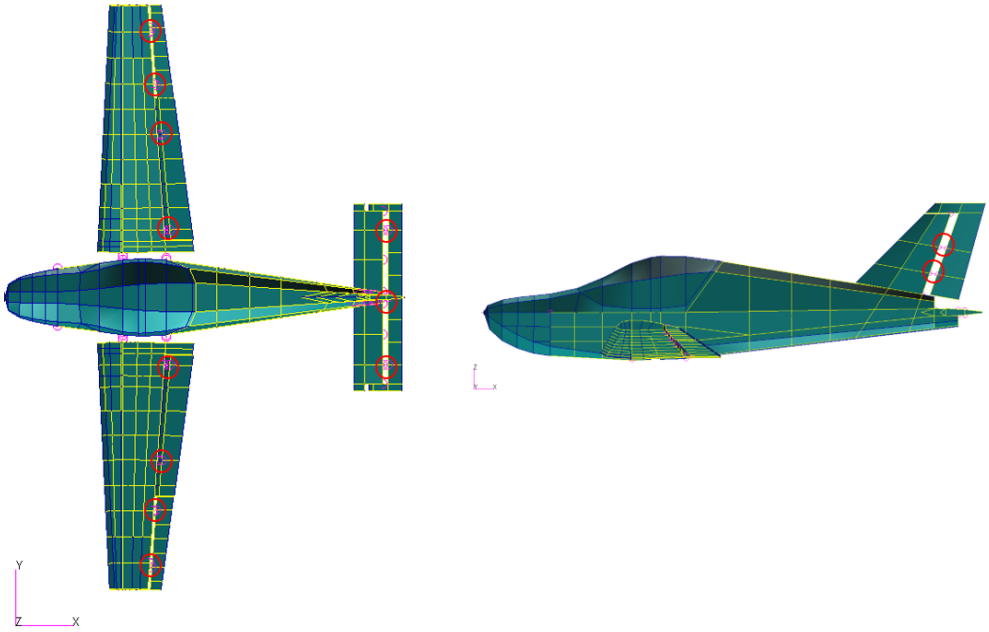

Figure 5.4 Connection points of the control surfaces of the VLA

The control surface and lifting surface connection between the GFEM and the BSM is shown in Figure 5.5 and Figure 5.6, respectively.

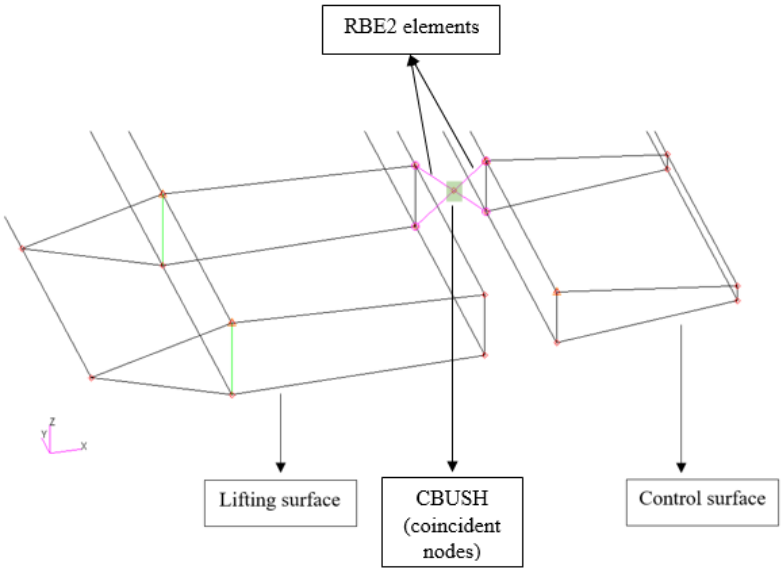

Figure 5.5 Connection of the control surface to lifting surface in the GFEM

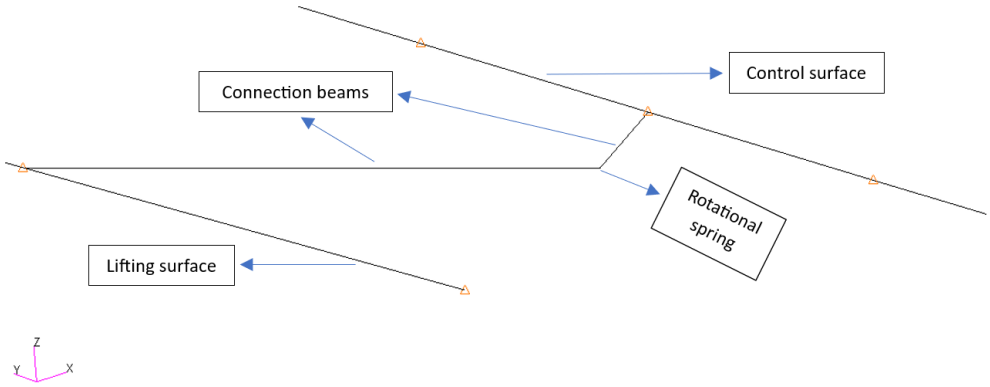

Figure 5.6 Connection of the control surface to the lifting surface in the BSM

In GFEM, two RBE2s connect on the hinge line. There are coincident nodes at the junction of RBE2s, and there is a rotational spring between the coincident nodes. This spring only resists the moments along the hinge line.

In BSM, a beam extends from the control surface to the hinge line, and another extends from the hinge line to the lifting surface. There are duplicated nodes on the hinge line, as in GFEM. A rotational spring with the same stiffness used in the GFEM is placed between these nodes.

At this stage, the cross-sectional properties of the isolated control surface and the isolated torque box are already determined. For the combined model, only the cross-sectional properties of the connection beams are obtained using the optimization code. It should be noted that other than the connection beams, the cross-sectional properties of the beams in the isolated torque box and the isolated control surface, are obtained in the previous stages and at this stage they are not used as design variables in the optimization for the determination of the stiffness of the connection beams. In Figure 5.7, connection beams are highlighted, and RBE2 and lumped mass elements are hidden to increase comprehensibleness. In Figure 5.8 the BSM of the combination of the isolated wing model with control surfaces that is created is presented. Aileron beam elements are not included in the optimization process because the isolated natural frequencies of the aileron are above 200 Hz. The values

for Aileron's EA, EI, and GJ have been set to 1e+12. This high value ensures that the internal stiffness of the aileron does not impact the elastic modes within the desired frequency range, similar to the GFEM. However, the connection elements between the aileron-wing torque box are included in the optimization. These elements affect the aileron rotation mode.

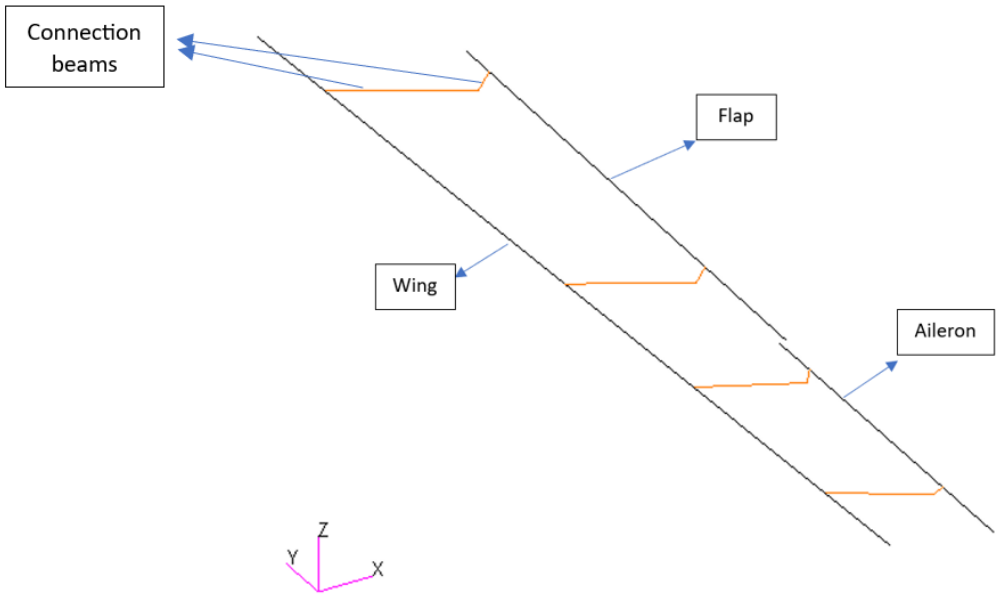

Figure 5.7 Connection beams of the wing

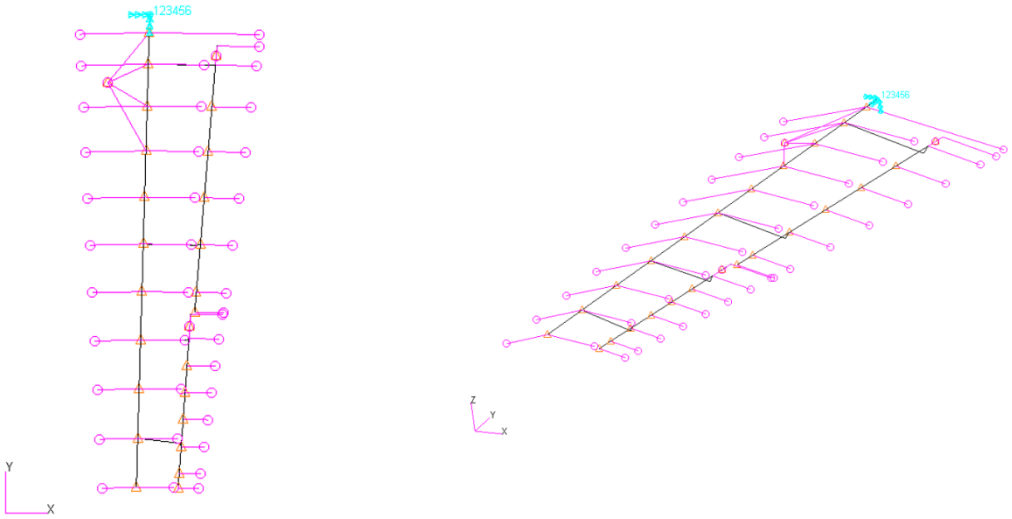

Figure 5.8 BSM of the combination of the isolated wing and the wing control surfaces

The natural frequencies and MAC values of the GFEM and the BSM for the combination of the isolated wing and the wing control surfaces after the connection beams are also optimized are given in Table 5.3.

Table 5.3 Comparison of dynamic characteristics of the isolated wing (combination of the wing torque box and control surfaces)

Mode Identification	GFEM Frequency [Hz]	BSM Frequency [Hz]	Difference [%]	MAC
1. Aileron rotation – wing first bending	13.40	13.43	0.23	1.00
2. Flap & aileron rotation (out of phase)	18.21	18.22	0.06	1.00
3. Flap & aileron rotation (in phase)	19.24	19.17	0.36	1.00
4. Wing second bending	56.68	55.29	2.45	1.00
5. Flap first bending	69.86	70.10	0.34	1.00
6. Wing first torsion-flap & aileron rotation (in phase)	90.64	93.38	3.02	0.96

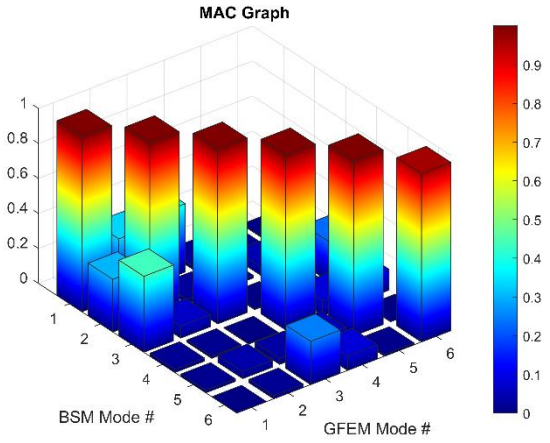

Figure 5.9 MAC graph for the combination of the isolated wing torque box and the wing control surfaces

Table 5.3 and Figure 5.9 show that the first six modes of the wing are obtained by the BSM with minimal difference from the GFEM.

5.3 Generation of the Beam Stick Model of the Fuselage Structure

The first step in this process is to obtain a GFEM for the isolated fuselage. The fuselage is disconnected from the wing attachment. Since horizontal and vertical tails are directly riveted to fuselage frames, to create an isolated fuselage model, the tail part is separated from the fuselage from the rivet connections. The isolated fuselage model created is given in Figure 5.10.

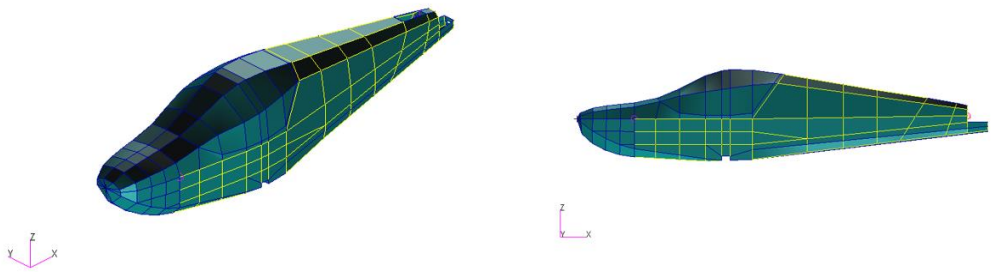

Figure 5.10 GFEM of the isolated fuselage

Natural frequencies and eigenvectors of the isolated fuselage model should be given as input to the optimization code. For this reason, modal analysis is performed for the isolated fuselage model. The fuselage is modeled in free-free boundary conditions. The two elastic modes after the first six rigid modes of the aircraft are given as input to the optimization code. Since the natural frequencies of the third and subsequent elastic modes are above 200 Hz, it has little effect on dynamic analysis. For this reason, these modes are ignored when creating the BSM of the fuselage. The fuselage stick model created is given in Figure 5.11. Since it is a free-free boundary condition, fuselage does not have an elastic axis. A curve is drawn from the nose to the rear of the aircraft, and the intersection points of the curve and the frames form the nodes of the fuselage beams. The RBE2 elements in the fuselage are extended from the beam node to the points on the far right and left along the spanwise direction of the fuselage. RBE2 elements are used to improve the aero-structure interaction.

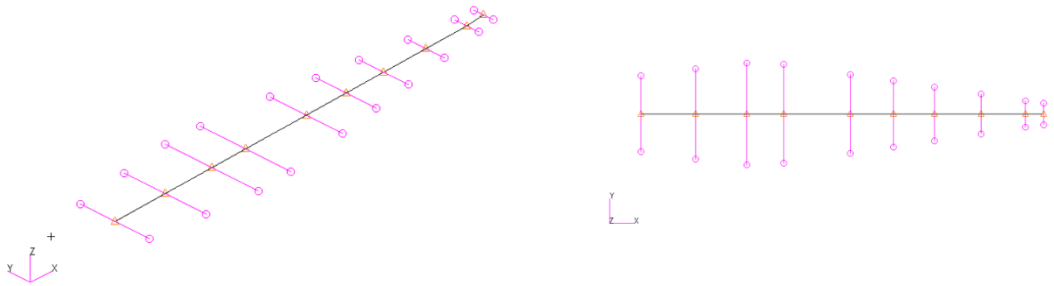

Figure 5.11 BSM of the isolated fuselage

The natural frequencies obtained after applying the optimized beam properties to the stick model are given in Table 5.4.

Table 5.4 Comparison of dynamic characteristics of the isolated fuselage

Mode Identification	GFEM Frequency [Hz]	BSM Frequency [Hz]	Difference [%]	MAC
First bending (out of plane)	119.34	119.29	0.04	1.00
First bending (in plane)	153.92	153.98	0.04	1.00

Table 5.4 shows that BSM of the fuselage very accurately represents the GFEM. Following the generation of the BSM of the isolated fuselage, the wing and the fuselage connection is performed. Five beams are used for each wing-fuselage (left and right wing) connection. These beams are numbered in Figure 5.12.

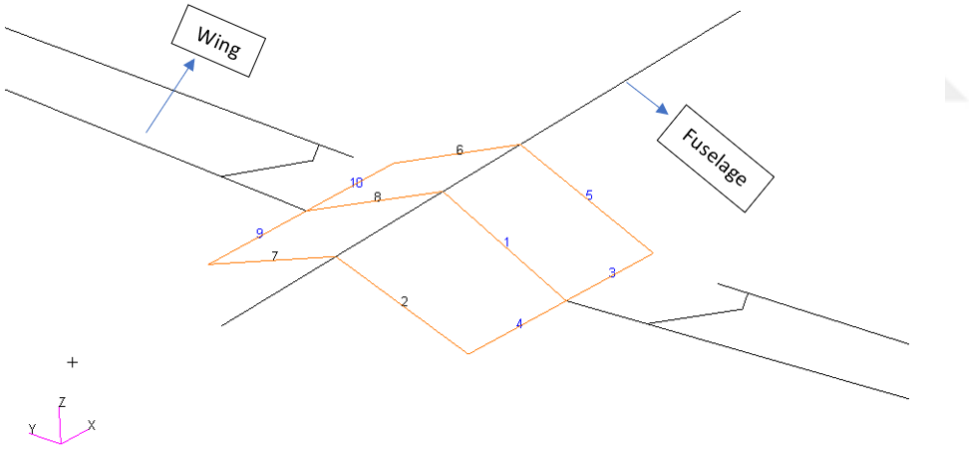

Figure 5.12 Wing-fuselage connection

The cross-sectional properties of the connection beams in the fuselage-wing connection should be optimized. For this purpose, first the necessary inputs for the optimization code are taken from the modal analysis result of the isolated wing-fuselage GFEM. GFEM and BSM of the isolated wing-fuselage are given in Figure

5.13. The highlighted regions in Figure 5.13 are the beams placed to model the wing-fuselage connection in the BSM. At this stage, stiffness properties of the isolated wing beam elements, including the control surfaces, and the fuselage beam elements have already been determined. While modeling the wing-fuselage connection, only the cross-sectional properties of the connection beams on the port side are given to the optimization code as design variables. Since the aircraft is symmetrical, cross-sectional properties of the connection beams on the starboard are the same as on the port side. It should be noted that the RBE2 elements on the BSM are hidden in order not to complicate Figure 5.13.

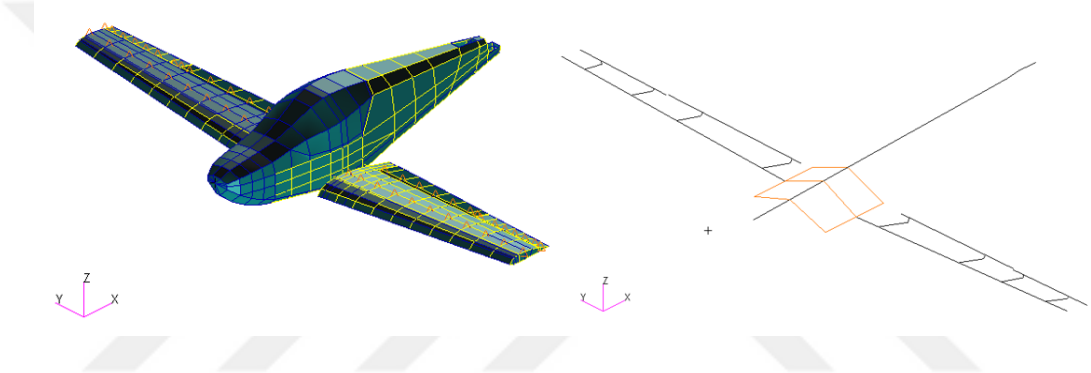

Figure 5.13 GFEM and BSM of the isolated wing-fuselage

The comparison of the natural frequencies and MAC values after optimizing the wing-body connection is given in Table 5.5. In Table 5.5, S denotes the symmetric mode shape, and A means the antisymmetric mode shape.

Table 5.5 Comparison of dynamic characteristics of the isolated wing-fuselage combination

Mode Identification	GFEM Frequency [Hz]	BSM Frequency [Hz]	Difference [%]	MAC
1. Aileron rotation – wing first bending (S)	12.38	12.33	0.40	1.00
2. Aileron rotation (A)	17.05	17.10	0.29	1.00
3. Flap & aileron rotation (out of phase) (S)	18.03	18.06	0.17	1.00
4. Flap rotation (A)	18.86	18.82	0.21	1.00
5. Flap & aileron rotation (in phase) (S)	19.10	19.02	0.42	1.00
6. Wing first bending – aileron rotation (A)	25.25	25.40	0.59	0.98
7. Wing second bending (S)	52.35	50.80	2.96	0.99
8. Wing second bending (A)	62.52	61.29	1.97	0.99
9. Flap first bending (S)	69.66	69.89	0.33	1.00
10. Flap first bending (A)	70.49	70.66	0.24	1.00
11. Wing first torsion flap & aileron rotation (in phase) (S)	85.12	84.86	0.31	0.95

When the natural frequencies and MAC values are examined, it is observed that the targeted similarity rates have been achieved. The MAC graph for the isolated wing-fuselage combination is presented in Figure 5.14.

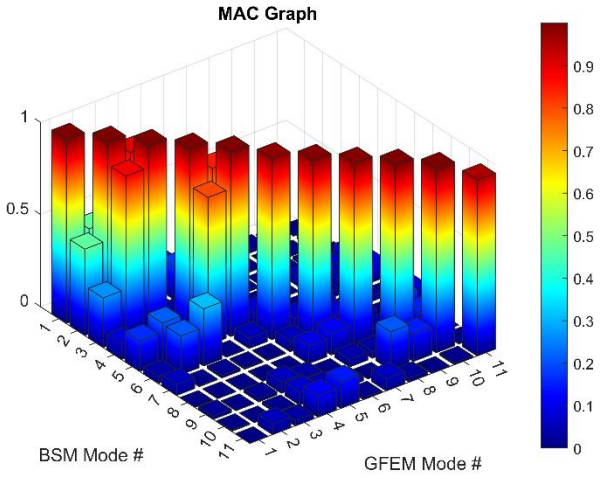

Figure 5.14 MAC graph for the isolated wing-fuselage

Having optimized the cross-sectional properties of the beams in the wing-fuselage connection, the conversion of the combination of the isolated wing and fuselage to BSM is completed.

5.4 Generation of the Beam Stick Model of the Vertical Tail and the Rudder

In this section, conversion of the vertical tail and rudder to BSM is explained. For this, isolated GFEM of the vertical tail and the fuselage are needed. Modal analysis of this model generates the inputs of the optimization code. The rudder and connection of the rudder to the vertical tail are included in the model in the next stage, just like the wing. GFEM and BSM of the isolated vertical tail and fuselage combination are given in Figure 5.15.

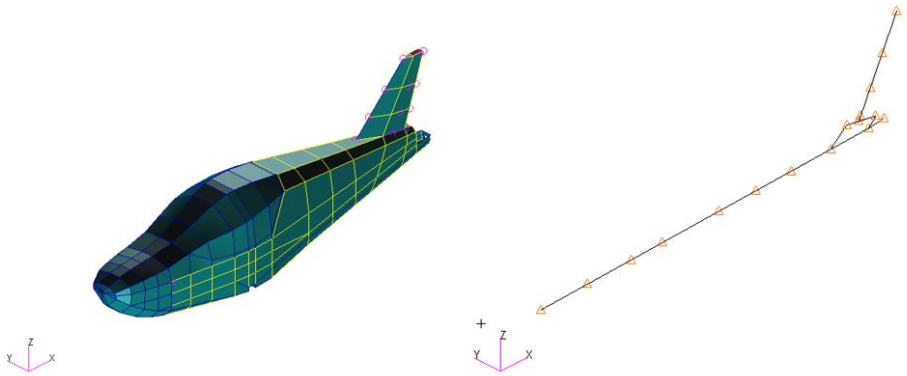

Figure 5.15 GFEM and BSM of the isolated fuselage-vertical tail assembly

Different from the wing-fuselage connection, in this case in the optimization code, the cross-sectional properties of the beam elements in the vertical tail and in the vertical tail-fuselage connection are taken as design variables simultaneously. The main difference between the wing-fuselage connection and the vertical tail-fuselage connection is that the vertical-fuselage connection is directly riveted to the fuselage frames. However, the wing-fuselage connection is made using lug and clevis joints. Therefore, the vertical tail is modeled as part of the fuselage to optimize beam values rather than using a cantilever boundary condition like the wing. The beam properties of the fuselage are the values determined in the previous step. Only the vertical tail and vertical tail-fuselage connection beam properties shown in Figure 5.16 are optimized in this step. Comparison of the dynamic characteristics of the isolated fuselage and vertical tail combination obtained by the GFEM and the BSM is given in Table 5.6.

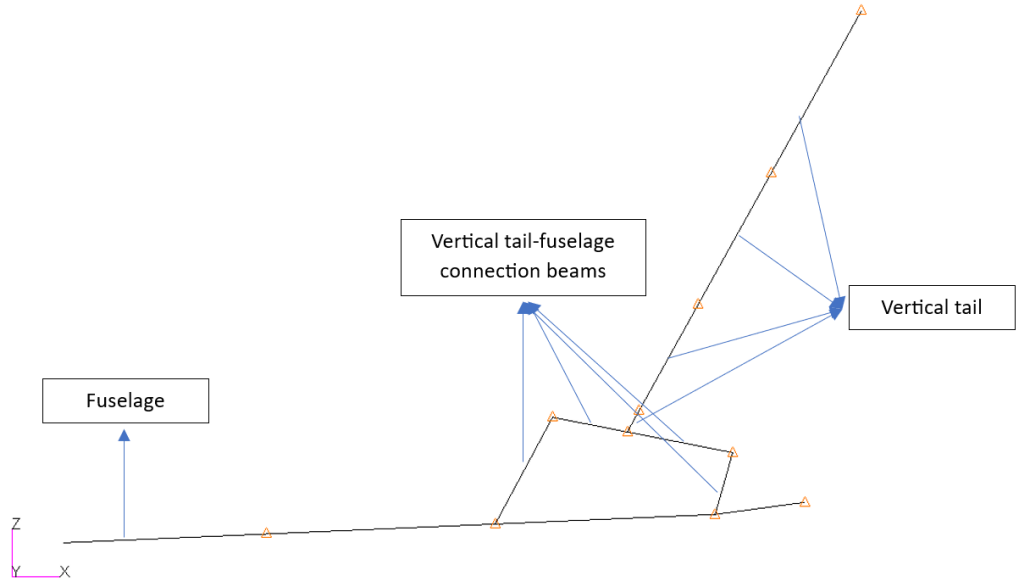

Figure 5.16 BSM of the vertical tail plane

Table 5.6 Comparison of dynamic characteristics of the isolated fuselage-vertical tail combination

Mode Identification	GFEM Frequency [Hz]	BSM Frequency [Hz]	Difference [%]	MAC
Vertical tail first bending	56.94	57.32	0.74	0.97
Fuselage first bending (out of plane)	113.09	109.92	2.78	0.96
Vertical tail first torsion	123.90	121.58	2.12	0.96

In the second step, an isolated rudder model is created. Free isolated rudder models are given in Figure 5.17. The methodology used when modeling the wing's control surfaces is applied similarly.

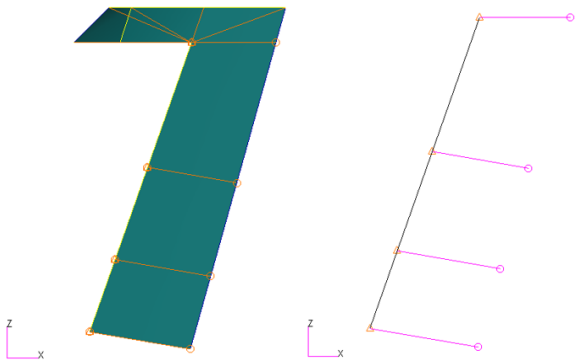

Figure 5.17 GFEM and BSM of the isolated rudder

A comparison of the dynamic characteristics of isolated rudder models is given in Table 5.7. For the rudder, only one elastic mode is included in the optimization code. It should be noted that the natural frequencies of the remaining elastic modes are above 200 Hz.

Table 5.7 Comparison of dynamic characteristics of the isolated rudder

Mode Identification	GFEM Frequency [Hz]	BSM Frequency [Hz]	Difference [%]	MAC
Rudder first bending	141.45	142.86	0.99	0.97

The next step is to find the cross-sectional properties of the connection beams connecting the rudder to the vertical tail. Dynamic characteristics of the GFEM of the isolated fuselage-vertical tail-rudder are used as input in the optimization. Only connection beams are given as design variables to the optimization code. Connection beams are shown in Figure 5.18. All remaining beam properties of the fuselage and the vertical tail are taken from previous analyses. The modeling logic of the vertical tail-rudder connection in BSM is the same as shown in Figure 5.6.

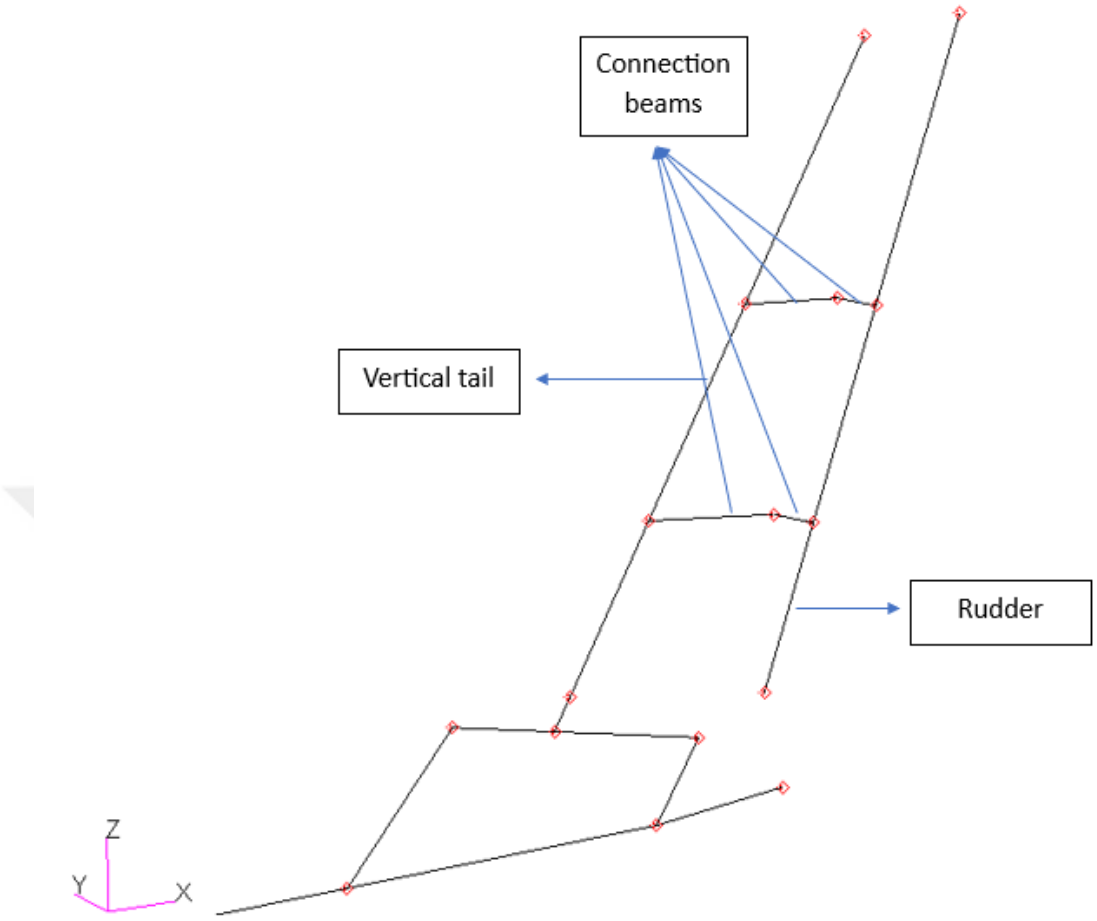

Figure 5.18 Connection beams of the vertical tail and the rudder

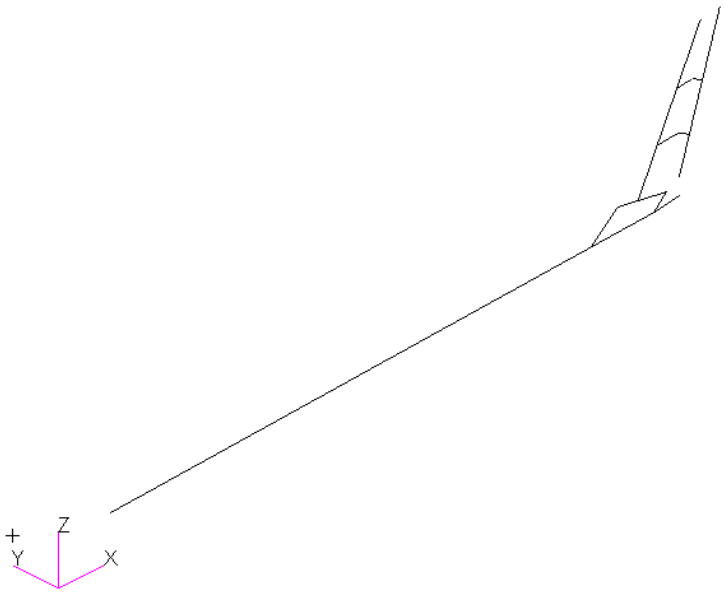

Figure 5.19 BSM of the isolated fuselage-vertical tail-rudder assembly

When the cross-sectional properties of the optimized connection beams are used, the modal analysis results of the BSM are given in Table 5.8.

Table 5.8 Comparison of dynamic characteristics of the isolated fuselage-vertical tail-rudder

Mode Identification	GFEM Frequency [Hz]	BSM Frequency [Hz]	Difference [%]	MAC
Vertical tail first bending	31.17	31.68	1.63	0.97
Rudder rotation	33.10	32.68	1.26	1.00
Vertical tail first torsion-rudder first bending	82.59	82.45	0.17	0.96
Fuselage first bending (out of plane)	100.33	98.12	2.20	0.96

Table 5.8 shows that the BSM of the isolated fuselage-vertical tail-rudder represents the dynamic characteristics of the GFEM of the isolated fuselage-vertical tail-rudder very closely.

5.5 Generation of the Beam Stick Model of the Horizontal Tail and Elevator

This section explains how the horizontal tail and the elevator assembly are converted to BSM. The process used is the same as the one used in converting the vertical tail and rudder to BSM. In this context, an isolated fuselage-horizontal tail model is needed first. Similar to the approach employed in other models, the isolated GFEM representation of the fuselage-horizontal tail assembly is used in the determination of the cross-sectional parameters of the beam elements in the horizontal tail section within the BSM. The horizontal tail is directly riveted to the fuselage frame, just like the vertical tail. Therefore, the optimization process of the horizontal tail is similar

to the vertical tail. GFEM and BSM of the isolated fuselage-horizontal tail are given in Figure 5.20.

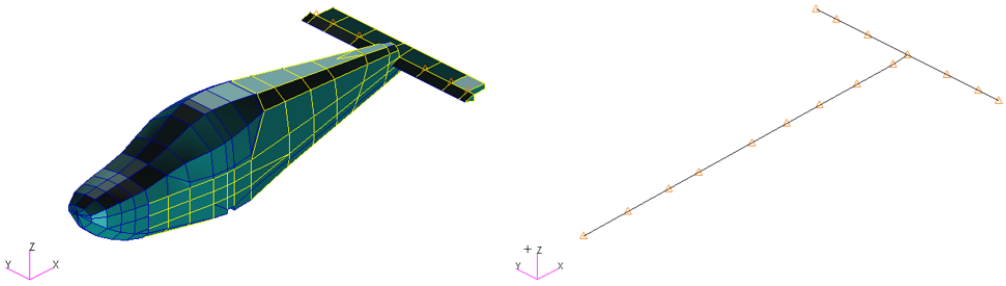

Figure 5.20 GFEM and BSM of the isolated fuselage – horizontal tail assembly

In the optimization code, only the beam elements of the horizontal tail are assigned as design variables. For the fuselage, beam properties determined in Section 5.3 are used directly. The comparison of the dynamic characteristics of the two models is given in Table 5.9.

Table 5.9 Comparison of dynamic characteristic of the isolated fuselage-horizontal tail

Mode Identification	GFEM Frequency [Hz]	BSM Frequency [Hz]	Difference [%]	MAC
Horizontal tail first bending (A)	61.86	62.20	0.54	0.99
Horizontal tail first bending (S)	64.03	64.86	1.30	1.00
Fuselage first bending (out of phase) – horizontal tail torsion (S)	115.90	112.62	2.83	0.97
Horizontal tail torsion (A)	135.17	136.26	0.81	0.94
Horizontal tail torsion (S)	139.15	140.56	1.01	0.94

In the next step, the cross-sectional properties of the beams representing the elevator must be determined. For this, an isolated free elevator model is used as in other control surfaces. GFEM and BSM of the free isolated elevator are given in Figure 5.21.

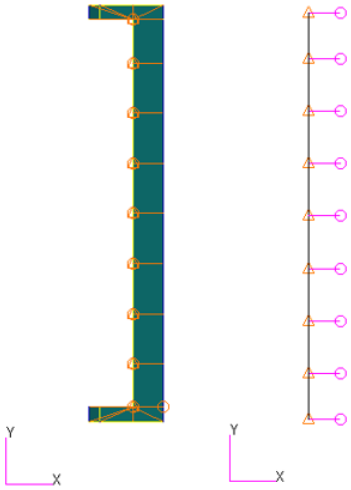

Figure 5.21 GFEM and BSM of the isolated elevator

Dynamic characteristics of the GFEM and BSM of the isolated elevator are compared in Table 5.10.

Table 5.10 Comparison of the dynamic characteristics of the isolated elevator

Mode Identification	GFEM Frequency [Hz]	BSM Frequency [Hz]	Difference [%]	MAC
Elevator first bending	30.29	30.19	0.33	1.00
Elevator first torsion	52.74	52.75	0.02	1.00
Elevator second bending	83.59	83.60	0.01	1.00

The final step to complete the BSM of the isolated fuselage-horizontal tail-elevator assembly is the modeling of the elevator-horizontal tail connection beams. An isolated fuselage-horizontal tail-elevator model is needed for modeling the connection beams. The modeling logic of the horizontal tail-elevator connection is

the same as in Figure 5.6. Unlike other control surfaces, the elevator has three lug-clevis connections. For this reason, connection beams are used in three different regions. Connection beams are shown in Figure 5.22.

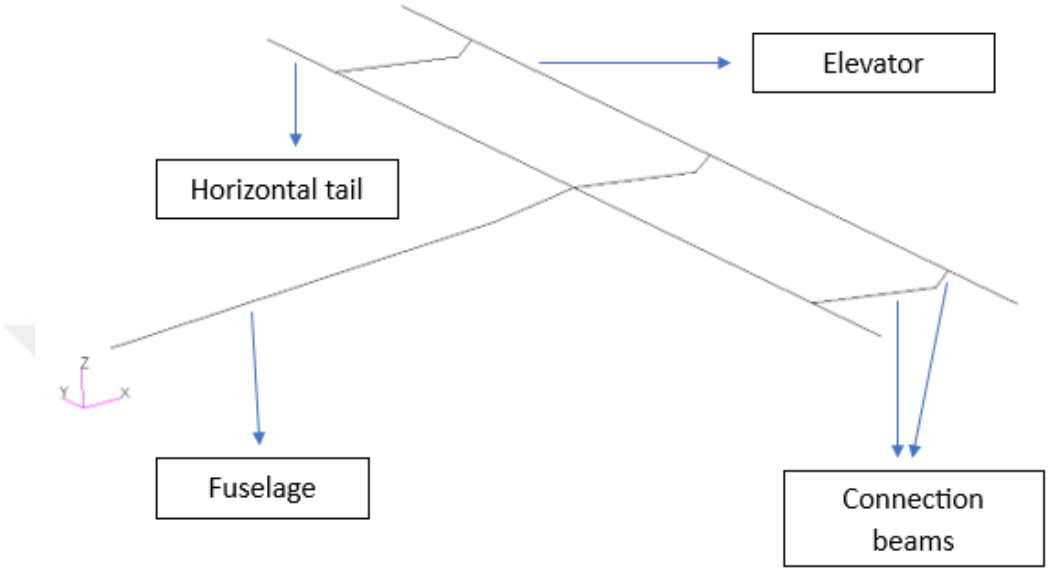

Figure 5.22 Connection beams of the horizontal tail – elevator

Isolated GFEM and BSM of the isolated fuselage - horizontal tail - elevator assembly are given in Figure 5.23. In Figure 5.23, RBE2 elements are hidden to increase visibility. A comparison of the dynamic characteristics of the two models is given in Table 5.11.

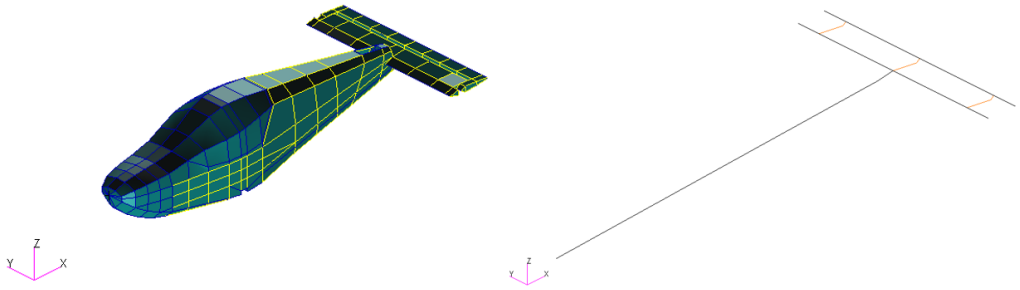

Figure 5.23 GFEM and BSM of the isolated fuselage - horizontal tail - elevator assembly

Table 5.11 Comparison of dynamic characteristics of the isolated fuselage-horizontal-elevator assembly

Mode Identification	GFEM Frequency [Hz]	BSM Frequency [Hz]	Error [%]	MAC
Elevator rotation (S)	21.65	21.64	0.05	1.00
Horizontal tail first bending-elevator first bending (A)	27.68	27.47	0.74	1.00
Horizontal tail first bending-elevator first bending (S)	34.28	33.28	2.91	1.00
Elevator first torsion-horizontal tail first bending (A)	54.62	54.63	0.02	0.99
Horizontal tail first torsion-elevator second bending (A)	76.84	77.08	0.31	0.98
Horizontal tail first torsion (S)	83.90	83.92	0.02	0.92

At this stage, for all isolated models BSM, which reflects the dynamic characteristics of GFEM, is created with high accuracy. In the final step isolated models are assembled to generate the BSM of the complete VLA.

5.6 Assembly of the Isolated Beam Stick Models

In this section, the generated BSMs are assembled, and the natural frequencies and mode shapes of the entire aircraft calculated by the GFEM and by the BSM are compared. BSM of the assembled VLA is given in Figure 5.24. In Sections 5.2-5.5, conversion of components to BSM is explained. To assemble the BSM, wing BSM explained in Section 5.2, fuselage and wing-fuselage connection BSM explained in Section 5.3, BSMs of the vertical tail, rudder, and connection beams explained in Section 5.4, and the BSM of the horizontal tail, elevator, and connection beams explained in Section 5.5 are used.

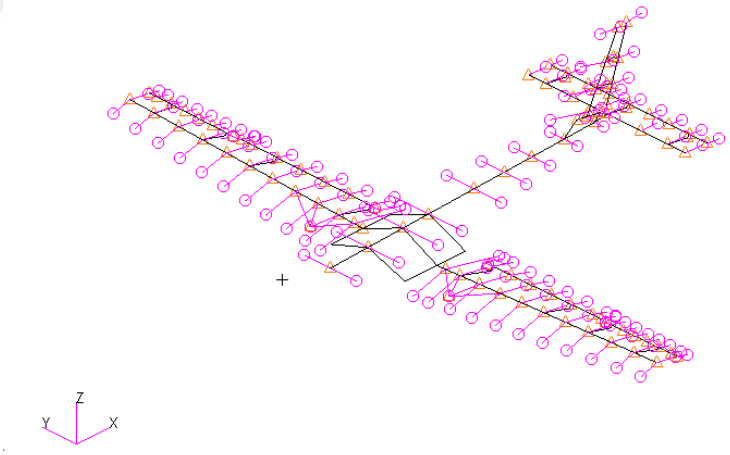

Figure 5.24 BSM of the METU-VLA

A modal analysis is performed on the created BSM. The final comparison of the dynamic characteristics of the GFEM and BSM is given in Table 5.12.

Table 5.12 Comparison of dynamic characteristics of the GFEM and BSM of the VLA

Mode Identification	GFEM Frequency [Hz]	BSM Frequency [Hz]	Difference [%]	MAC
1. Wing first bending – aileron rotation (S)	12.35	12.30	0.36	1.00
2. Aileron rotation (A)	16.97	17.02	0.28	1.00
3. Aileron & flap rotation (out of phase) (S)	18.02	18.05	0.17	1.00
4. Flap rotation (A)	18.85	18.81	0.21	1.00
5. Aileron & flap rotation (in phase) (S)	19.09	19.00	0.46	1.00
6. Elevator rotation (S)	21.66	21.94	1.31	0.99
7. Wing first bending – aileron rotation (A)	23.12	23.04	0.32	1.00
8. Horizontal tail first bending-vertical tail first bending-elevator first bending (A)	27.35	27.36	0.02	0.99
9. Vertical tail first bending (A)	30.65	31.16	1.68	0.95
10. Rudder rotation (A)	32.70	32.44	0.78	0.99
11. Horizontal tail first bending – elevator first bending (S)	33.60	32.59	3.01	0.95
12. Wing second bending (S)	52.36	50.73	3.10	0.99
13. Elevator first torsion – horizontal tail first bending (S)	53.26	54.29	1.95	0.98
14. Wing second bending (A)	62.56	61.44	1.79	0.99
15. Flap first bending (S)	69.65	69.88	0.32	1.00
16. Flap first bending (A)	70.40	70.64	0.34	1.00
17. Horizontal tail first torsion – elevator second bending (A)	76.81	77.69	1.15	0.97

Table 5.12 continued

18. Vertical tail first torsion - rudder first bending (A)	82.55	81.16	1.69	0.88
19. Horizontal tail first torsion (S)	83.67	84.05	0.44	0.89
20. Wing first torsion (S)	85.42	84.74	0.80	0.95

As it is seen in Table 5.12, BSM has successfully reflected the first 20 elastic modes of the GFEM. The natural frequency of the last mode to be used in BSM is determined as 85.42 Hz. It is observed that the natural frequency of elastic modes above this frequency has almost no effect on dynamic aeroelastic analyses. Therefore, ignoring natural frequencies above 85 Hz from the study does not affect the results of the dynamic aeroelasticity analysis.

When a comparison is made between GFEM and BSM, it is seen that the most significant difference between natural frequencies is 3.10%. The highest difference among natural frequencies is slightly above 3%. The lowest MAC ratio is calculated as 0.88. Although this value is below the targeted threshold of 0.90, when the results are examined, it is seen that the BSM successfully reflects 18 of the 20 elastic modes found in GFEM with a MAC ratio above 0.95.

Also, a high similarity rate is observed in the modes dominated by the control surfaces, indicating that the proposed method used in modeling the control surfaces is effective. Another striking point is that the connection mechanisms between different components are also successfully reflected by the BSM. The MAC plot is presented in Figure 5.25 to compare the mode shapes of GFEM and BSM.

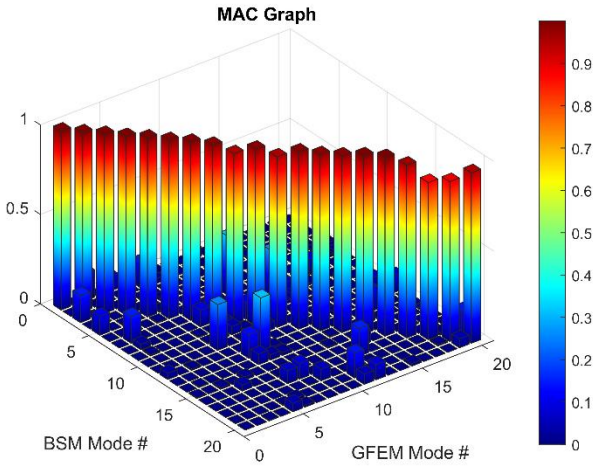

Figure 5.25 MAC graph for the entire aircraft

The diagonal terms are dominant in the MAC chart in Figure 5.25. This indicates that mode shapes of the GFEM and the BSM are highly similar. Finally, the mode shapes of the first three elastic modes of the aircraft are given in Figure 5.26. Remaining mode shapes are also given in Appendix C.

When comparing the computational times for modal analysis, GFEM took 2.27 seconds, while BSM took only 0.93 seconds.

a

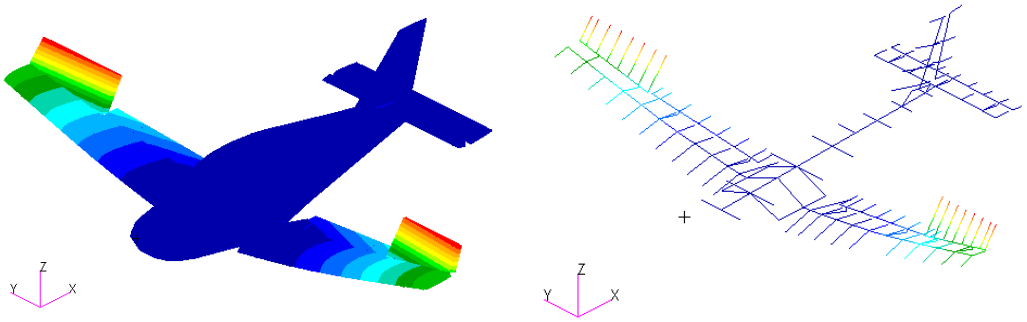

b

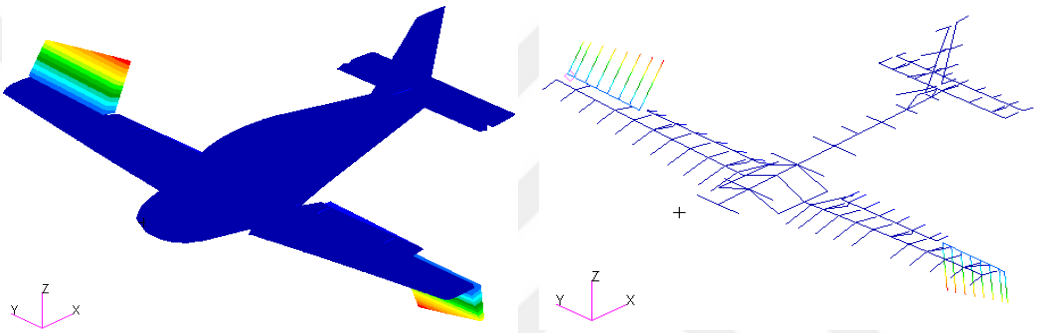

c

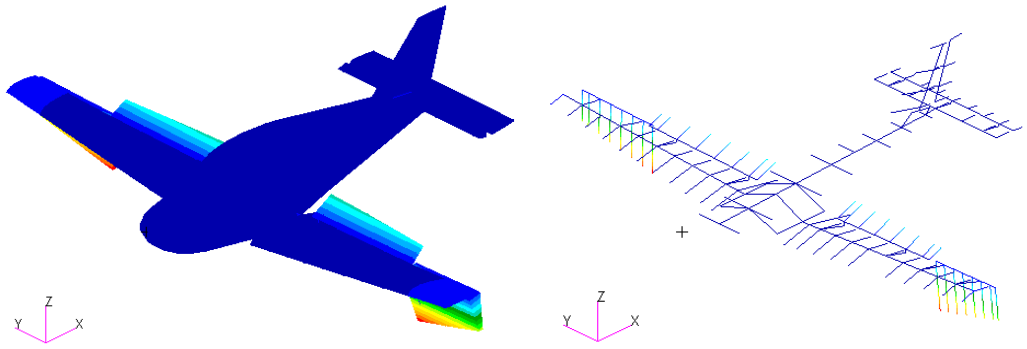

Figure 5.26 Comparison of first three elastic mode shapes a) Wing first bending – aileron rotation (S) b) Aileron rotation (A) c) Aileron & flap rotation (out of phase) (S)

CHAPTER 6

DYNAMIC AEROELASTIC ANALYSIS OF THE VERY LIGHT AIRCRAFT

6.1 Introduction

This section aims to test the usability of the generated BSM for dynamic analysis. The chapter starts with the aerodynamic model and splining methodology of the BSM. Flutter and discrete gust analysis are performed using the aeroelastic models created for GFEM and BSM and results are compared. In this respect, MSC Nastran SOL145 is used for flutter analysis, and MSC Nastran SOL146 is used for discrete gust analysis.

It should be noted that BSMs should quickly adapt to minor changes in the aircraft, hence the effect of structural modifications on the dynamic characteristics of the aircraft can easily be evaluated. For instance, flutter analyses should be performed at the full aircraft level and for all possible combinations of fuel and payload configurations. This creates a considerable analysis load on the aircraft design process. Therefore, this section also evaluates how the BSM responds to mass changes. The usability and reliability of the BSM are evaluated by comparing the results obtained by the 3D GFEM.

6.2 Aerodynamic Model Used in Conjunction with the Beam Stick Model

The aerodynamic model used for the BSM is the same as for the GFEM. The aerodynamic model used and the theory behind it were explained in Section 3.5.

6.3 Aero-Beam Stick Model Coupling

In the aeroelastic model of the VLA whose structure is represented by the BSM, IPS is used to provide communication between the aerodynamic model and the BSM. In order to use IPS in conjunction with the BSM, a surface must be created. For this reason, RBE2 elements from beams to the trailing edge and leading edge have also been added to splined nodes. In addition, another advantage of these RBE2 elements is that they allow the aerodynamic model to remain within the structural model. In cases where the aerodynamic model is larger than the structural model, extrapolation has to be made. Extrapolations in the IPS method may cause severe errors since there is no boundary condition in the theory. Added RBE2 elements are shown in purple in Figure 6.1.

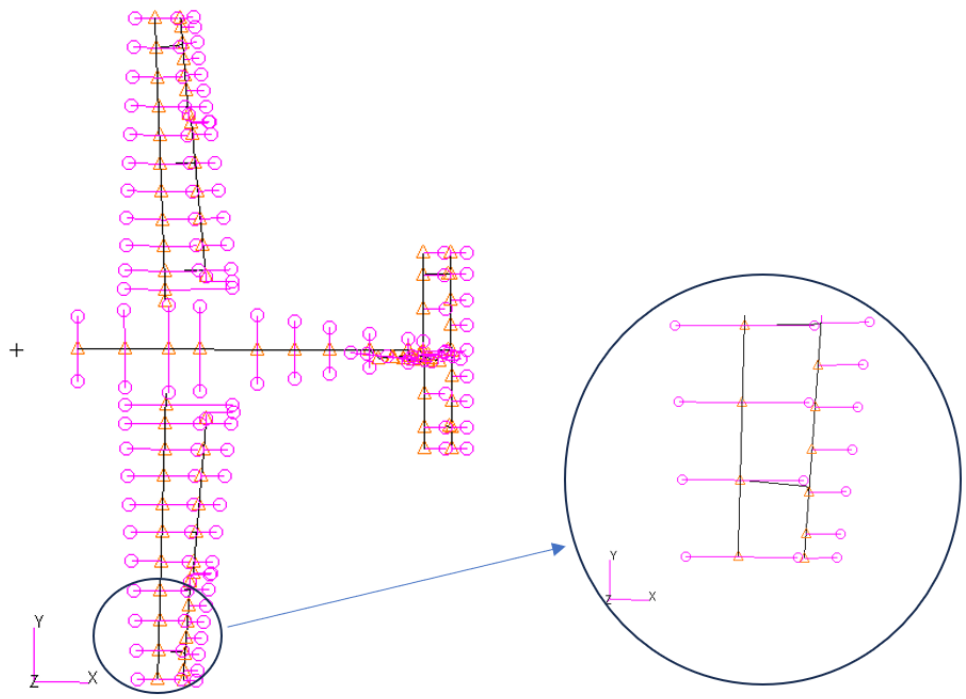

Figure 6.1 RBE2 elements in the BSM

Splined nodes used in BSM are given in Figure 6.2 and Figure 6.3.

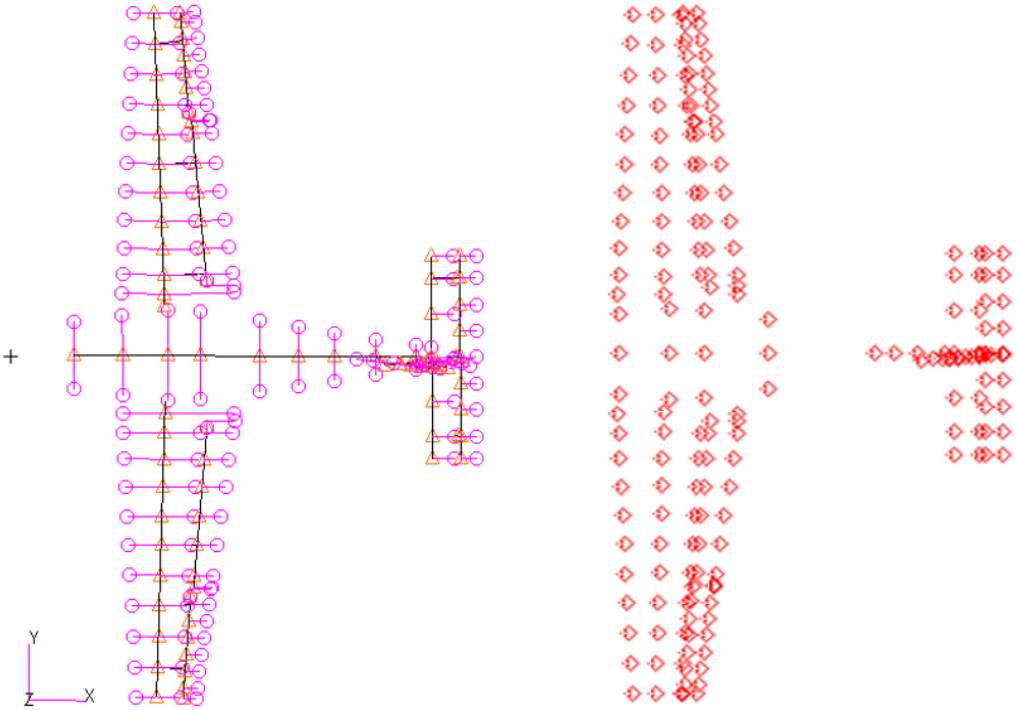

Figure 6.2 Splined nodes from the top-view (left – BSM, right – splined nodes)

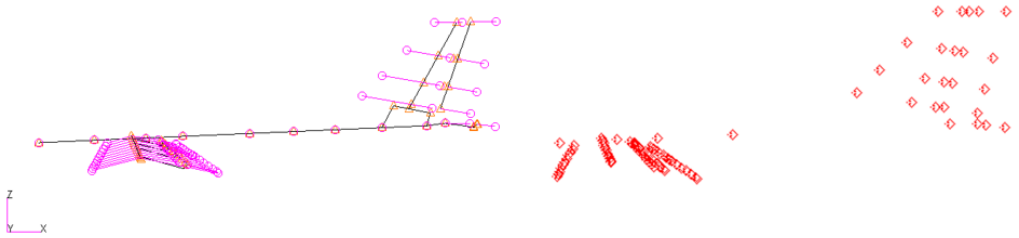

Figure 6.3 Splined nodes from the side-view (left – BSM, right – splined nodes)

Spline verification can be performed by comparing the deformation of the structural model with the deformation of the aerodynamic model. For this reason, certain elastic mode responses of the aerodynamic model and BSM are compared in Figure 6.4.

a) Mode 1

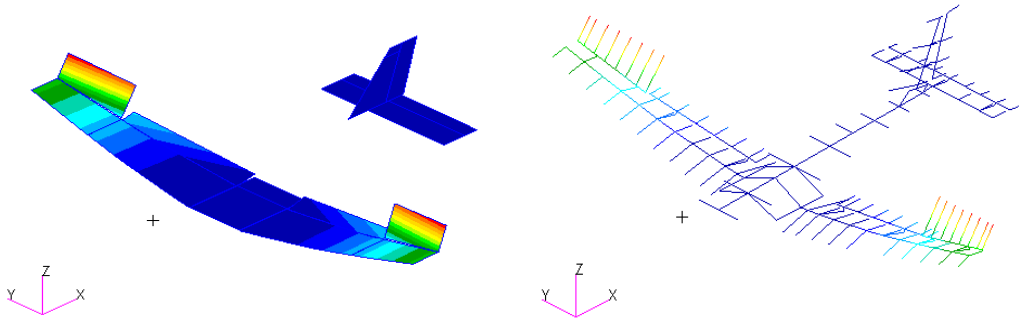

b) Mode 7

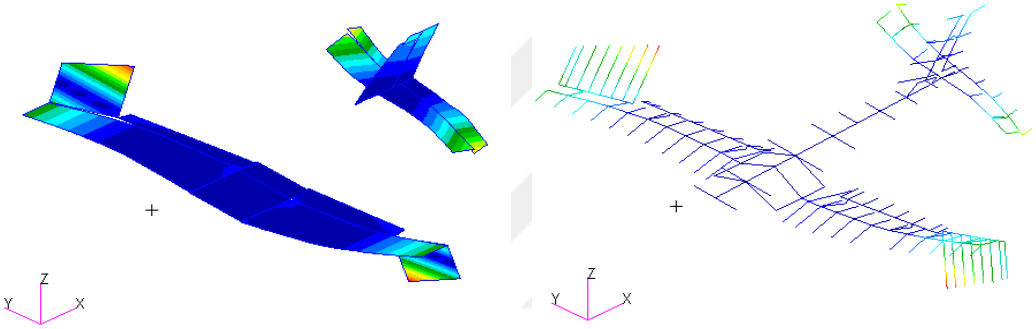

c) Mode10

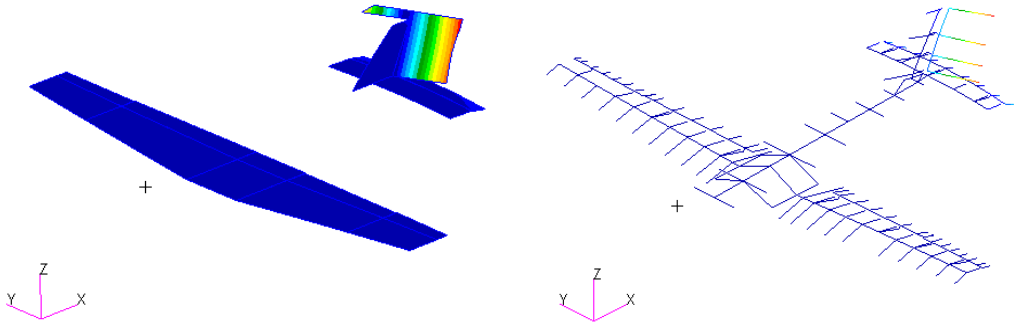

d) Mode 14

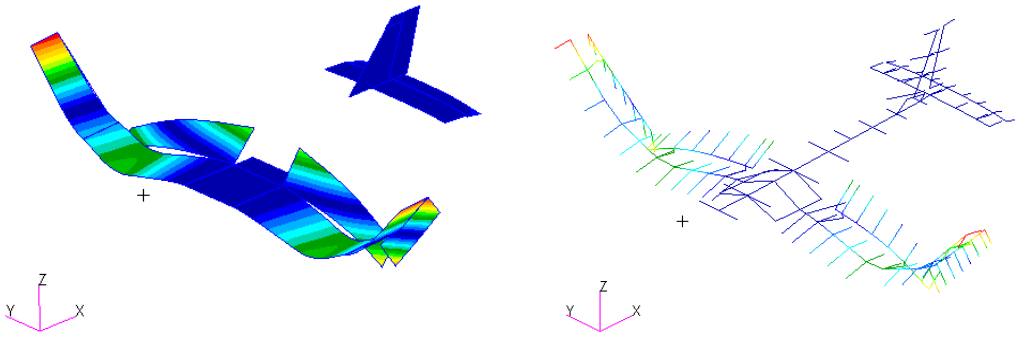

Figure 6.4 Spline Verification of the BSM (left aerodynamic model, right BSM)

To ensure that all components are splined correctly, the elastic modes presented in Figure 6.4 have been carefully selected to include the movement of all components. As Figure 6.4 shows, motions of the aerodynamic model and the structural model are similar. This shows that the chosen spline nodes are adequately and correctly selected.

6.4 Flutter Analysis of the Very Light Aircraft

Flutter is the phenomenon in which vibrations increase uncontrollably during the interaction of the aircraft structure with unsteady aerodynamic loads. Flutter can cause loss of aircraft. For this reason, flutter analyses should be done meticulously and included in the optimization process of the aircraft.

First, this section explains the PK solution methodology [47] used in flutter analysis. Subsequently, the flutter speed, frequencies, and mode shapes of GFEM and BSM are compared.

6.4.1 PK Solution Method

The most general form of an equation of motion for a discrete system is given in Equation 3.1. The assumption of an undamped system is made to simplify the derivation. However, damping can be easily added to the system. The equation of motion of an undamped system is given in Equation 6.1.

$$[M]\{\ddot{q}\ (t)\} + [K]\{q(t)\} = \{Q(t)\} \tag{6.1}$$

In Equation 6.1, M and K matrices are mass and stiffness matrices, respectively. q is the degree of freedom vector representing the structural deformation, and Q is the force column vector. The Q vector can be split into two as in Equation 6.2.

$$\{Q(t)\} = F_a(q) + F_e(t) \tag{6.2}$$

where $F_e(t)$ represent the external forces and $F_a(q)$ represents the unsteady aerodynamic loads generated due to the deformation of the structure. Continuous turbulence, discrete gusts, or control surface aerodynamic forces as a result of the pilot input command are examples of the external forces applied. Equation 6.3 can be obtained by combining Equation 6.2 and 6.1.

$$[M]\{\ddot{q}\ (t)\} + [K]\{q(t)\} - F_a(q) = F_e(t) \tag{6.3}$$

In dynamic aeroelastic analysis employing DLM, usually the aerodynamic influence coefficient (AIC) matrix is calculated to obtain the unsteady load vector $F_a(q)$. A matrix whose coefficients describe the aerodynamic influence of aerodynamic boxes on the control points is produced by assembling the simple integral solutions. The 75% chordwise station and box center are the control points for each box in DLM. Control point is the point where the boundary condition is satisfied. The relationship between the created AIC matrix and the deformation and force on the aerodynamic panels is given in Equation 6.4 [48].

$$\{F_h\} = q_\infty[AIC(Mach, k)]h \tag{6.4}$$

In Equation 6.4, q_∞ is the dynamic pressure, F_h is the force on aerodynamic model, and h is the deformation of the aerodynamic boxes. AIC matrix depends on reduced frequency (k) and Mach number. Reduced frequency depends on reference chord ($\bar{c}$), angular frequency ($\bar{\omega}$), and free-stream velocity (V).

$$k = \frac{\bar{\omega}\bar{c}}{2V} \tag{6.5}$$

Aerodynamic forces on the structural model can be obtained when Equation 3.7 and 3.10 are combined.

$$\{F_a\} = q_\infty [G]^T [AIC(Mach, k)][G]\{q\} \tag{6.6}$$

In the structural model, flutter solutions take much time, as there are many degrees of freedom. For this reason, the solution time can be shortened by including only the lower-order modes of the aircraft in the equation by using the modal approach. In order to use the modal approach, coordinate transformation given by Equation 6.7 must be done.

$$\{q\} = [\phi]\{\eta\} \tag{6.7}$$

where η stands for the generalized coordinate vector. The lower-order natural modes are contained in the columns of the modal matrix (ϕ). When Equation 6.7 and 6.6 are substituted into Equation 6.3 and the resulting equation is pre-multiplied with $[\phi]^T$, Equation 6.8 is obtained.

$$[M_{hh}]\{\ddot{\eta}\} + [K_{hh}]\{\eta\} - q_\infty [Q_{hh}(Mach, k)]\{\eta\} = [\phi^T]F_e(t) \tag{6.8}$$

where M_{hh}, K_{hh}, and Q_{hh} are generalized mass, stiffness, and aerodynamic force matrices, respectively. Equations 6.9, 6.10, and 6.11 define the generalized mass, stiffness, and aerodynamic force matrices, respectively.

$$[M_{hh}] = [\Phi]^T [M][\Phi] \tag{6.9}$$

$$[K_{hh}] = [\Phi]^T [K][\Phi] \tag{6.10}$$

$$[Q_{hh}(Mach, k)] = [\Phi]^T [G]^T [AIC(Mach, k)][G][\Phi] \tag{6.11}$$

The generalized aerodynamic force matrix is separated into real and imaginary parts in the PK solution methodology. Separating the generalized aerodynamic force gives Equation 6.12. Also, flutter is a self-excited event in nature, hence, $F_e(t) = 0$.

$$[M_{hh}]\{\ddot{\eta}\} + [K_{hh}]\{\eta\} - q_\infty Re([Q_{hh}(Mach, k)])\{\eta\} \\ -iq_\infty Im([Q_{hh}(Mach, k)])\{\eta\} = 0 \tag{6.12}$$

At this point, the solution of the system is assumed to be $\{\eta\} = \{\bar{\eta}\}e^{pt}$ with the p given in Equation 6.13 being the eigenvalue in the assumption.

$$p = \bar{\omega}(\gamma \pm i) \tag{6.13}$$

In Equation 6.13, γ is the decay parameter and ω is the frequency.

In the PK method, the computation of a damped oscillation yields the eigenvalue. It is important to emphasize that the underlying assumption of simple harmonic motion (SHM) during the calculation of unsteady aerodynamic loads causes inconsistency in the PK method. However, the PK approach can produce excellent results in situations with low damping characteristics and it is used widely in industry.

It should be noted that in an aeroelastic system, lightly damped modes are the ones that one cares about the most. High damping regions are not critical for an aeroelastic system. Considering that the decay parameter is much lower than $\bar{\omega}$, Equations 6.14 and 6.15 can be written.

$$\frac{p}{i\bar{\omega}} = \frac{\bar{\omega}\gamma + i\bar{\omega}}{i\bar{\omega}} \tag{6.14}$$

$$\frac{p}{i\bar{\omega}} \approx 1 \tag{6.15}$$

Equation 6.16 can then be written using Equation 6.15.

$$i\frac{p}{i\bar{\omega}} q_\infty Im([Q(Mach, k)])\{\bar{\eta}\}e^{pt} \approx iq_\infty Im([Q(Mach, k)])\{\bar{\eta}\}e^{pt} \tag{6.16}$$

Using Equation 6.16 and making necessary simplifications, governing equation 6.12 can be written in the form given by Equation 6.17.

$$[[M_{hh}]p^2 - (\frac{1}{4}\rho\bar{c}VIm(Q_{hh})/k)p + ([K_{hh}] - \frac{1}{2}\rho V^2 Re(Q_{hh}))]\{\bar{\eta}\} = 0 \quad (6.17)$$

Equation 6.17 is the fundamental equation of the PK method. This equation is a complex eigenvalue problem. It is usually expressed in state-space form. State matrix (A) is given in Equation 6.18.

$$A = \begin{bmatrix} 0 & I \\ -M_{hh}^{-1}[K_{hh} - \frac{1}{2}\rho V^2 V^2 Re(Q_{hh})] & M_{hh}^{-1}[\frac{1}{4}\rho\bar{c}VIm(Q_{hh})/k] \end{bmatrix} \quad (6.18)$$

Equation 6.19 is the flutter determinant.

$$det|[A - p[I]| \quad (6.19)$$

After solving Equation 6.19, four eigenvalues are obtained. These eigenvalues can be real or complex conjugate pairs. Real roots imply convergent or divergent behavior. Eigenvalues indicate convergence if they are negative real numbers and divergence if they are positive real numbers. The decay rate coefficient is used to express the damping for the real roots case. This relationship is given in Equation 6.20 [40].

$$g = 2\gamma \quad (6.20)$$

Circular frequency and reduced frequency are related. Equation 6.21 [40] provides this dependency.

$$\mathrm{k} = \frac{\bar{c}}{2V}\mathrm{Im}(p) \quad (6.21)$$

In Equation 6.21 k, $\bar{c}$, and V are the reduced frequency, reference chord, and free-stream velocity, respectively. The solution of the system must satisfy both Equation 6.17 and Equation 6.21. The two specified equations are directly satisfied if the eigenvalues are real because this only happens when k equals to zero. However, if eigenvalues are complex, an iterative solution is required. In the case of complex roots, almost all the eigenvalues are complex conjugate pairs. The steps to solve the PK method can be summarized as follows:

- Set the range of flight speeds.
- Perform the following actions for each flight speed within the specified range.
    - Specify the reduced frequency.
    - Determine the aerodynamic force associated with the reduced frequency and the Mach number.
    - Solve the complex eigenvalue problem to obtain the frequency and damping values.
    - Calculate a new reduced frequency using the obtained frequency and the stated flight speed as a starting point.
    - Check the convergence.
        - Adjust the reduced frequency and repeat the process if convergence is not obtained.
        - If the reduced frequency converges, store the frequency and damping values.
- Repeat all the process for new flight speed.

6.4.2 Flutter Analysis Results of the Very Light Aircraft using the 3D Global Finite Element Model and the Beam Stick Model

This section compares the results of flutter analysis of BSM and GFEM. The parameters in which the flutter analysis is performed are given in Table 6.1. Flutter analyses are performed using Nastran, Sol 145.

Table 6.1 Parameters of flutter analysis

Mach Number	0.4
Air Density	0.49 kg/m^3
Reference Chord	1.223 m
Solution Method	PK
Velocity Range	25 m/s – 290 m/s

In this study, matched point flutter analysis is not performed. The responses of the two models are examined by assuming the air conditions as 0.4 Mach for all dynamic pressures. If point matching analysis had been conducted, fewer flutter points would have been identified, and more data would have been analyzed to compare the two models. The GFEM has four flutter mechanisms. All these flutter mechanisms are also determined as a result of flutter analysis with the BSM. A comparison of the results of the two models is given in Table 6.2.

Table 6.2 Comparison of flutter analysis results

	GFEM		BSM	
	Flutter Speed [m/s]	Flutter Frequency [Hz]	Flutter Speed [m/s]	Flutter Frequency [Hz]
Flutter Mechanism 1	75.54	22.50	77.50	22.43
Flutter Mechanism 2	155.83	26.75	148.82	26.74
Flutter Mechanism 3	284.42	30.21	275.06	30.96
Flutter Mechanism 4	223.79	50.87	228.40	49.22

In Table 6.2, the first flutter mechanism is the coupling mechanism of the aileron rotation and the wing first bending. The modes that contribute the most to the second flutter mechanism are horizontal tail bending, vertical tail bending, and aileron rotation. The primary contributors to the third flutter mechanism are vertical tail bending and rudder rotation modes. The fourth flutter mechanism includes by wing second bending, aileron, and flap rotation.

Table 6.2 shows that the responses of the two models are similar. When examining the flutter speed, the highest difference is 4.5%. Regarding flutter frequencies, the highest difference is 3.3%. These results show that the models give very close and consistent responses with each other.

VG and VF graphs are of great importance in flutter analysis. The VG graph shows how the aeroelastic damping changes with airspeed. The VF graph shows the effect of air velocity on the aeroelastic frequency. These graphs are used to understand the energy loss of the structural system and the damping of vibrations. Identifying possible flutter regions, detecting critical velocity ranges, and optimizing the structural design are also important. This information is essential to ensure the safety and durability of the aircraft. For this reason, comparison of VG and VF graphs of BSM and GFEM gives information in terms of the reliability of the BSM. VG and VF graphs of both models are shown in Figure 6.5 and Figure 6.6, respectively. Figure 6.5 and Figure 6.6 are prepared for only the flutter modes listed in Table 6.2.

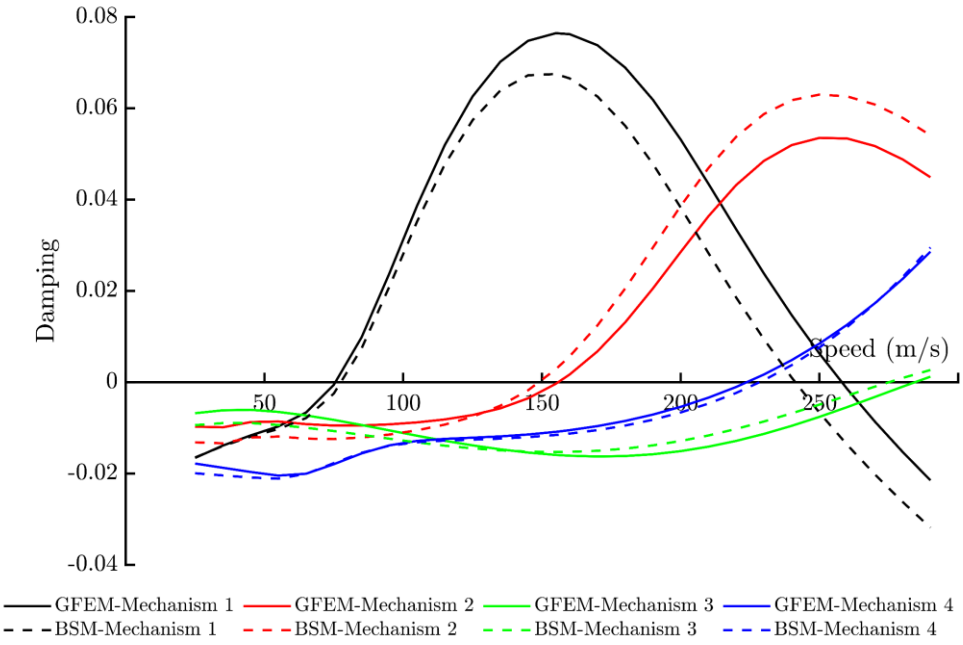

Figure 6.5 Comparison of VG graphs

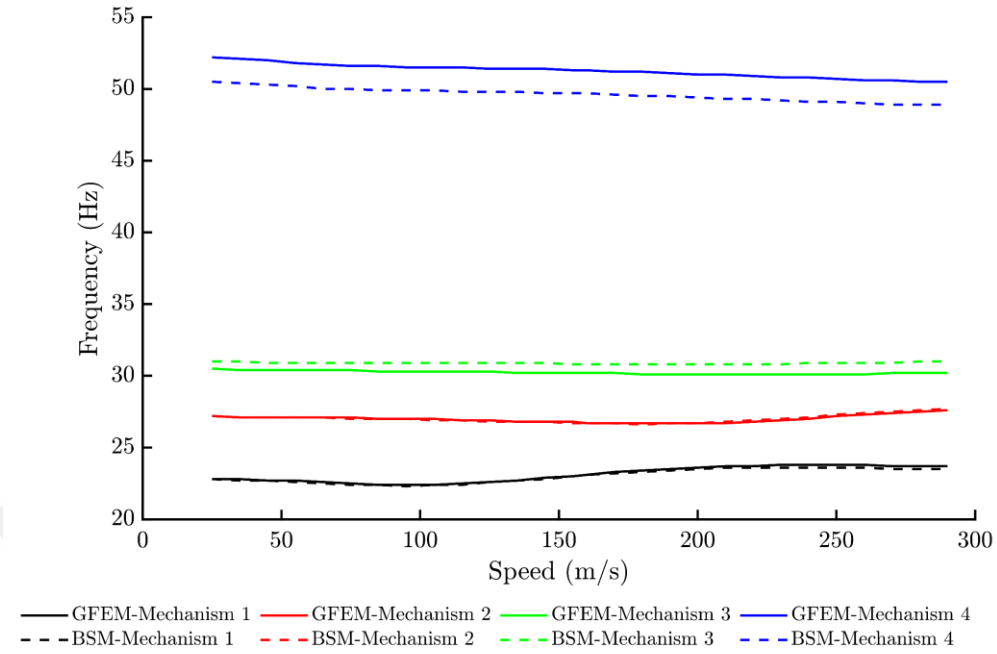

Figure 6.6 Comparison of VF graphs

The point where damping cuts zero on the VG graph is called the flutter velocity. The calculated frequency at the flutter velocity is the flutter frequency. Figure 6.5 and Figure 6.6 show that the similarity is not limited to flutter speeds and frequencies; but the behavior of the two models outside the flutter speed are also similar. This similarity indicates that the BSM retains the basic properties of the structure and accurately represents the aeroelastic interactions.

Another comparison is made for the flutter mode shapes. The flutter mode shapes of both models are given in Figures 6.7, 6.8, 6.9, and 6.10.

Isometric View

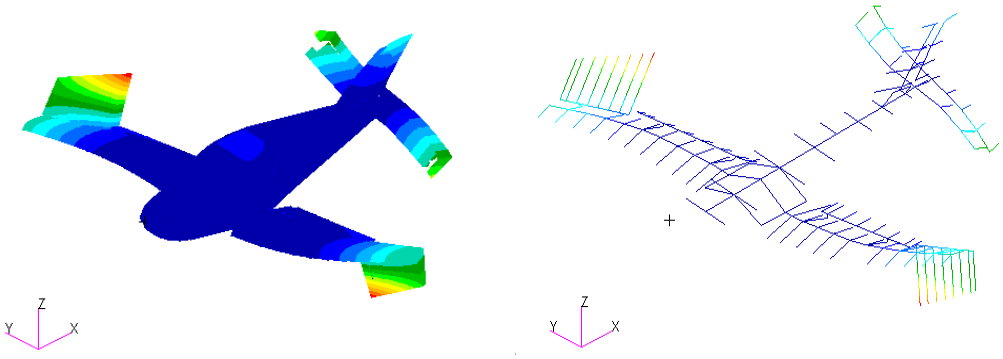

Front view

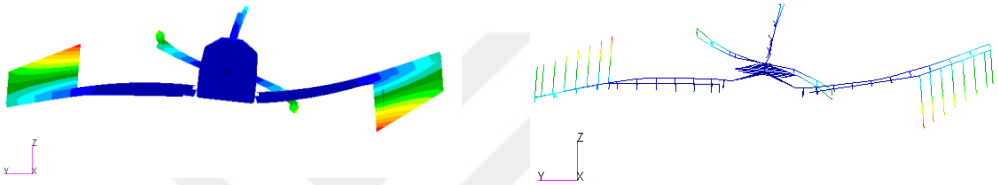

Top view

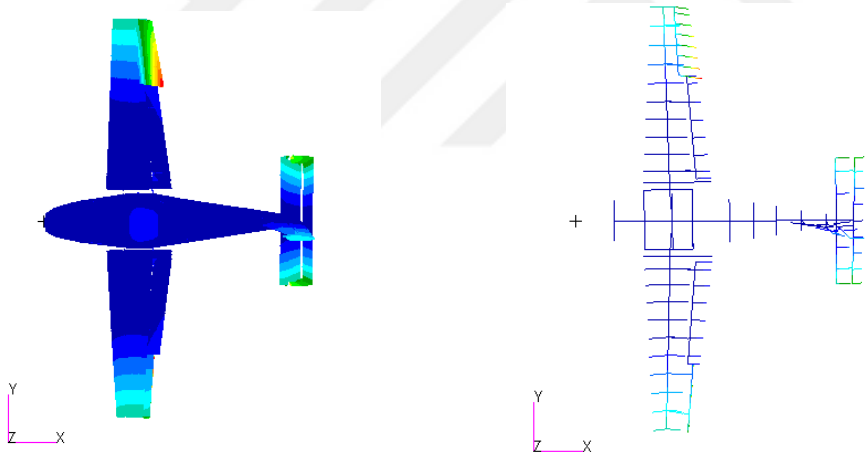

Figure 6.7 Flutter Mechanism 1

Isometric View

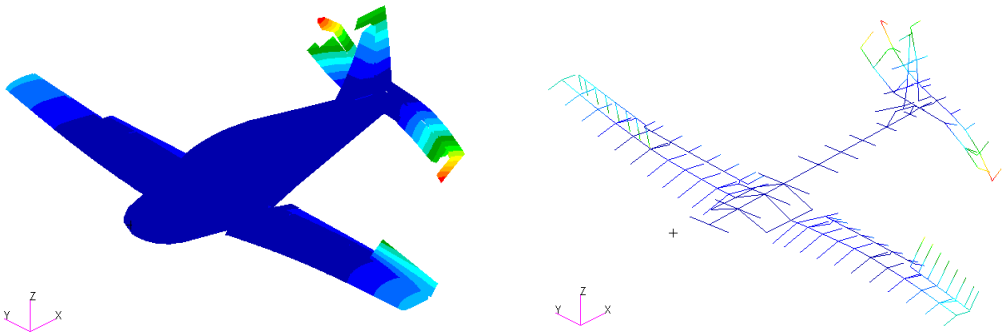

Front view

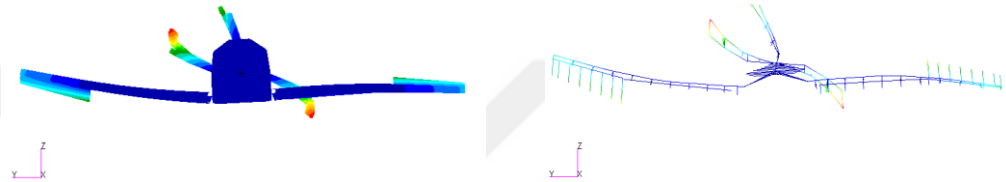

Top view

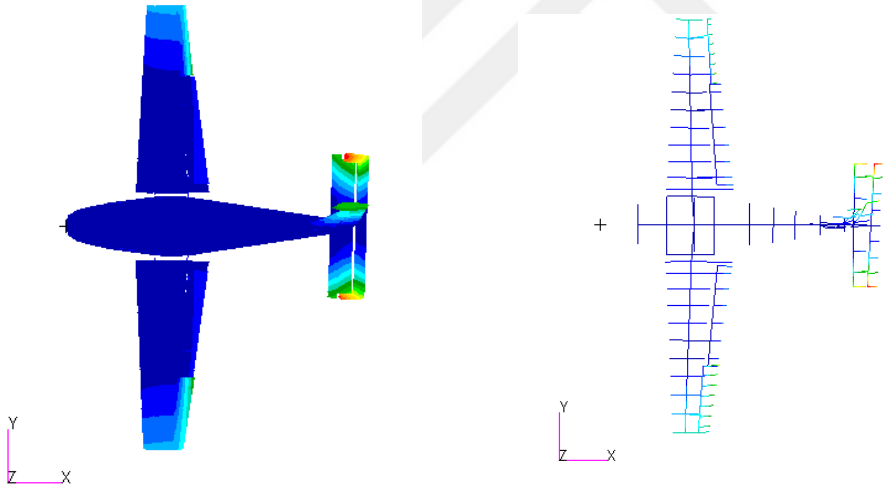

Figure 6.8 Flutter Mechanism 2

Isometric View

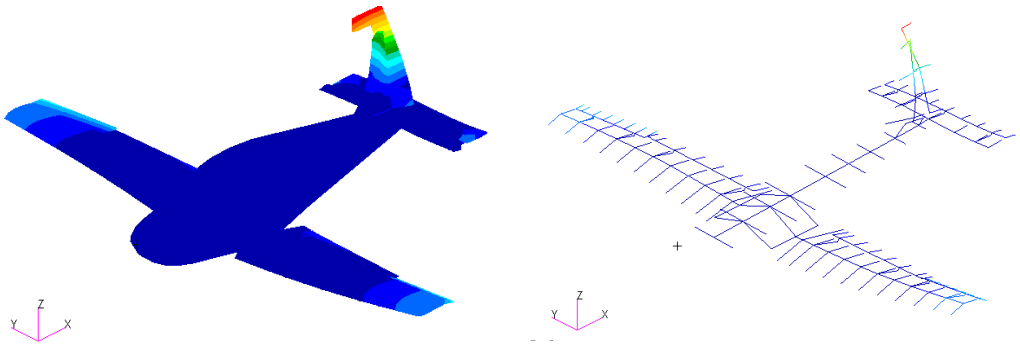

Front view

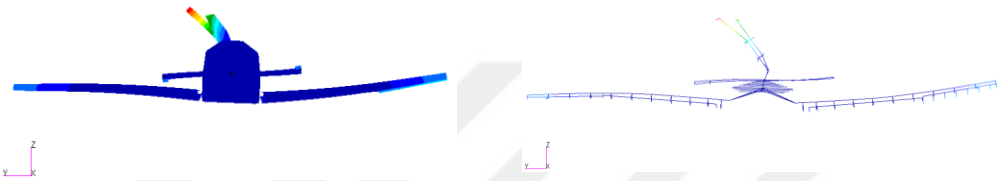

Top view

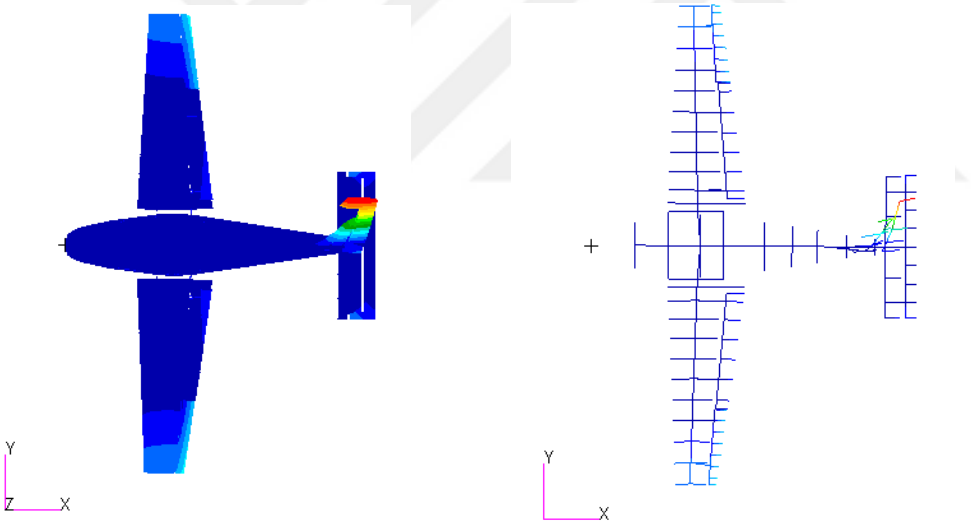

Figure 6.9 Flutter Mechanism 3

Isometric View

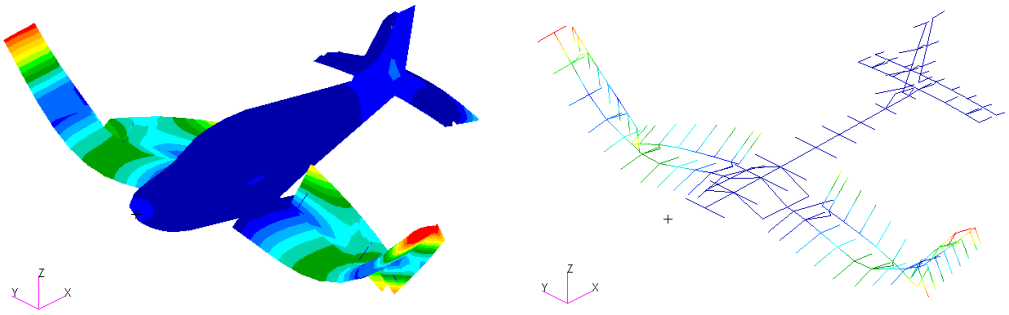

Front view

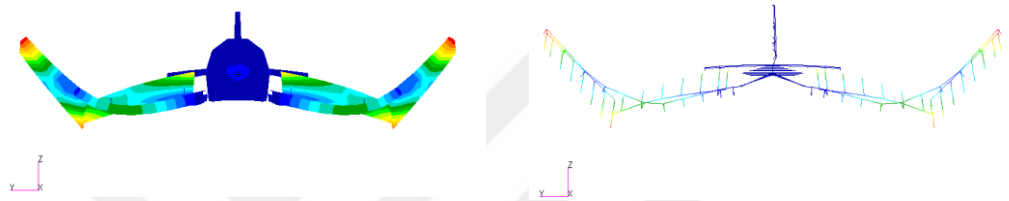

Top view

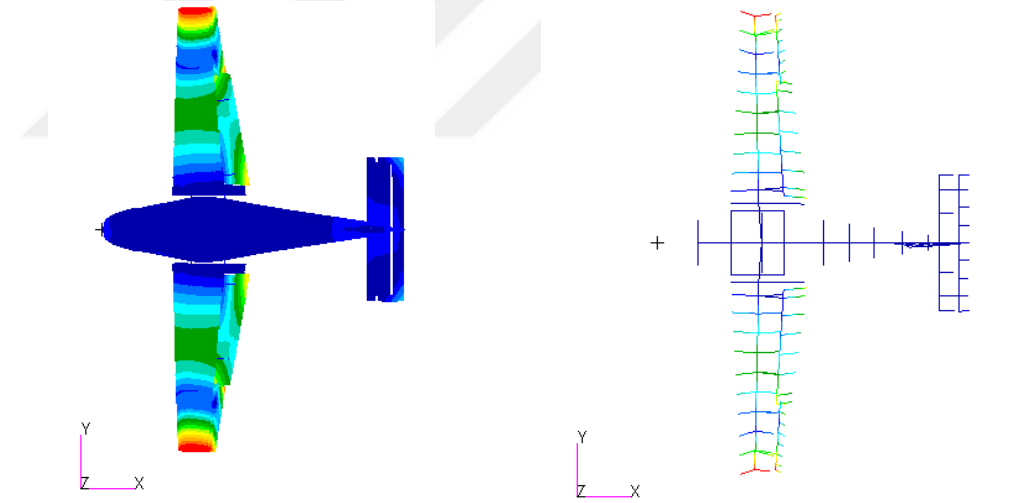

Figure 6.10 Flutter Mechanism 4

Figures 6.7, 6.8, 6.9, and 6.10 show that BSM captures flutter mode shapes accurately. Close similarity indicates that although BSM uses fewer degrees of freedom, it can adequately represent the flutter mode shapes of the GFEM. This shows that BSM can produce reliable results in design analyses and accurately

models the dynamic behavior of the VLA. It should also be noted that all four flutter mechanisms contain control surface motions which are captured by the BSM. This shows that the methodology used for modeling the control surfaces in the BSM works adequately.

6.5 Discrete Gust Analysis of the Very Light Aircraft using the 3D Global Finite Element Model and the Beam Stick Model

Aircraft can be subjected to sudden gust loads in the air. Discrete gust analyses are performed to evaluate the aircraft's response to a sudden change in the direction and magnitude of airspeed. With the discrete gust analysis, displacements and stresses caused by gusts can be calculated.

This section compares the results of the discrete gust analysis of GFEM and BSM. Analyses are performed using Nastran SOL 146. Before comparing the results of the two models, the aeroelastic response theory is explained briefly.

6.5.1 Theory of Dynamic Aeroelastic Response

Nastran performs dynamic response analysis in the frequency domain [40]. However, inputs and outputs in transient response analysis are usually requested in the time domain. For this reason, using the Fourier transform, MSC Nastran switches between the time domain and the frequency domain. Fourier transform is used in three different stages in transient analysis. In the first stage, the loads specified as a function of time are converted into the frequency domain. Secondly, responses are calculated in the frequency domain. The second stage is explained in this section. In the third stage responses are converted back into the time domain from the frequency domain.

Calculation of the responses in the frequency domain is started with Equation 6.8. Equation 6.21 is obtained only when structural and viscous damping are added to the equation.

$$[M_{hh}]\{\ddot{\eta}\} + [B_{hh}]\{\dot{\eta}\} + [i[H_{hh}] + [K_{hh}]]\{\eta\} \\ -q_\infty[Q_{hh}(Mach, k)]\{\eta\} = [\phi^T]F_e(t) \quad (6.21)$$

H_{hh} and B_{hh} are generalized structural and viscous damping given by Equation 6.22 and 6.23, respectively.

$$H_{hh} = [\phi]^T[H][\phi] \quad (6.22)$$

$$B_{hh} = [\phi]^T[B][\phi] \quad (6.23)$$

Equation 6.24 can be written if the matrix H is proportional to the stiffness matrix K,

$$H_{hh} = [\phi]^T\bar{g}[K][\phi] \quad (6.24)$$

where $\bar{g}$ is the modal loss factor in Equation 6.24. Equation 6.21 can be rewritten with the use of Equation 6.24.

$$[M_{hh}]\{\ddot{\eta}\} + [B_{hh}]\{\dot{\eta}\} + [(i + \bar{g})[K_{hh}]]\{\eta\} \\ -q_\infty[Q_{hh}(Mach, k)]\{\eta\} = [\phi^T]F_e(t) \quad (6.25)$$

The solution of the system is assumed to be in the form of simple harmonic motion given by $\{\eta\} = \{\bar{\eta}\}e^{iwt}$. In this case, Equation 6.26 can be written in the following form.

$$[[-M_{hh}]\{\omega^2\} + [iB_{hh}]\{\omega\} + [(i + \bar{g})[K_{hh}] \\ -q_\infty[Q_{hh}(Mach, k)]]\{\bar{\eta}\} = [\phi^T]F_e(t) \quad (6.26)$$

At this point, $F_e(t)$ must be determined for gust problems. A typical illustration of a discrete gust is shown in Figure 6.11.

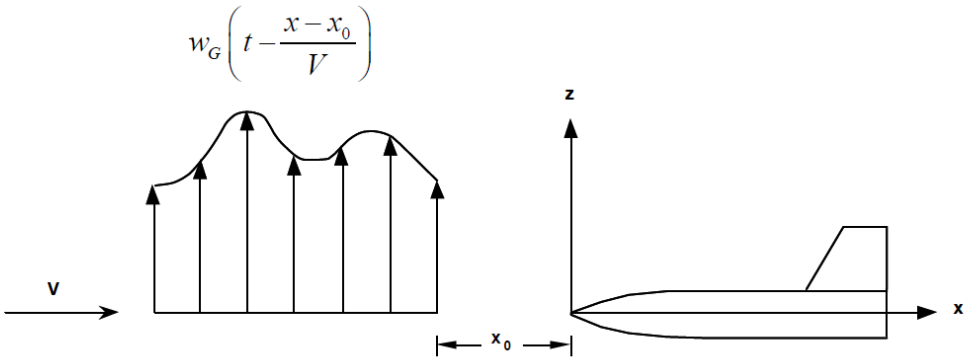

Figure 6.11 Typical Gust Illustration [48]

In Figure 6.11, the discrete gust profile ($w_g(t-\frac{x-x_0}{V})$) approaches to the airplane with a speed of V. x_0 represents the initial distance between the origin of the aircraft origin and the gust. The induced angle of attack at a x location can be expressed as Equation 6.27.

$$\alpha(t) = \frac{w_g\left(t-\frac{x-x_0}{V}\right)}{V} \tag{6.27}$$

τ can be defined as;

$$\tau = t - \frac{x-x_0}{V} \tag{6.28}$$

Convolution integral can be used to determine the aerodynamic forces ($F_e(t)$).

$$F_e(t) = q_\infty \int_0^t \bar{H}\left[\frac{V}{\bar{c}}(t-\tau)\right]\alpha(\tau)d\tau \tag{6.29}$$

In Equation 6.29, the angle of attack is connected to the aerodynamic forces via the convolution integral by the time-domain transfer function $\bar{H}$. $\bar{c}$ is the reference chord length in Equation 6.29. $F_e((t))$ should be converted to the frequency domain. The equivalent of Equation 6.29 [48] in the frequency domain is expressed as,

$$F_e(i\omega) = q_\infty H\left(\frac{i\omega\bar{c}}{V}\right)\alpha(i\omega) \tag{6.30}$$

where $\alpha(i\omega)$ is the frequency domain equivalent of $\alpha(t)$ given by Equation 6.31 [48].

$$\alpha(i\omega) = \frac{1}{V} w_g(i\omega) e^{-i\omega\left(\frac{x-x_0}{V}\right)} \tag{6.31}$$

Frequency domain equivalent of $\bar{H}$ is $H\left(\frac{i\omega\bar{c}}{V}\right)$. The following is the AIC matrix's representation of $H\left(\frac{i\omega\bar{c}}{V}\right)$ [48].

$$H\left(\frac{i\omega\bar{c}}{V}\right) = [\mathrm{AIC(ik)}][-\mathrm{N_z}] \tag{6.32}$$

$\mathrm{N_z}$ is the normal component for vertical gusts along the z axis. Equation 6.33 can be obtained by combining Equations 6.30, 6.31, and 6.32.

$$[\phi^T]F_e(t) = \mathrm{q}_\infty[\phi]^T[G]^T\left[S_{kj}\right]^T[\mathrm{AIC(ik)}][-\mathrm{N_z}]e^{-i\omega\left(\frac{x-x_0}{V}\right)}w_g(i\omega)/\mathrm{V} \tag{6.33}$$

Pressure coefficients are transformed into three forces and three moments on panels using an integration matrix (S_{kj}). Generalized displacements can be found when Equation 6.33 is substituted in Equation 6.26. After the generalized displacements are computed, this data can be used to calculate the physical displacement and the acceleration.

6.5.2 Discrete Gust Analysis Results of the Very Light Aircraft using the 3D Global Finite Element Model and the Beam Stick Model

This section compares GFEM and BSM responses to discrete gust. Gust response analyses are performed using Nastran, Sol 146. The flight condition given during the cruise proposed in the CS-VLA [49] is used. According to the specified certification criterion, the aircraft must be exposed to symmetrical vertical gust in the case of level flight. At the time of the cruise, the speed of the aircraft is accepted as 56.6 m/s, and

its altitude is 7500 ft. Gust-shape is shown in Figure 6.12 and defined in Equation 6.34 [49].

$$U(S) = \frac{U_{de}}{2}\left(1 - \cos\left(\frac{2\pi S}{25\bar{c}}\right)\right) \tag{6.34}$$

where U_{de} is gust velocity and is defined as 15.24 m/s during the cruise. $\bar{c}$ is the mean aerodynamic chord, and the value is 1.223 m. Gust length should be equal $25\bar{c}$ according to CS-VLA [49]. S is the position of the aircraft relative to the gust.

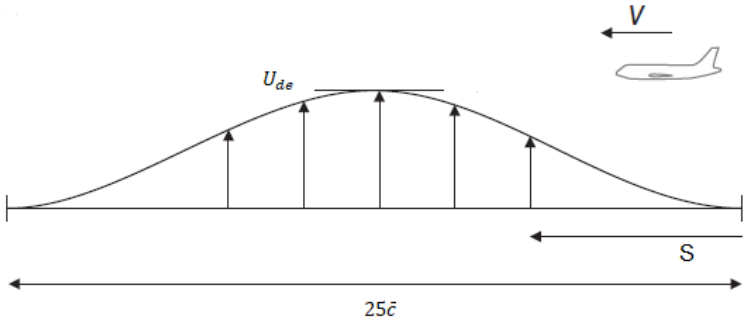

Figure 6.12 Discrete gust profile [1]

The vertical accelerations at the CGs of the two models in the specified flight conditions are compared in Figure 6.13.

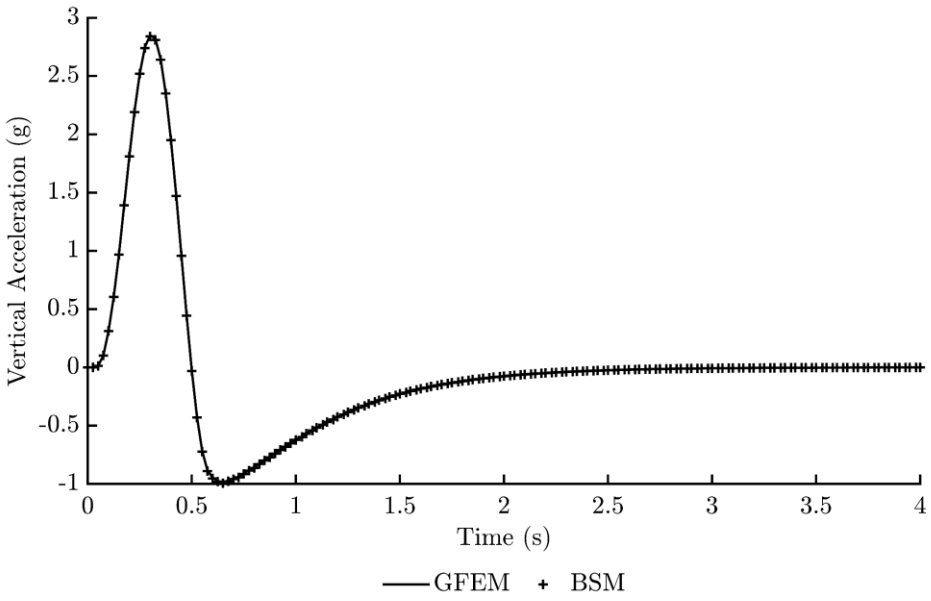

Figure 6.13 Comparison of the vertical acceleration at the CG vs time

Figure 6.13 shows that the responses of the two systems to the discrete gust are on top of each other. Both GFEM and BSM reach maximum acceleration at 0.3 seconds. Maximum acceleration in GFEM is 2.85g, while in BSM, it is 2.84g. The behavior of the two models outside the peak points is also quite similar.

One of the most important outputs of gust response analysis is the internal forces in the aircraft structure. In this respect, shear force and bending moment at the root of the wing calculated by the gust analysis utilizing GFEM and BSM are compared in Figure 6.14 and Figure 6.15.

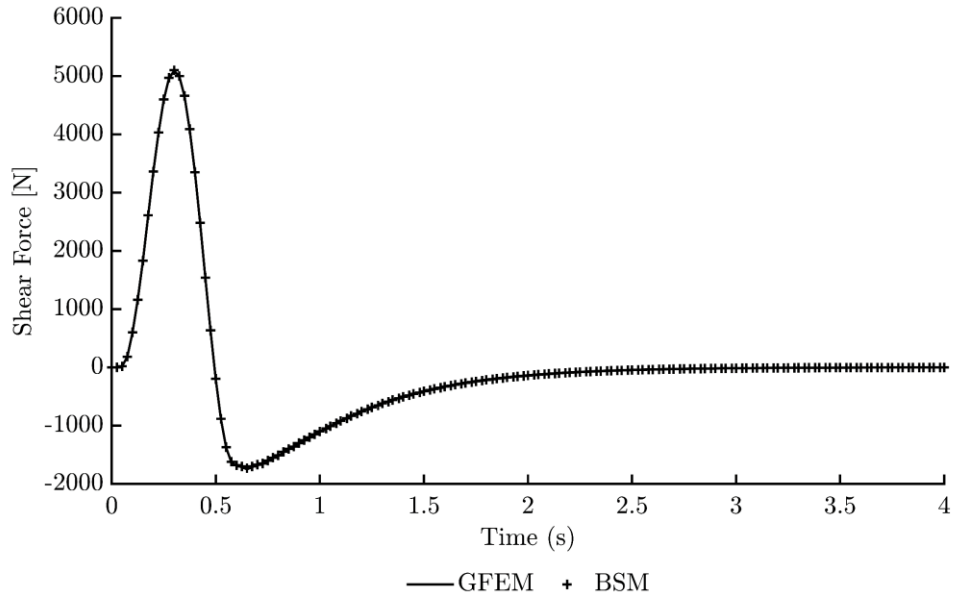

Figure 6.14 Comparison of shear force vs time at the wing root

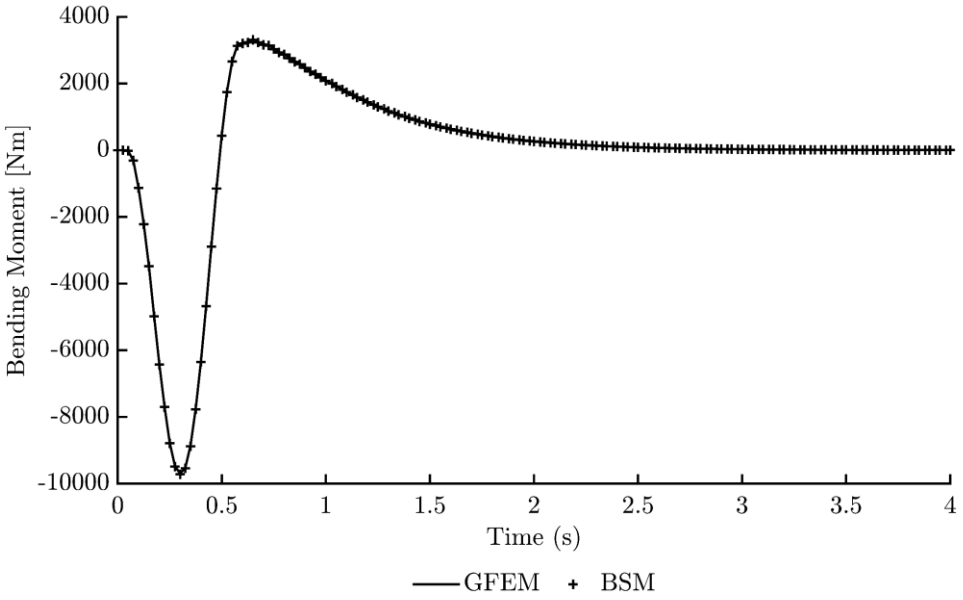

Figure 6.15 Comparison of bending moment vs time at the wing root

The time-dependent variation of shear forces at the wing root is almost the same. While the maximum shear force in GFEM is 5087 N, it is 5096 N in BSM. Both models reached the maximum shear force at 0.3 seconds. The highest negative direction shear is 1745 N in GFEM and 1734 N in BSM. Figure 6.15 shows the time varying bending moment at the root of the wing. It is also seen in this graph that the GFEM and BSM responses are almost identical. The highest bending moment GFEM is exposed to is 9703 Nm. In BSM, it is 9721 Nm.

Discrete gust analysis gives confidence in the reliability of the BSM. However, due to the long gust length, elastic modes may have little contribution to the response in dynamic analysis. Re-analysis can be done by removing rigid body modes from the analysis to see how much the elastic modes affect the response. The result of the analysis, in which rigid body modes are ignored and all elastic modes are included, is given in Figure 6.16 for the vertical acceleration response at the CG of the VLA.

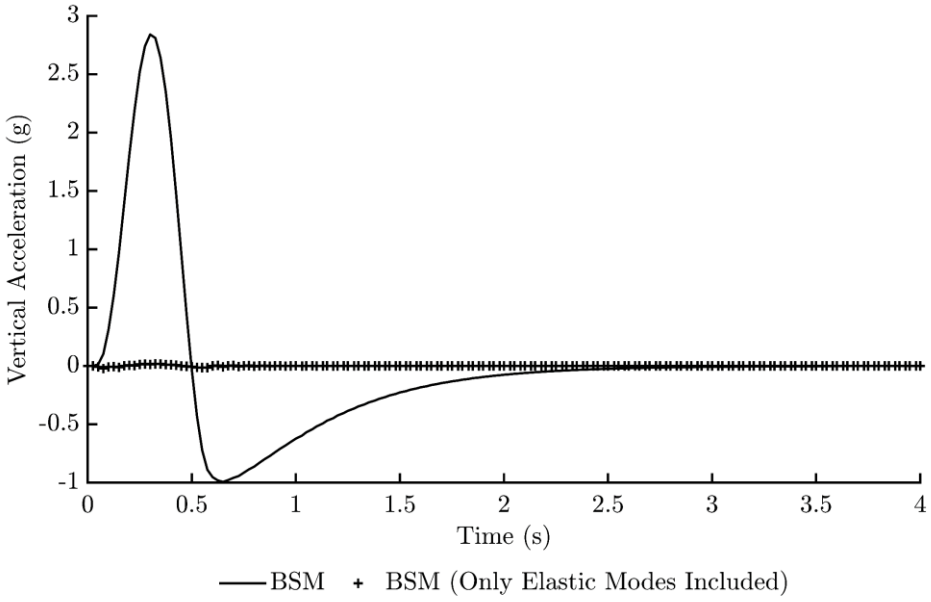

Figure 6.16 Effects of rigid body modes on vertical acceleration at the CG

Figure 6.16 shows that rigid body motions almost wholly dominate the dynamic response. Comparing the BSM and the GFEM by increasing the effect of elastic modes in response is necessary to show the reliability of the BSM. The gust frequency to which the aircraft is exposed is calculated by Equation 6.35.

$$Gust\ Frequency = \frac{Speed\ of\ Aircraft}{Gust\ Length} = \frac{56.6\ m/s}{30.58\ m} = 1.85\ \text{Hz} \qquad (6.35)$$

Since 1.85 Hz is far from the natural frequency of elastic modes, the response is then dominated by rigid body modes. For this reason, vertical acceleration at the CG is calculated by reducing the gust length from 30.58 meters to 3.77 meters. This change in gust length increases the frequency of gusts to 15 Hz. Figure 6.17 compares the vertical acceleration at the CG when the gust length is taken as 3.77 meters.

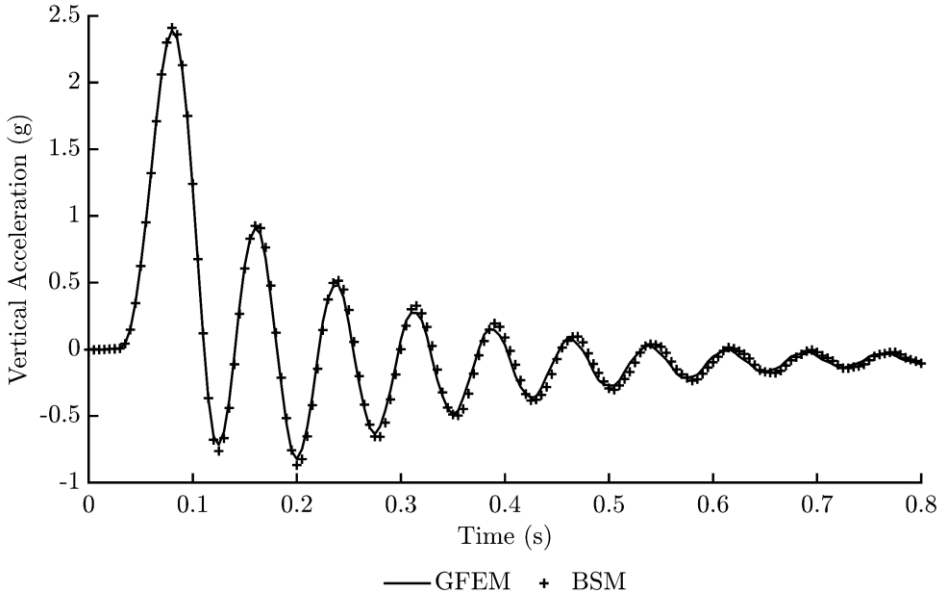

Figure 6.17 Comparison of the vertical acceleration at the CG vs time (gust length = 3.77m)

When the gust length is reduced, the effect of elastic modes on the dynamic response increases. Figure 6.17 shows that BSM and GFEM both give the similar response. The maximum acceleration in GFEM is 2.39g, and maximum acceleration in BSM

is 2.41g. This analysis once again gives confidence for the usability of BSM in dynamic aeroelastic analysis.

6.6 Effect of the Mass Change on the Normal Mode Analysis Results

The main purpose of the BSM is to obtain a reduced order model which is suitable for assessing the effect of design changes on the dynamic characteristics of the aircraft. In this study, in order to test how the BSM responds to design modifications, the mass of the part in the indicated area of Figure 6.18 in the METU VLA wing is increased by twenty percent. By increasing the BSM mass in the same region, the responses of the models are examined.

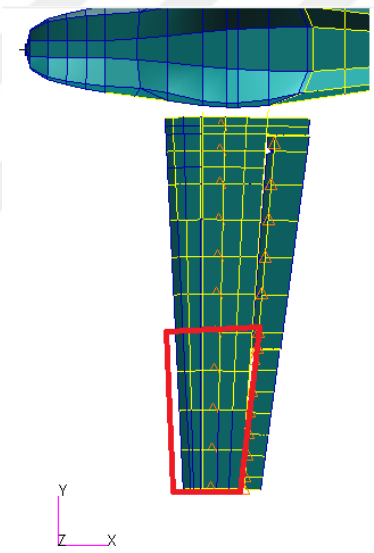

Figure 6.18 Area of increased mass

The impact of 20% mass increase in the indicated region in Figure 6.18 on the elastic modes by the modal analysis performed by the GFEM is given in Table 6.3.

Table 6.3 Effect of the mass change on the natural frequencies of the VLA calculated by the GFEM

Mode Identification	GFEM frequency before mass increase [Hz]	GFEM frequency after mass increase [Hz]
Wing first bending – aileron rotation (S)	12.35	11.69
Aileron rotation (A)	16.97	16.97
Aileron & flap rotation (out of phase) (S)	18.02	17.87
Flap rotation (A)	18.85	18.82
Aileron & flap rotation (in phase) (S)	19.09	18.93
Elevator rotation (S)	21.66	21.66
Wing first bending – aileron rotation (A)	23.12	22.46
Horizontal tail first bending-vertical tail first bending-elevator first bending(A)	27.35	27.15
Vertical tail first bending (A)	30.65	30.46
Rudder rotation (A)	32.70	32.67
Horizontal tail first torsion – elevator first bending (S)	33.60	33.58
Wing second bending (S)	52.36	50.70
Elevator first torsion – horizontal tail first bending (S)	53.26	53.19
Wing second bending (A)	62.56	60.85
Flap first bending (S)	69.65	69.65
Flap first bending (A)	70.40	70.21
Horizontal tail first torsion – elevator second bending (A)	76.81	76.78
Vertical tail first torsion - rudder first bending (A)	82.55	82.47
Horizontal tail first torsion (S)	83.67	N/A

Table 6.3 continued

Wing first torsion (S)	85.42	N/A
Wing first torsion -horizontal tail first torsion (S)	N/A	83.42

When the wing mass is increased, the horizontal tail first torsion (S) and wing first torsion (S) models combine into one mode. This increase in mass is predicted to decrease the natural frequency of the wing first torsion mode more than the natural frequency of the horizontal tail first torsion. Consequently, with the mass increase, two elastic modes with similar natural frequencies become a single elastic mode.

Table 6.4 compares the natural frequencies calculated by the GFEM and BSM corresponding to the 20% mass increase in the indicated region in Figure 6.18.

Table 6.4 Effect of mass change on the normal mode analysis results

Mode Identification	GFEM Frequency [Hz]	BSM Frequency [Hz]	Difference [%]	MAC
Wing first bending – aileron rotation (S)	11.69	11.64	0.48	1.00
Aileron rotation (A)	16.97	17.02	0.29	1.00
Aileron & flap rotation (out of phase) (S)	17.87	17.90	0.19	1.00
Flap rotation (A)	18.82	18.78	0.24	1.00
Aileron & flap rotation (in phase) (S)	18.93	18.86	0.39	1.00
Elevator rotation (S)	21.66	21.94	1.31	0.99
Wing first bending – aileron rotation (A)	22.46	22.43	0.15	0.99
Horizontal tail first bending-vertical tail first bending-elevator first bending(A)	27.15	27.11	0.14	0.99
Vertical tail first bending (A)	30.46	31.00	1.75	0.96

Table 6.4 continued

Rudder rotation (A)	32.67	32.43	0.71	0.99
Horizontal tail first torsion – elevator first bending (S)	33.58	32.59	2.96	0.96
Wing second bending (S)	50.70	49.02	3.31	0.99
Elevator first torsion – horizontal tail first bending (S)	53.19	54.25	1.99	0.98
Wing second bending (A)	60.85	59.64	2.00	0.98
Flap first bending (S)	69.65	69.85	0.28	1.00
Flap first bending (A)	70.21	70.46	0.36	1.00
Horizontal tail first torsion – elevator second bending (A)	76.78	77.66	1.15	0.96
Vertical tail first torsion - rudder first bending (A)	82.47	80.84	1.97	0.86
Wing first torsion - horizontal tail first torsion (S)	83.42	84.08	0.79	0.90

Compared with the baseline results, with the mass increment, natural frequencies decreased as expected, especially for the elastic modes of the wing. It is seen that the natural frequencies change at similar rates in both models. Also, the highest difference in the natural frequencies is 3.31%. The lowest MAC is calculated as 0.86. Almost 90% of the elastic modes have MACs of 0.95 and above. The differences between frequencies calculated by GFEM and BSM of only two modes are greater than two percent. These analyses show that the created BSM can be used in the optimization of the dynamic characteristics of the aircraft.

CHAPTER 7

CONCLUSION

7.1 General Conclusion

Within the scope of the thesis, a new approach is developed to create a BSM that reflects the dynamic characteristics of the aircraft using global optimization algorithm. The concluded results of this study are given below.

- A lumped-based mass model is preferred instead of the density-based mass model, as it reduces local modes, shortens the solution time, and facilitates the BSM developing process. The transition process from a density-based mass model to a lumped-based mass model is explained using the MSC Patran mass properties tool.
- The meta-heuristic algorithm CSA is adapted to use multi-objective functions and variable AP. These modifications aim to make the CSA algorithm better suited to the problem. An optimization code is developed that aims to make the natural frequencies and mode shapes of the BSM as compatible as possible with the 3D GFEM or GVT results by optimizing the design variables.
- It is explained how to build an entire aircraft BSM utilizing component BSMs. First, the BSM of the isolated wing torque box is created. Subsequently, a new methodology is developed to connect control surfaces to lifting surfaces. In this methodology, the BSM of the control surfaces is first created under the free-free boundary condition. The created control surface and lifting surface are then connected to each other. Two connection beams are used for the connection. These connection beams in the BSM connect the control surface to the hinge line and the lifting surface. Similar to the GFEM, there are duplicated nodes on the hinge line. There is a

rotational spring with the same stiffness as that of the GFEM between the duplicated nodes. This connection is illustrated in Figure 5.6. The fuselage is then converted to the BSM using inputs from the isolated fuselage GFEM. In the next step, the fuselage and the wing are assembled. Five beams are used for each fuselage-wing connection to connect the two BSMs. This connection is illustrated in Figure 5.12. After the connection beams are included in the optimization process, the wing-fuselage connection is completed. Subsequently, the vertical tail is converted to the BSM. The isolated GFEM vertical tail-fuselage connection is used when converting the vertical tail to BSM. However, while optimizing the beam properties, the cross-sectional properties of the beam elements previously found for the fuselage are used and they are not included in the optimization process. In this section, only the cross-sectional properties of the vertical tail beams are optimized. An isolated vertical tail model is not used, as in the wing, because the vertical tail is riveted directly to the tail fuselage frames. After this section, the rudder is connected to the system, similar to wing control surfaces. The horizontal tail and elevator conversion process to the BSM is the same as that for the vertical tail and rudder conversion to the BSM. Finally, the horizontal tail and elevator are added to the system, and the BSM creation process is completed.

- The modal analysis results of the created BSM are compared with the corresponding results of the GFEM. Compared to the GFEM results, the highest difference in the natural frequencies of the first twenty elastic modes calculated by the BSM is 3.1%. The difference in the natural frequencies of 18 of the 20 elastic modes is below 2%. A high similarity rate is also achieved in the mode shapes. The lowest MAC ratio is calculated as 0.88. Moreover, 18 of the 20 elastic modes have a MAC ratio above 0.95. A high similarity rate is also obtained in the models in which the control surface motions are dominant. This shows that the proposed methodology of generating the BSM of the control surfaces and connecting control surfaces to the main surfaces is reliable.

- The behavior of GFEM and BSM in dynamic aeroelasticity analyses is investigated. Four flutter mechanisms are determined in the flutter analysis results in both GFEM and BSM. When flutter speeds are examined, it is seen that the highest difference is 4.5%. The highest difference in flutter frequencies is 3.3%. The VG and VF graphs of the two models are given in Figure 6.5 and Figure 6.6, respectively. It is seen that the behavior of VG and VF is quite similar for both models. In addition, flutter mode shapes are compared in Figures 6.7, 6.8, 6.9, and 6.10. Although BSM uses much fewer elements, it is observed that it captures the flutter mode shapes of the four different flutter mechanisms.
- Dynamic responses of GFEM and BSM when exposed to discrete gust are examined. Comparing the vertical accelerations of the two models at the CG, the maximum acceleration in GFEM is 2.85g, while it is 2.84g in BSM. Apart from these, the bending moment and shear force of the GFEM and the BSM are compared at the wing root under discrete gust loading. The difference in maximum bending moment is 0.19%, and in maximum shear force is 0.63%. The study also examines how the models respond to gusts of varying lengths. It is shown that by shortening the gust length, the elastic modes contribute more to the dynamic response. In case of reduced gust length (3.77 m), maximum vertical acceleration at the CG is calculated as 2.39g utilizing GFEM and as 2.41g utilizing BSM.
- BSM is also checked for its capability in responding to local mass changes which frequently occur in aircraft design process. Since in the developed BSM mass distribution is taken as same as in GFEM, it is not required to perform another optimization for the beam properties of the BSM. In this respect, in GFEM and BSM, the masses of specific wing parts are increased, and modal analysis is performed again. With the mass increment, the rate of decrease in natural frequencies in the two models is quite similar. The highest difference in natural frequencies is found to be 3.31%. The lowest MAC rate

is calculated as 0.86. It is shown that almost 90% of the elastic modes MAC values are 0.95 and above.

- Considering all the results, it is seen that the differences between the two models are at an acceptable level. Similar responses are observed in the dynamic aeroelasticity analyses of the two models. Hence, comparative results show that proposed BSM generation method produced very accurate BSM which can be used in the dynamic analysis of the aircraft with confidence.

7.2 Future Studies

Recommended future studies are listed below.

- Solution times are pretty long in nonlinear aeroelasticity and aeroservoelastic analyses. The generated BSM can be tested in nonlinear aeroelasticity and aeroservoelastic studies. The use of BSM in such analyses will significantly shorten the solution time.
- The current BSM only focuses on natural frequencies and mode shapes, making it only suitable for dynamic analysis. However, adding an objective function for displacement can make it suitable for both dynamic and static analysis. The code can calculate the stiffness matrix and provide direct displacement calculations for various applied forces. A BSM can be created to give the same displacements under the same force as the GFEM, but adding an objective function may make it challenging to find eigenvalues and eigenvectors. Adding an additional objective function to the BSM creation process results in a more consistent system stiffness. This may eliminate the need for the repeated BSM creation process for local stiffness changes. In order to make the BSM suitable for the new configuration, some local stiffness of the BSM can be changed like local mass change.

REFERENCES

[1] J. R. Wright and J. E. Cooper, *Introduction to Aircraft Aeroelasticity and Loads: Second Edition*. 2015. doi: 10.1002/9781118700440.

[2] Y. C. Fung, *An Introduction to the Theory of Aeroelasticity*. New York: Dover Publications, 1969.

[3] R. Cirillo, "Detailed and Condensed Finite Element Models for Dynamic Analysis of a Business Jet Aircraft," M.S. thesis, The University of Politecnico di Milano, Milano, 2010.

[4] A. Askarzadeh, "A novel metaheuristic method for solving constrained engineering optimization problems: Crow search algorithm," *Comput Struct*, vol. 169, pp. 1–12, Jun. 2016, doi: 10.1016/j.compstruc.2016.03.001.

[5] M. S. A. El Sayed, M. A. Gutierrez Contreras, and N. Stathopoulos, "Monitor Points Method for Loads Recovery in Static/Dynamic Aeroelasticity Analysis with Hybrid Airframe Representation," *SAE International Journal of Aerospace*, vol. 6, no. 2, pp. 2013-01–2142, Sep. 2013, doi: 10.4271/2013-01-2142.

[6] A. K. Singh and C. W. Nichols, "Derivation of an Equivalent Beam Model from a Structural Finite Element Model," in *Proceedings of the MSC 1988 World Users Conference*, Los Angeles, 1988.

[7] G. Corriveau and F. Dervault, "Impact of Wing Box Geometrical Parameters on Stick Model Prediction Accuracy," in *54th AIAA/ASME/ASCE/AHS/ASC Structures, Structural Dynamics, and Materials Conference*, Reston, Virginia: American Institute of Aeronautics and Astronautics, Apr. 2013. doi: 10.2514/6.2013-1810.

[8] J. Jones and C. E. Cesnik, "Nonlinear Aeroelastic Analysis of the X-56 Multi-Utility Aeroelastic Demonstrator," in *15th Dynamics Specialists*

Conference, Reston, Virginia: American Institute of Aeronautics and Astronautics, Jan. 2016. doi: 10.2514/6.2016-1799.

[9] M. Hashemi-Kia and M. Toossi, "Development and Application of a Technique for Reducing Airframe Finite Element Models for Dynamic Analysis," Mesa, 1990.

[10] U. Hayirli and A. Kayran, "Stick Model Development of Aircraft Structures for Dynamic Analysis," in *58th AIAA/ASCE/AHS/ASC Structures, Structural Dynamics, and Materials Conference*, Reston, Virginia: American Institute of Aeronautics and Astronautics, Jan. 2017. doi: 10.2514/6.2017-0407.

[11] P. Hajela and J. L. Chen, "Preliminary Weight Estimation of Conventional and Joined Wings Using Equivalent Beam Models," *J Aircr*, vol. 25, no. 6, pp. 574–576, Jun. 1988, doi: 10.2514/3.45625.

[12] S. Corn, J. Piranda, and N. Bouhaddi, "Simplification of Finite Element Models for Structures Having a Beam-Like Behaviour," *J Sound Vib*, vol. 232, no. 2, pp. 331–354, Apr. 2000, doi: 10.1006/jsvi.1999.2746.

[13] S. P. Timoshenko, "On the Transverse Vibrations of Bars of Uniform Cross Section," *Philosophical Magazine*, pp. 125–131, 1922.

[14] P. Piperni, M. Abdo, and F. Fafyeke, "The Application of Multi-Disciplinary Optimization Technologies to the Design of a Business Jet," in *10th AIAA/ISSMO Multidisciplinary Analysis and Optimization Conference*, Reston, Virigina: American Institute of Aeronautics and Astronautics, Aug. 2004. doi: 10.2514/6.2004-4370.

[15] M. S. A. Elsayed, R. Sedaghati, and M. Abdo, "Accurate Stick Model Development for Static Analysis of Complex Aircraft Wing-Box Structures," *AIAA Journal*, vol. 47, no. 9, pp. 2063–2075, Sep. 2009, doi: 10.2514/1.38447.

[16] G. Bindolino, G. Ghiringhelli, S. Ricci, and M. Terraneo, “Multilevel Structural Optimization for Preliminary Wing-Box Weight Estimation,” *J Aircr*, vol. 47, no. 2, pp. 475–489, Mar. 2010, doi: 10.2514/1.41552.

[17] R. Palacios, Y. Wang, A. Wynn, and M. Karpel, “Condensation of Large Finite-Element Models for Wing Load Analysis with Geometrically-Nonlinear Effects,” in *IFASD*, Bristol, Jun. 2013.

[18] E. Carrera, A. Pagani, and M. Petrolo, “Classical, Refined, and Component-Wise Analysis of Reinforced-Shell Wing Structures,” *AIAA Journal*, vol. 51, no. 5, pp. 1255–1268, May 2013, doi: 10.2514/1.J052331.

[19] L. Euler, *De Curvis Elasticis*. Lausanne, 1744.

[20] A. Pagani, “Component-Wise Models for Static, Dynamic and Aeroelastic Analyses of Metallic and Composite Aerospace Structures,” Ph.D dissertation, Politecnico di Torino, Torino, 2015.

[21] J. Cecrdle, “Some Special Modelling Techniques For Preparation of Aeroelastic Stick Models,” in *IFASD*, Como, Jun. 2017.

[22] A. Kratochví, “A New Approach of Creating a Finite Element Stick Model for Flutter Analysis,” *MATEC Web of Conferences*, vol. 304, Dec. 2019, doi: 10.1051/matecconf/201930401015.

[23] M. Gupta, D. Sarojini, A. Shah, and D. H. Hodges, “Beam Theory for Asymptotic Analysis of Aperiodic and Inhomogeneous Structures,” *AIAA Journal*, vol. 57, no. 10, pp. 4155–4168, Oct. 2019, doi: 10.2514/1.J057563.

[24] D. Sarojini, M. Gupta, D. H. Hodges, and D. N. Mavris, “An Efficient Method to Dimensionally Reduce Aperiodic Inhomogeneous 3-D Structures to 1-D Beam-Like Structures,” in *AIAA Scitech 2020 Forum*, Reston, Virginia: American Institute of Aeronautics and Astronautics, Jan. 2020. doi: 10.2514/6.2020-0272.

[25] S. A. Dunn, “The Use of Genetic Algorithms in Dynamic Finite Element Model Identification for Aerospace Structures,” in *20th Congress of the International Council of the Aeronautical Sciences*, Reston, Virginia, USA, 1996.

[26] S. A. Dunn, “Modified Genetic Algorithm for the Identification of Aircraft Structures,” *J Aircr*, vol. 34, no. 2, pp. 251–253, Mar. 1997, doi: 10.2514/2.7569.

[27] S. A. Dunn, “Optimisation of the Structural Dynamic Finite Element Model for a Complete Aircraft,” in *21st Congress of the International Council of the Aeronautical Sciences*, Melbourne, Victoria, Australia, Sep. 1998.

[28] S. A. Dunn, “The use of genetic algorithms and stochastic hill-climbing in dynamic finite element model identification,” *Comput Struct*, vol. 66, no. 4, pp. 489–497, Feb. 1998, doi: 10.1016/S0045-7949(97)00092-8.

[29] S. A. Dunn, “Technique for Unique Optimization of Dynamic Finite Element Models,” *J Aircr*, vol. 36, no. 6, pp. 919–925, Nov. 1999, doi: 10.2514/2.2552.

[30] P. M. Trivailo, T. Gilbert, E. Glessich, and D. Sgarioto, “Inverse problem of aircraft structural parameter identification: application of genetic algorithms compared with artificial neural networks,” *Inverse Probl Sci Eng*, vol. 14, no. 4, pp. 337–350, Jun. 2006, doi: 10.1080/17415970600573338.

[31] P. V. Thomas, “Development and Design Optimization of High fidelity Reduced Order Models for Dynamic Aeroelasticity Loads Analyses of Complex Airframes,” M.S. thesis, Carleton University, Ottawa, Ontario, 2018.

[32] J. Navrátil, “New Approaches in Numerical Aeroelasticity Applied in Aerodynamic Optimization of Elastic Wing,” Ph.D dissertation, Brno University of Technology, Brno, 2016.

[33] R. J. Guyan, “Reduction of stiffness and mass matrices,” *AIAA Journal*, vol. 3, no. 2, pp. 380–380, Feb. 1965, doi: 10.2514/3.2874.

[34] B. Irons, “Structural eigenvalue problems - elimination of unwanted variables,” *AIAA Journal*, vol. 3, no. 5, pp. 961–962, May 1965, doi: 10.2514/3.3027.

[35] J. O’Callahan, “A Procedure for an Improved Reduced System (IRS) Model,” in *7th International Modal Analysis Conference*, 1989, pp. 17–21.

[36] J. O’Callahan, P. Avitabile, and R. Riemer, “System Equivalent Reduction Expansion Process (SEREP),” in *7th International Modal Analysis Conference*, 1989.

[37] R. R. Craig and M. C. C. Bampton, “Coupling of substructures for dynamic analyses.,” *AIAA Journal*, vol. 6, no. 7, pp. 1313–1319, Jul. 1968, doi: 10.2514/3.4741.

[38] A. Y.-T. Leung, “An accurate method of dynamic condensation in structural analysis,” *Int J Numer Methods Eng*, vol. 12, no. 11, pp. 1705–1715, 1978, doi: 10.1002/nme.1620121108.

[39] E. ALBANO and W. P. RODDEN, “A doublet-lattice method for calculating lift distributions on oscillating surfaces in subsonic flows.,” *AIAA Journal*, vol. 7, no. 2, pp. 279–285, Feb. 1969, doi: 10.2514/3.5086.

[40] MSC Software Corporation, *MSC Nastran Aeroelastic Analysis User’s Guide*. 2021.

[41] ZONA TECHNOLOGY INC, *ZAERO USER’S MANUAL*, Version 9.3. 2019.

[42] R. L. HARDER and R. N. DESMARAIS, “Interpolation using surface splines.,” *J Aircr*, vol. 9, no. 2, pp. 189–191, Feb. 1972, doi: 10.2514/3.44330.

[43] ZONA TECHNOLOGY INC, “ZAERO Basic Training,” 2020.

[44] Y. Meraihi, A. B. Gabis, A. Ramdane-Cherif, and D. Acheli, “A comprehensive survey of Crow Search Algorithm and its applications,” *Artif Intell Rev*, vol. 54, no. 4, pp. 2669–2716, Apr. 2021, doi: 10.1007/s10462-020-09911-9.

[45] MSC Software, “Quick Reference Guide,” Nov. 2011.

[46] A. E. Smith and D. W. Coit, “Penalty functions,” in *Evolutionary Computation 2*, IOP Publishing Ltd. doi: 10.1887/0750306653/b840c7.

[47] H. J. HASSIG, “An approximate true damping solution of the flutter equation by determinant iteration.,” *J Aircr*, vol. 8, no. 11, pp. 885–889, Nov. 1971, doi: 10.2514/3.44311.

[48] ZONA TECHNOLOGY INC, “ZAERO THEORETICAL MANUAL,” vol. Version 9.3, 2017.

[49] EASA, “Certification Specifications for Very Light Aeroplanes,” Nov. 2003.

[50] Klaus-Jürgen Bathe, *Finite Element Procedures*. 1996.

[51] J. Duan and Y.-G. Li, “About the Finite Element Analysis for Beam-Hinged Frame,” in *Proceedings of the 2017 6th International Conference on Energy and Environmental Protection (ICEEP 2017)*, Paris, France: Atlantis Press, 2017. doi: 10.2991/iceep-17.2017.40.

APPENDICES

A. Element Stiffness Matrix of a Beam

The element stiffness matrix of a 3D beam element is given in Figure A.1 [50], [51]. Figure A.1, E represents the elastic modulus, A represents the cross-sectional area, l represents element length, I stands for the moment of inertia, J is the polar moment. A beam element comprises two nodes, and each node possesses six DOFs that include translations and rotations along each axis.

$$\begin{pmatrix}
\frac{EA}{l} & 0 & 0 & 0 & 0 & 0 & -\frac{EA}{l} & 0 & 0 & 0 & 0 & 0 \\
0 & \frac{12EI_z}{l^3} & 0 & 0 & 0 & \frac{6EI_z}{l^2} & 0 & -\frac{12EI_z}{l^3} & 0 & 0 & 0 & \frac{6EI_z}{l^2} \\
0 & 0 & \frac{12EI_y}{l^3} & 0 & -\frac{6EI_y}{l^2} & 0 & 0 & 0 & -\frac{12EI_y}{l^3} & 0 & -\frac{6EI_y}{l^2} & 0 \\
0 & 0 & 0 & \frac{GJ}{l} & 0 & 0 & 0 & 0 & 0 & -\frac{GJ}{l} & 0 & 0 \\
0 & 0 & -\frac{6EI_y}{l^2} & 0 & \frac{4EI_y}{l} & 0 & 0 & 0 & 0 & 0 & \frac{2EI_y}{l} & 0 \\
0 & \frac{6EI_z}{l^2} & 0 & 0 & 0 & \frac{4EI_z}{l} & 0 & 0 & 0 & 0 & 0 & \frac{2EI_z}{l} \\
-\frac{EA}{l} & 0 & 0 & 0 & 0 & 0 & \frac{EA}{l} & 0 & 0 & 0 & 0 & 0 \\
0 & -\frac{12EI_z}{l^3} & 0 & 0 & 0 & 0 & 0 & \frac{12EI_z}{l^3} & 0 & 0 & 0 & -\frac{6EI_z}{l^2} \\
0 & 0 & -\frac{12EI_y}{l^3} & 0 & 0 & 0 & 0 & 0 & \frac{12EI_y}{l^3} & 0 & \frac{6EI_y}{l^2} & 0 \\
0 & 0 & 0 & -\frac{GJ}{l} & 0 & 0 & 0 & 0 & 0 & \frac{GJ}{l} & 0 & 0 \\
0 & 0 & -\frac{6EI_y}{l^2} & 0 & \frac{2EI_y}{l} & 0 & 0 & 0 & \frac{6EI_y}{l^2} & 0 & \frac{4EI_y}{l} & 0 \\
0 & \frac{6EI_z}{l^2} & 0 & 0 & 0 & \frac{2EI_z}{l} & 0 & -\frac{6EI_z}{l^2} & 0 & 0 & 0 & \frac{4EI_z}{l}
\end{pmatrix}$$

Figure A.1 Element stiffness of matrix of a beam element [51]

B. Cross-sectional Properties of the Beam Stick Model

Appendix B gives the beam properties obtained from the optimization code. Firstly, the beam properties used in the wing, flap and aileron are shown in Table B.1. All of the beam properties used in Table B.1 are given according to the element coordinate frames. Figure B.1 to B.3 show element numbering and element coordinate frames.

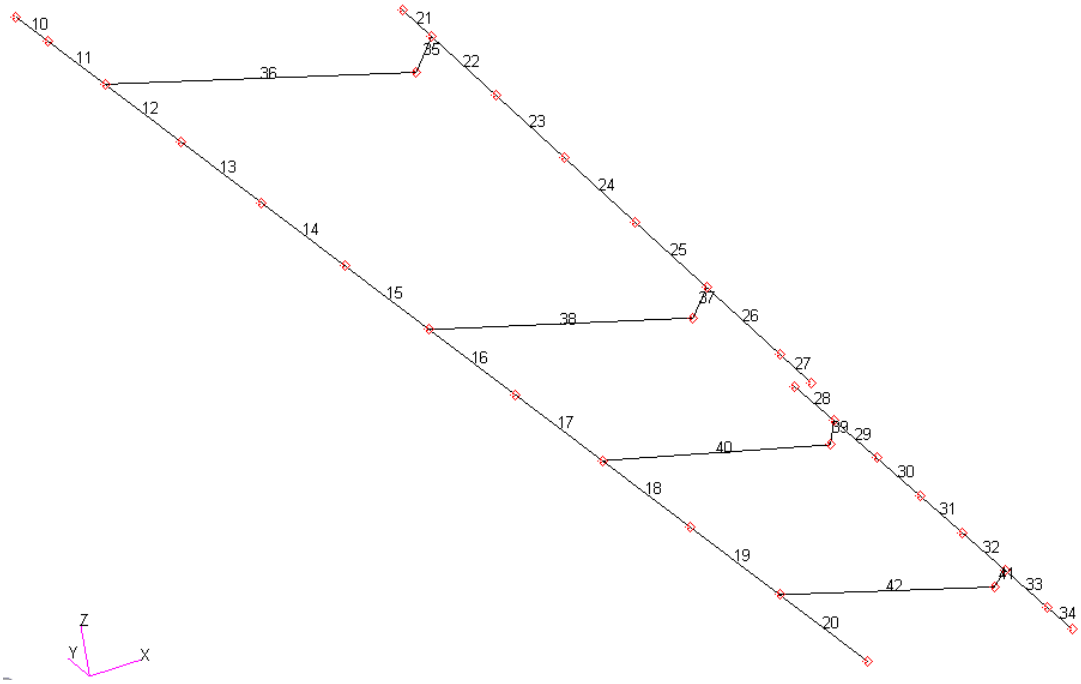

Figure B.1 Numbering of beam elements in the wing

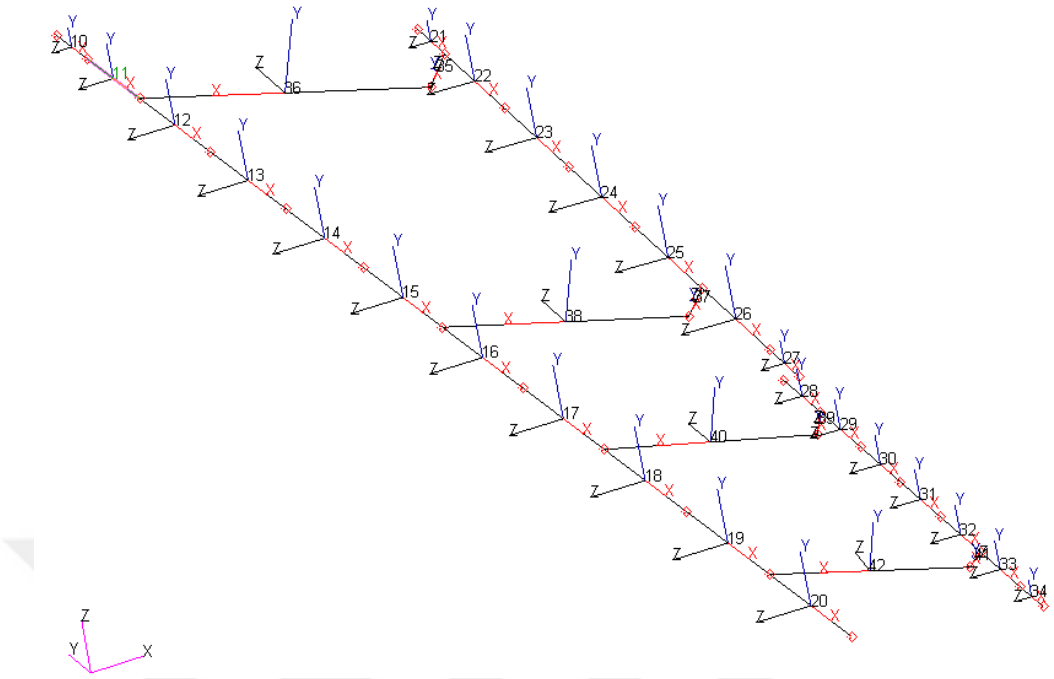

Figure B.2 Element coordinate frames of beam elements in the wing

Coordinate frames of elements 35, 37, 39, and 41 are not clear. Therefore, the zoomed view of the specified elements is given in Figure B.3.

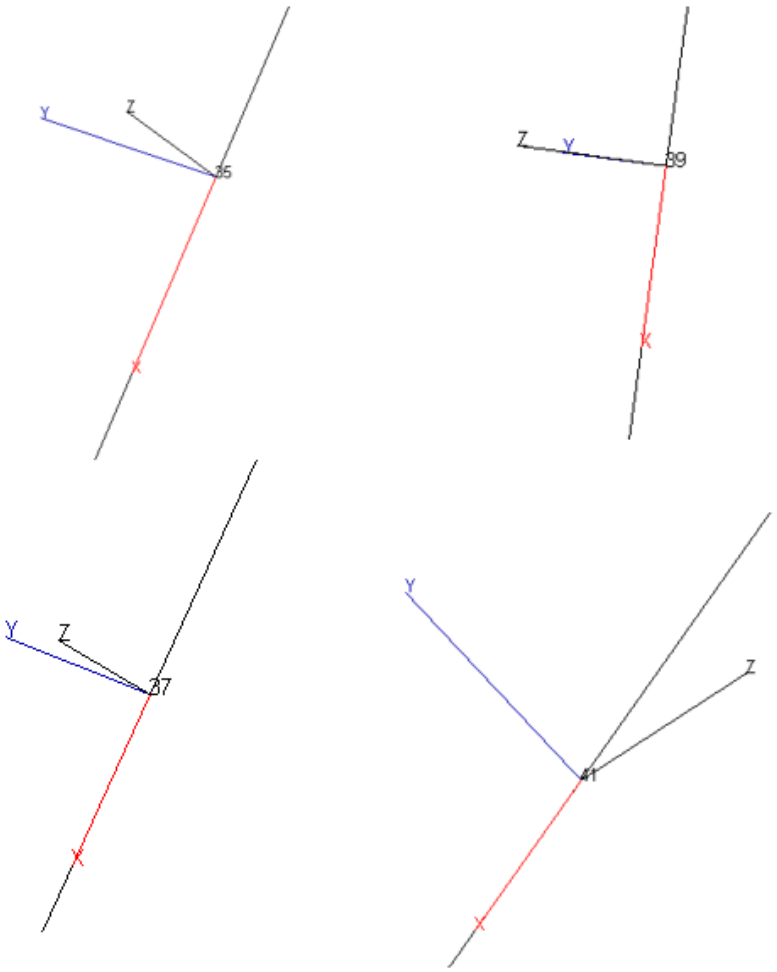

Figure B.3 Zoomed view of beam elements 35, 37, 39, 41

Table B.1 Cross sectional properties of the beam elements in the wing

Number of the Beam Element	*Cross sectional area [mm²]*	I_{zz} *[mm⁴]*	I_{yy} *[mm⁴]*	*J [mm⁴]*
10	7.87E+05	3.17E+06	1.59E+08	1.01E+07
11	1.51E+03	5.50E+03	1.19E+06	1.10E+07
12	2.12E+06	3.51E+06	3.63E+08	1.64E+07
13	4.89E+06	1.88E+06	3.33E+08	1.29E+07
14	1.61E+06	3.30E+06	9.88E+08	3.06E+07
15	1.05E+06	3.29E+03	1.85E+08	7.62E+06
16	6.28E+05	9.23E+04	2.45E+08	5.44E+06
17	6.24E+06	1.83E+06	4.95E+08	4.56E+06
18	8.27E+01	1.89E+03	2.31E+05	3.94E+06
19	5.08E+06	1.64E+07	1.06E+09	3.22E+06
20	1.11E+06	3.64E+06	4.98E+08	6.03E+06
21	3.33E+03	3.65E+03	6.08E+05	1.70E+03
22	6.84E+01	3.90E+02	9.46E+03	3.45E+03
23	7.13E+02	4.16E+02	3.24E+05	2.89E+03
24	5.84E+01	3.65E+02	1.45E+04	2.86E+03
25	5.54E+01	3.22E+02	1.25E+04	2.28E+03
26	6.43E+02	2.47E+02	1.29E+05	3.26E+03
27	1.80E+03	2.27E+03	3.19E+05	1.46E+03
28	1.00E+00	1.00E+00	1.00E+00	1.00E+00
29	1.00E+00	1.00E+00	1.00E+00	1.00E+00
30	1.00E+00	1.00E+00	1.00E+00	1.00E+00
31	1.00E+00	1.00E+00	1.00E+00	1.00E+00
32	1.00E+00	1.00E+00	1.00E+00	1.00E+00
33	1.00E+00	1.00E+00	1.00E+00	1.00E+00
34	1.00E+00	1.00E+00	1.00E+00	1.00E+00
35	8.70E-01	1.39E+00	8.98E+01	8.07E-01
36	1.02E+00	6.25E+00	1.55E-01	4.92E-01
37	5.18E-01	1.30E+00	4.87E+01	5.98E-01
38	1.23E+00	2.49E+00	4.56E+01	5.25E-01
39	9.50E-01	5.67E-01	7.58E+01	9.72E-01

Table B.1 continued

40	7.92E-01	4.18E-01	1.00E+02	5.53E-01
41	1.14E+00	5.44E-01	4.46E+01	6.83E-01
42	8.27E-01	1.79E+00	5.44E+01	6.42E-01
Elastic Modulus (Torque Box)	9.59e+07 N/mm^2			
Shear Modulus (Torque Box)	1.89e+05 N/mm^2			
Elastic Modulus (Flap)	9.49e+07 N/mm^2			
Shear Modulus (Flap)	1.11e+07 N/mm^2			
Elastic Modulus (Aileron)	1.00e+12 N/mm^2			
Shear Modulus (Aileron)	1.00e+12 N/mm^2			
Elastic Modulus (Connection beams)	3.41e+10 N/mm^2			
Shear Modulus (Connection beams)	2.96e+10 N/mm^2			

Secondly, the cross-sectional properties of the fuselage and the wing-fuselage connection are given in Table B.2. Element numbers and element coordinate frames are shown in Figure B.4 and B.5, respectively.

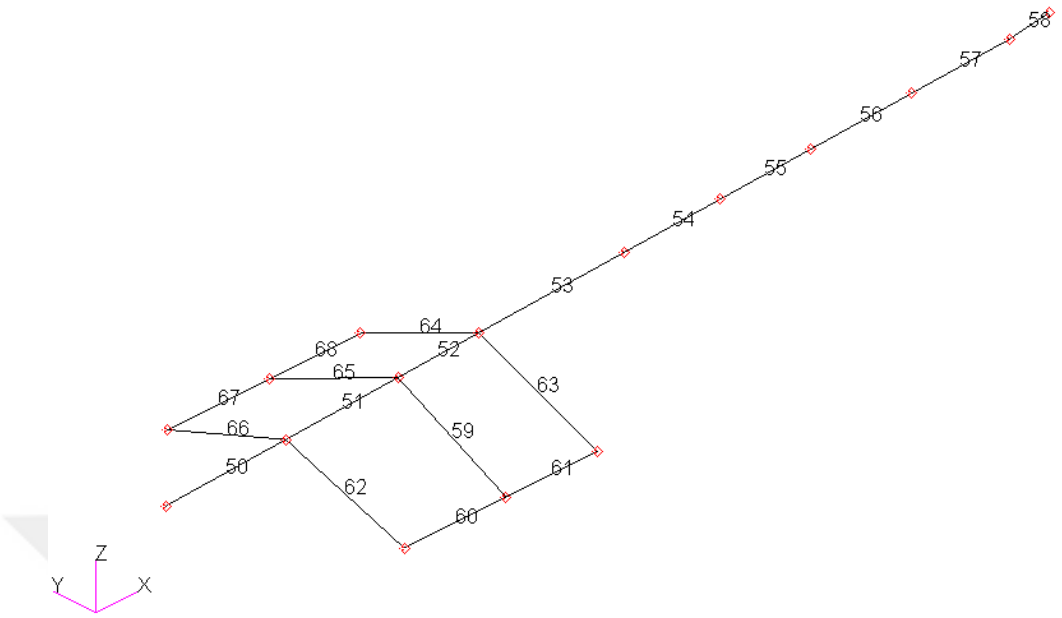

Figure B.4 Element numbering of the fuselage and the fuselage-wing connection

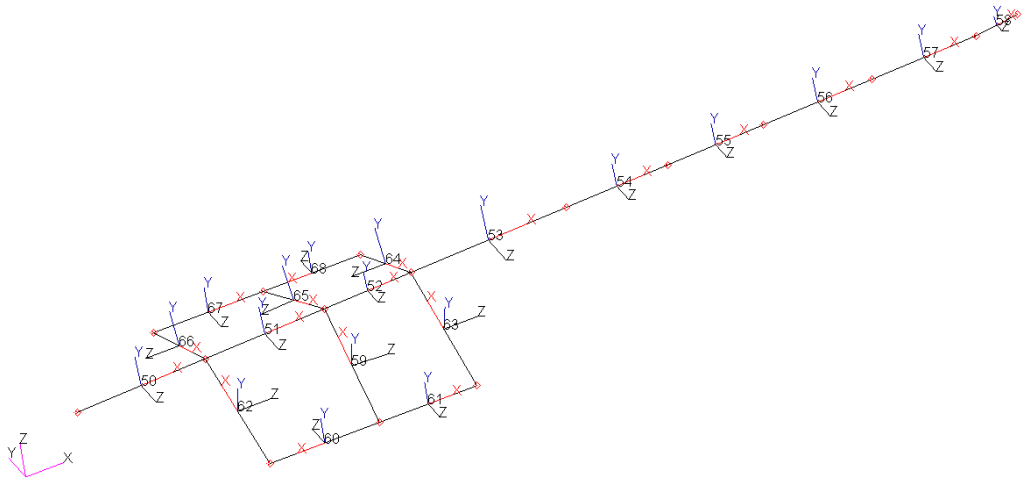

Figure B.5 Element coordinate frame of the fuselage and the fuselage-wing connection beams

Table B.2 Cross sectional properties of the fuselage and the fuselage-wing connection beam elements

Number of the Beam Element	*Cross sectional area [mm²]*	I_{zz} *[mm⁴]*	I_{yy} *[mm⁴]*	*J [mm⁴]*
50	3.62E+01	1.38E+00	8.92E+01	1.95E+01
51	1.55E+00	1.60E+01	5.96E+01	2.04E+01
52	3.42E+01	1.11E+01	4.79E+00	3.04E+01
53	7.81E-01	7.37E+00	8.91E+01	2.76E+01
54	5.45E-01	3.70E+01	8.54E+01	8.86E+01
55	2.74E+01	7.60E+01	8.69E+01	2.64E+01
56	5.55E+00	3.61E+01	6.29E+01	3.32E+01
57	2.42E+01	1.94E+00	6.57E+01	1.89E+01
58	4.00E+01	3.70E+01	6.56E+00	4.65E+01
59	5.10E+01	3.67E+01	2.02E+02	4.90E+02
60	9.27E+01	6.82E+02	1.19E+03	1.78E+02
61	1.32E+02	5.22E+02	2.23E+02	8.57E+02
62	2.35E+02	5.88E+03	2.24E+02	8.81E+02
63	2.88E+02	1.70E+03	3.79E+02	3.19E+02
64	5.10E+01	3.67E+01	2.02E+02	4.90E+02
65	9.27E+01	6.82E+02	1.19E+03	1.78E+02
66	1.32E+02	5.22E+02	2.23E+02	8.57E+02
67	2.35E+02	5.88E+03	2.24E+02	8.81E+02
68	2.88E+02	1.70E+03	3.79E+02	3.19E+02
Elastic Modulus (Fuselage)	1.16e+13 N/mm²			
Shear Modulus (Fuselage)	1.30e+13 N/mm²			
Elastic Modulus (Connection beams)	1.09e+10 N/mm²			
Shear Modulus (Connection beams)	1.25e+09 N/mm²			

Thirdly, the cross-sectional properties of the vertical tail plane's beams are given in Table B.3. Element numbering and element coordinate frames of the vertical tail plane are shown in Figure B.6, and B.7, respectively.

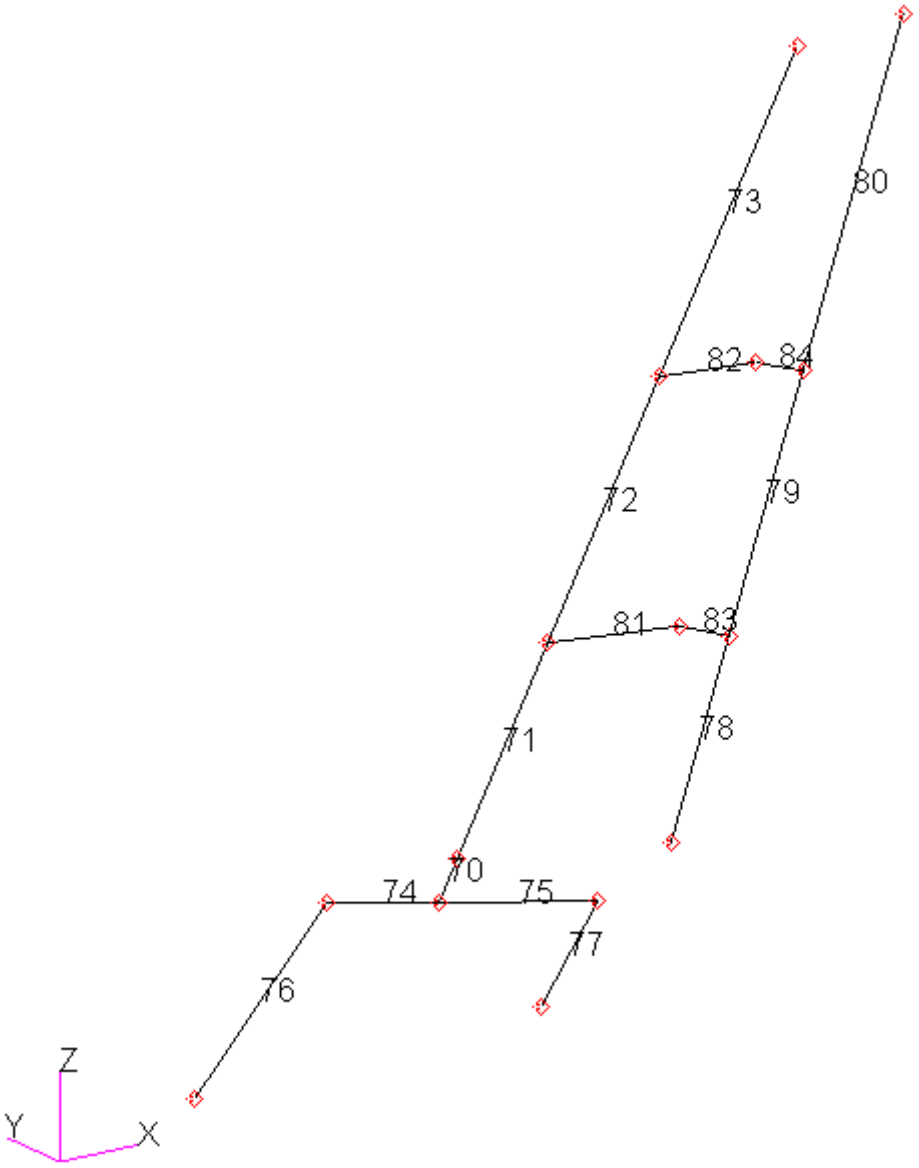

Figure B.6 Element numbering of the vertical tail plane

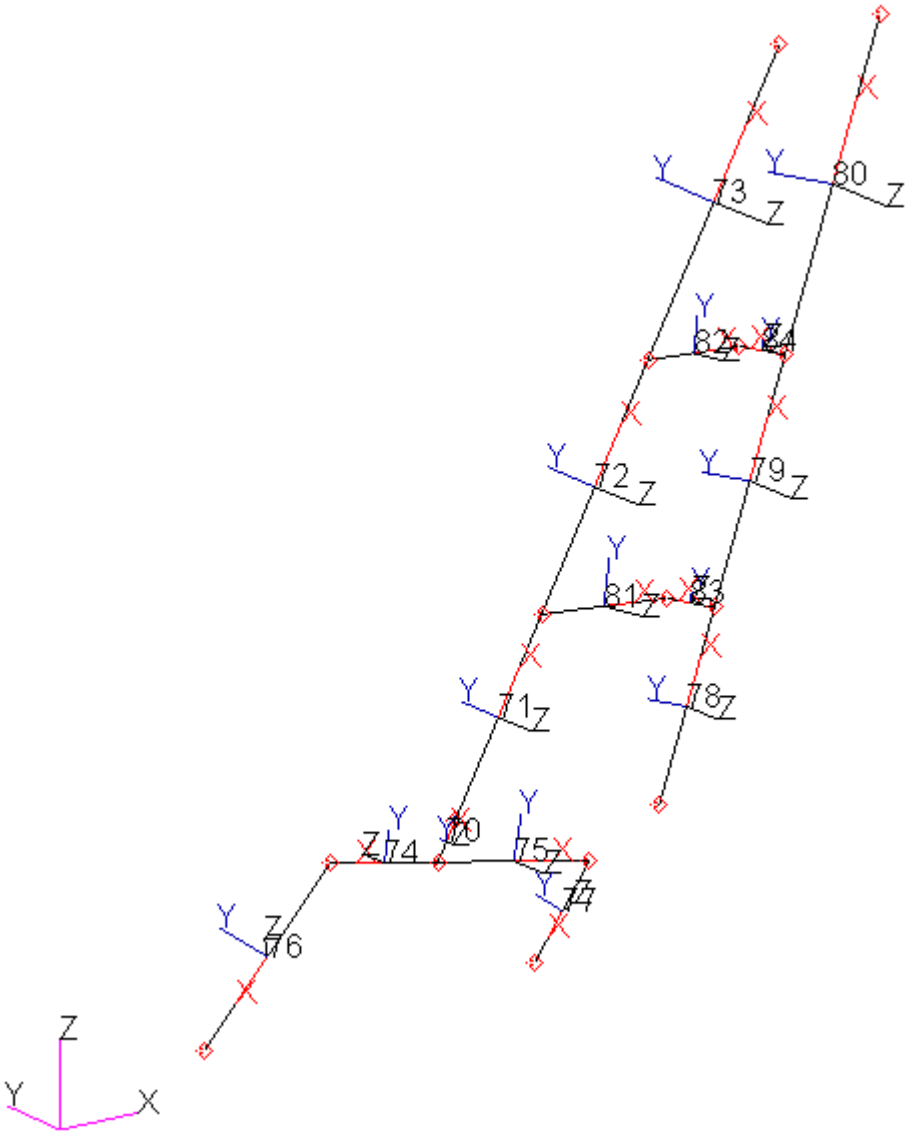

Figure B.7 Element coordinate frame of the vertical tail plane

A zoomed view of the connection beams between the vertical tail and the rudder is given in Figure B.8 for clarity.

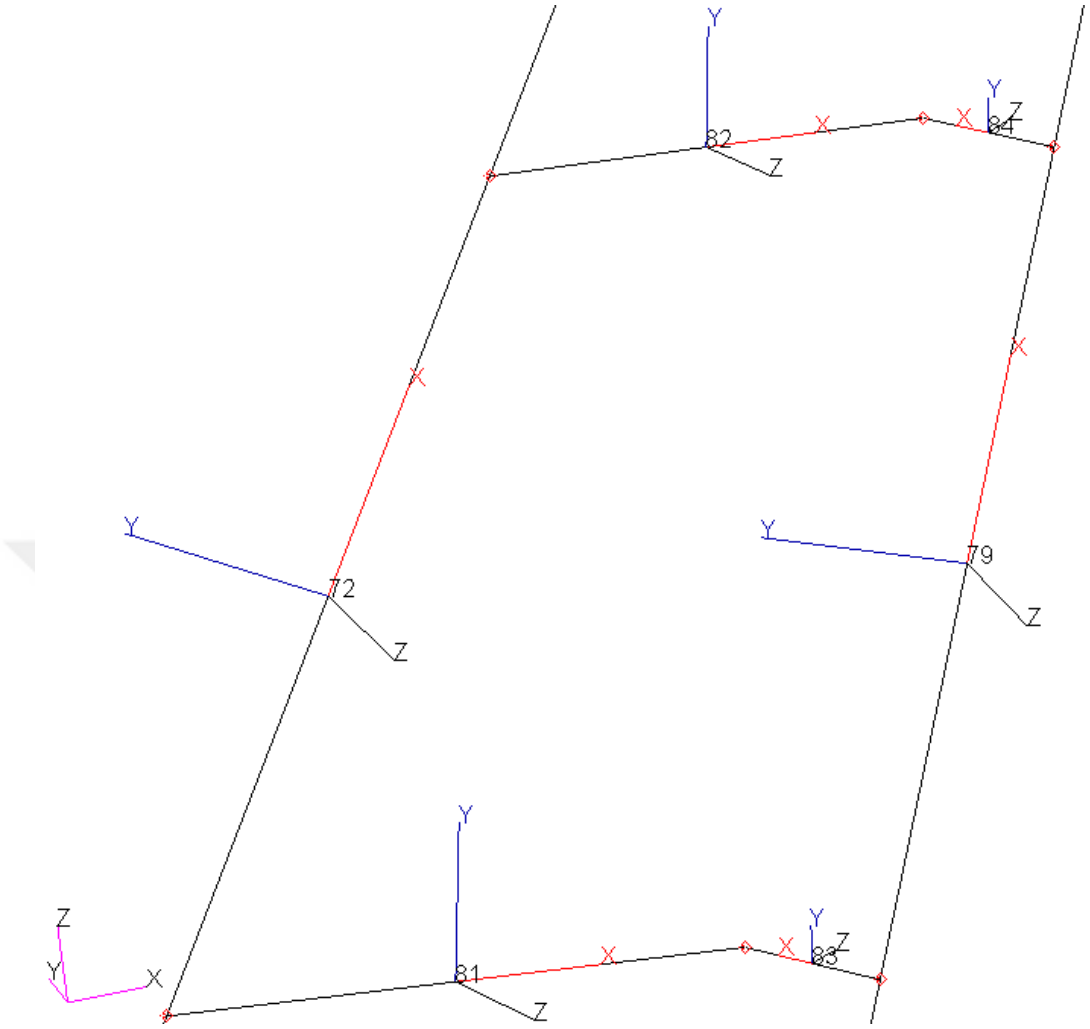

Figure B.8 Zoomed view of the vertical tail-rudder connection beams

Table B.3 Cross-sectional properties of the vertical tail plane

Number of the Beam Element	*Cross sectional area [mm²]*	I_{zz} *[mm⁴]*	I_{yy} *[mm⁴]*	*J [mm⁴]*
70	4.85E+01	1.33E+02	3.20E+04	1.32E+02
71	1.20E+01	7.86E+00	5.24E+04	1.33E+03
72	2.03E+02	1.08E+02	5.72E+03	1.40E+02
73	6.09E+02	1.08E+03	2.04E+04	2.21E+02
74	3.22E+01	4.48E+01	4.21E+04	1.21E+02
75	4.20E+02	1.43E+03	2.87E+04	7.26E+02
76	9.59E+02	1.17E+03	4.19E+04	5.49E+01
77	1.25E+02	2.59E+02	7.93E+04	8.87E+01
78	6.14E+02	1.02E+03	2.55E+04	3.68E+02
79	2.25E-02	1.58E+00	4.89E+04	1.53E+01
80	4.09E+01	1.99E+00	3.26E+04	9.46E+00
81	8.14E+01	4.24E+01	7.55E+04	1.18E+01
82	3.03E+02	5.59E+02	1.84E+04	1.81E+02
83	1.46E+02	4.76E+02	7.79E+04	4.77E+02
84	1.09E+02	5.76E+02	1.01E+05	9.59E+02
Elastic Modulus (Vertical tail-vertical tail-fuselage connection)	8.65e+09 N/mm²			
Shear Modulus (Vertical tail-vertical tail-fuselage connection)	7.22e+08 N/mm²			
Elastic Modulus (Rudder)	9.20e+9 N/mm²			
Shear Modulus (Rudder)	8.40e+9 N/mm²			
Elastic Modulus (Connection beams between vertical tail and rudder)	7.86e+09 N/mm²			
Shear Modulus (Connection beams between vertical tail and rudder)	6.75e+08 N/mm²			

Horizontal tail beam properties are given in Section 5.6. Finally, the elevator and elevator-horizontal tail connection are shown in Table B.4.

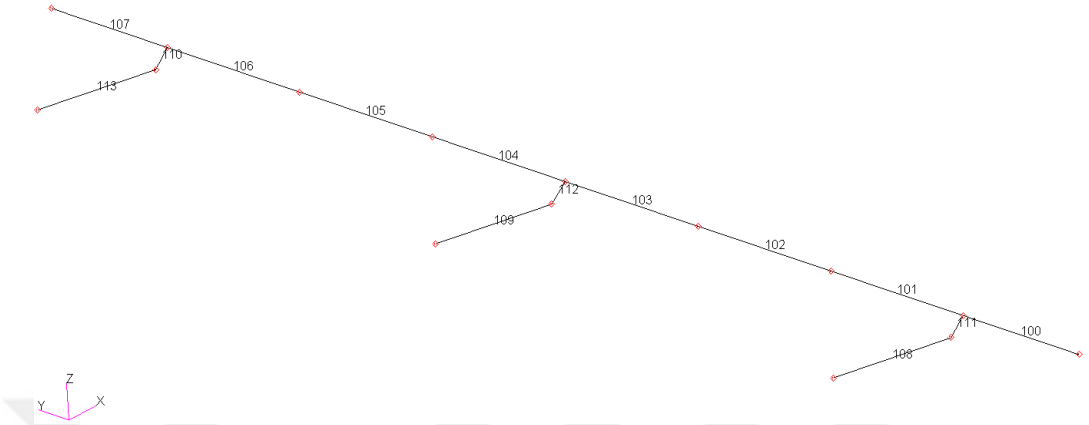

Figure B.9 Element numbering of the elevator and elevator-horizontal tail connection beams

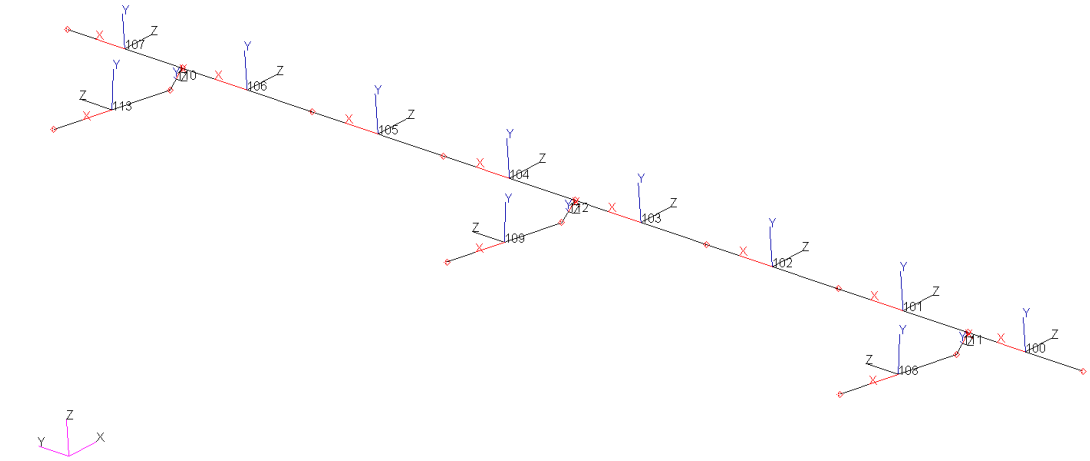

Figure B.10 Element coordinate frames of the elevator and elevator-horizontal tail connection beams

To enhance clarity of element 110, 111, and 112, Figure B.11 displays a zoomed version of element 111. It is important to note that all three elements share the same coordinate frame.

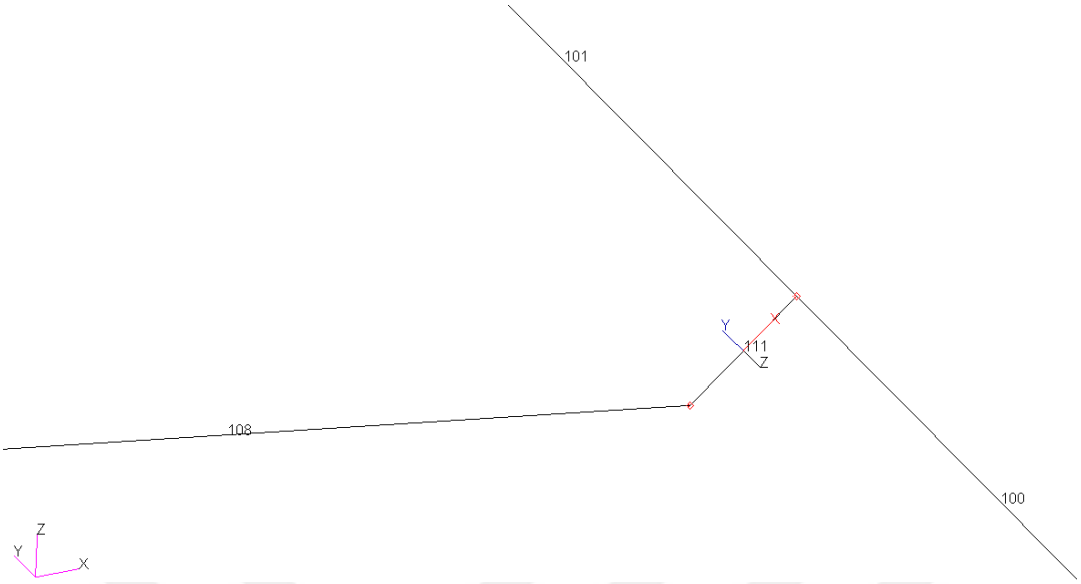

Figure B.11 Zoomed view of the element 111

Table B.4 Cross-sectional properties of the elevator and the horizontal-elevator connection beams

Number of the Beam Element	*Cross sectional area [mm²]*	I_{zz} *[mm⁴]*	I_{yy} *[mm⁴]*	*J [mm⁴]*
100	2.43E+02	7.96E+00	3.99E+03	4.18E+01
101	1.71E+01	2.11E+00	3.24E+03	4.81E+00
102	5.56E+01	2.52E+01	6.23E+01	7.67E+00
103	4.32E+01	1.76E+00	4.32E+03	1.62E+01
104	4.32E+01	1.76E+00	4.32E+03	1.62E+01
105	5.56E+01	2.52E+01	6.23E+01	7.67E+00
106	1.71E+01	2.11E+00	3.24E+03	4.81E+00
107	2.43E+02	7.96E+00	3.99E+03	4.18E+01
108	5.63E+01	6.11E+01	7.23E+02	2.09E+01
109	6.86E+01	4.91E+01	6.56E+03	5.67E+01
110	4.48E+01	3.02E+01	3.59E+03	7.13E+01
111	4.48E+01	3.02E+01	3.59E+03	7.13E+01
112	3.24E+01	7.65E+00	4.42E+03	5.42E+01
113	5.63E+01	6.11E+01	7.23E+02	2.09E+01
Elastic Modulus (Elevator)	3.98+9 N/mm²			
Shear Modulus (Elevator)	1.28e+9 N/mm²			
Elastic Modulus (Connection beams between elevator and horizontal tail)	4.33e+09 N/mm²			
Shear Modulus (Connection beams between elevator and horizontal tail)	1.25+08 N/mm²			

C. Comparison of the Mode Shapes

MODE 4

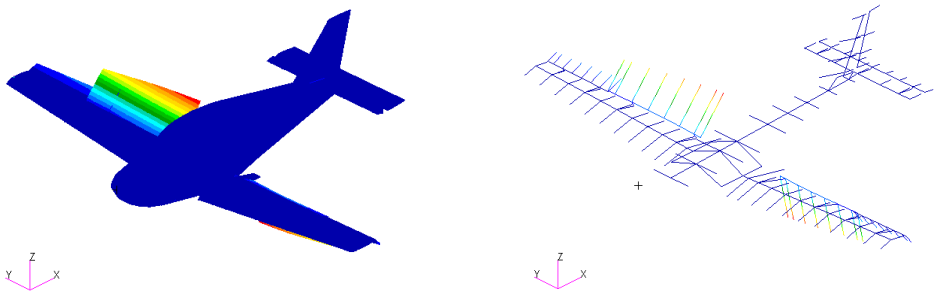

MODE 5

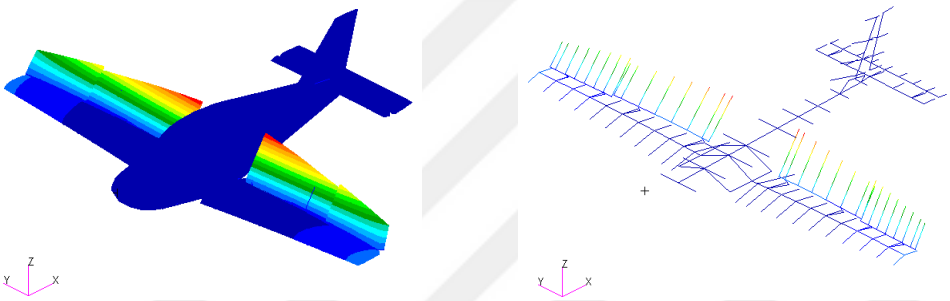

MODE 6

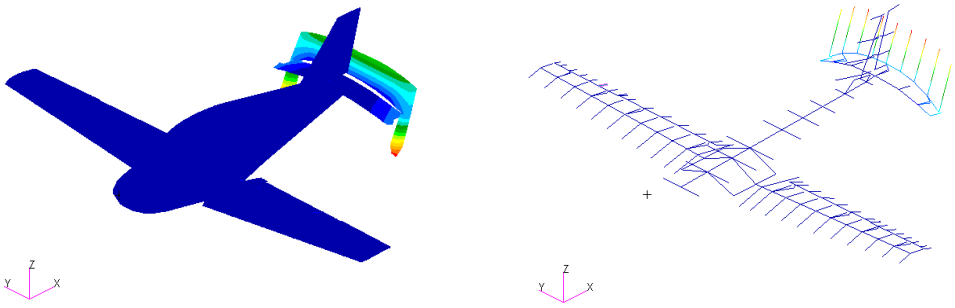

MODE 7

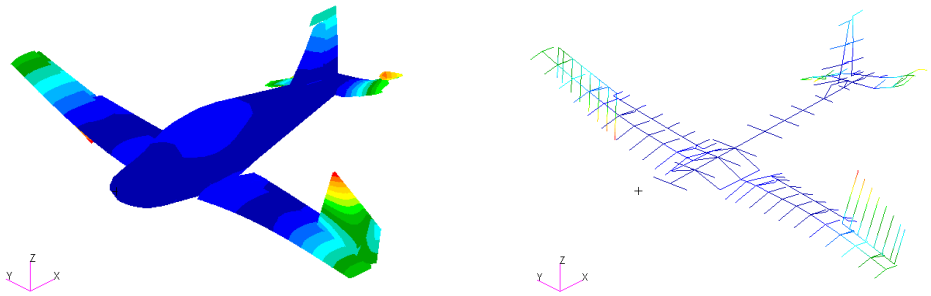

MODE 8

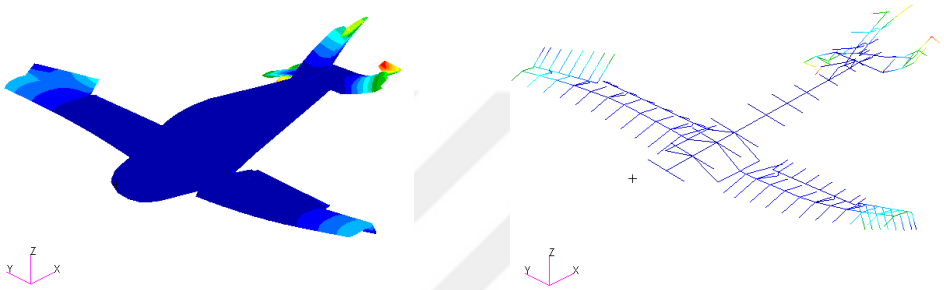

MODE 9

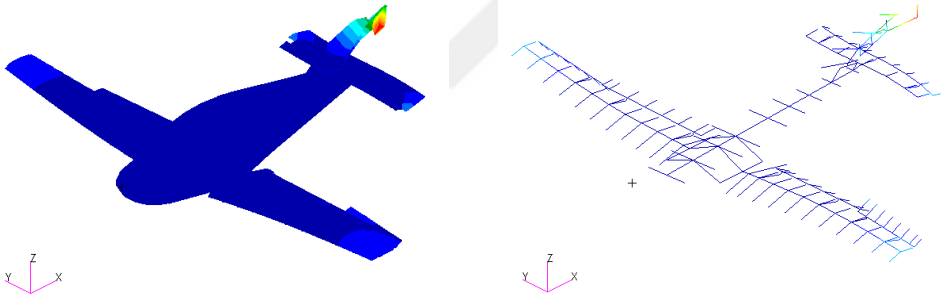

MODE 10

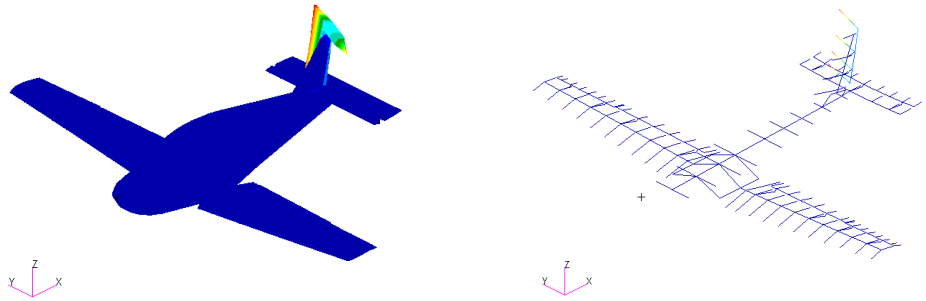

MODE 11

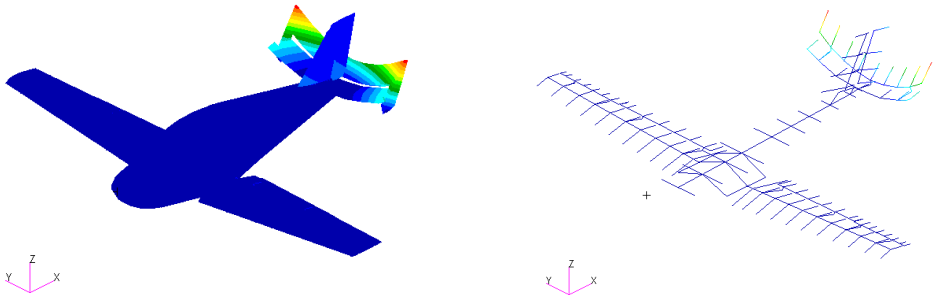

MODE 12

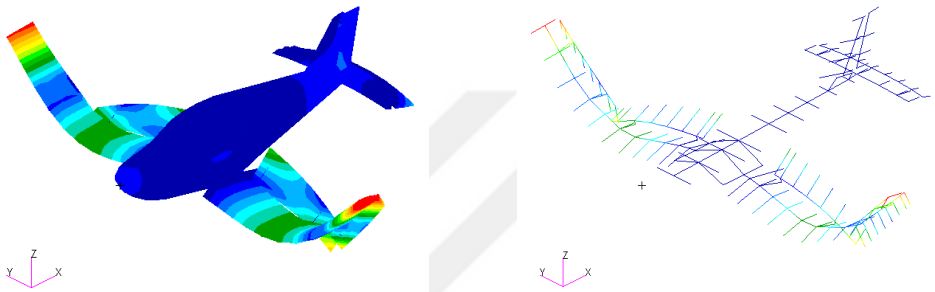

MODE 13

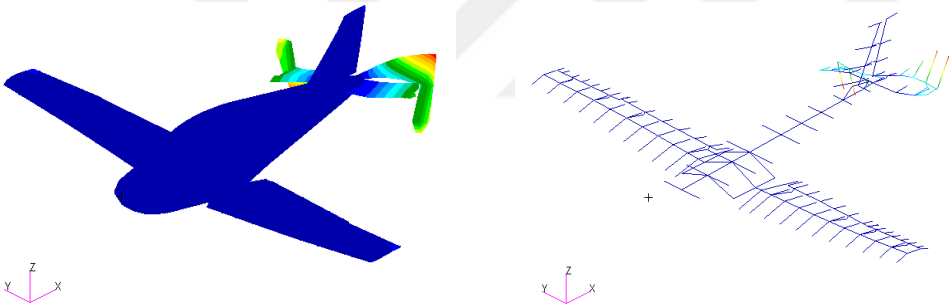

MODE 14

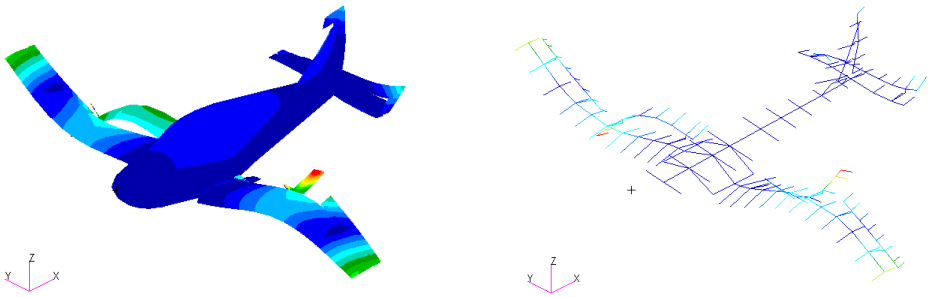

MODE 15

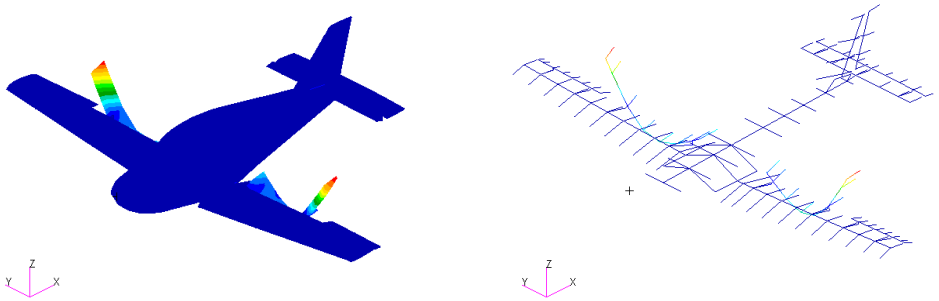

MODE 16

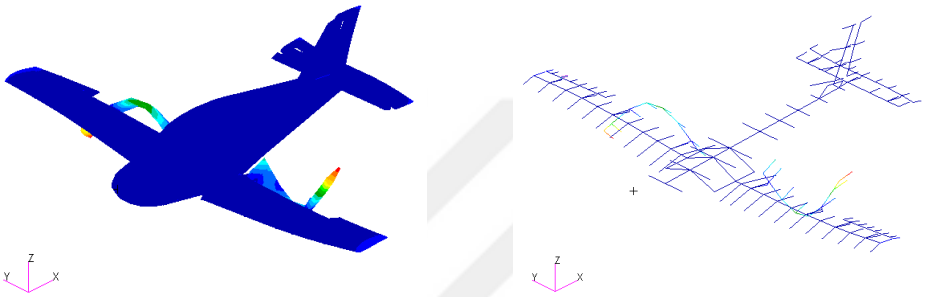

MODE 17

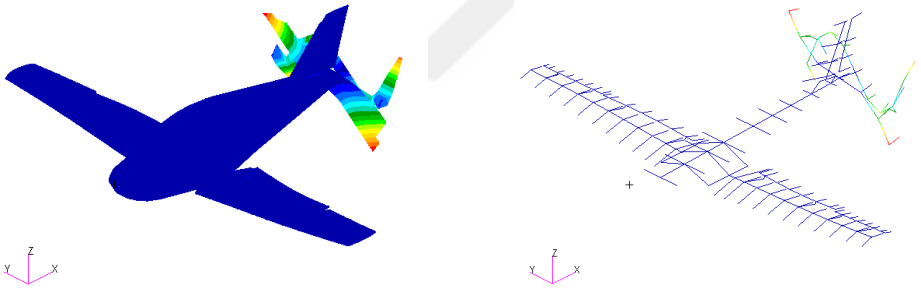

MODE 18

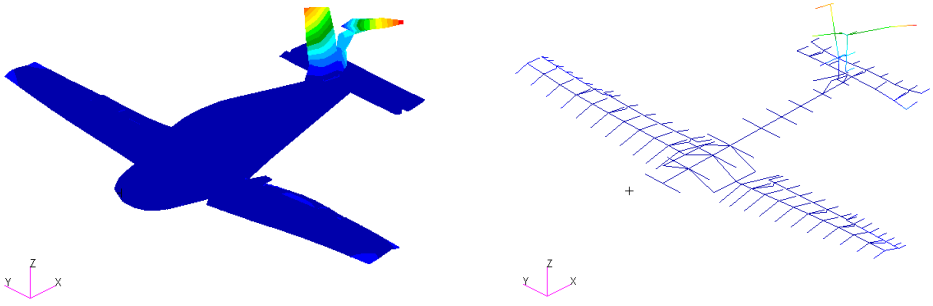

MODE 19

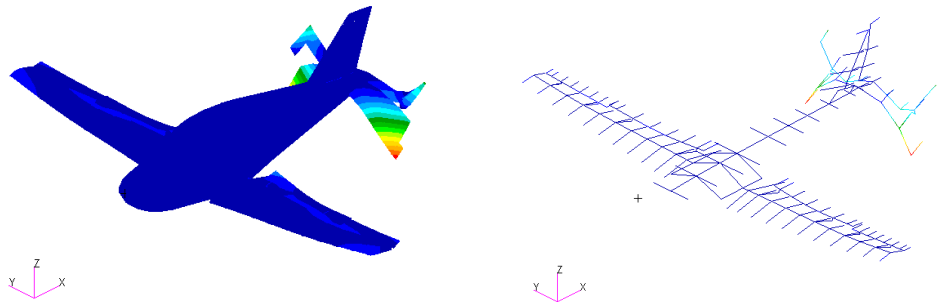

MODE 20

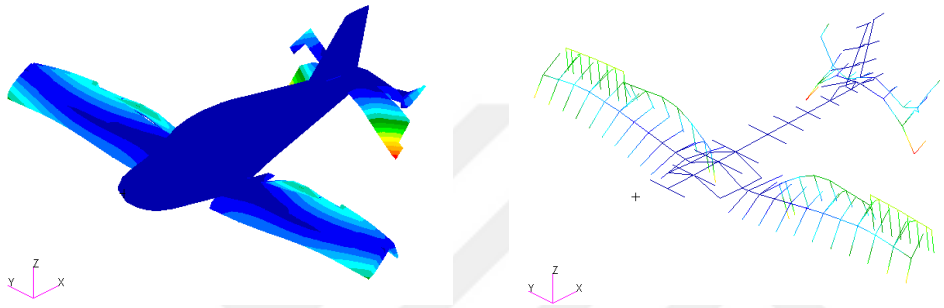

Figure C.1 Comparison of the mode shapes